

Physical Characterization of the Lower Carboniferous Limestone as a potential Geothermal Reservoir

T. Goense



Physical Characterization of the Lower Carboniferous Limestone as a potential Geothermal Reservoir

By

T. Goense

in partial fulfilment of the requirements for the degree of

Master of Science

in Petroleum Engineering and Geosciences

at the Delft University of Technology,
to be defended publicly on Friday August 24, 2018 at 15:00 PM.

Supervisors:	Prof. dr. D.F. Bruhn	TU Delft
	Ir. C. Kluge	TU Delft
Thesis committee:	Dr. A. Barnhoorn	TU Delft
	Dr. G. Blöcher	GFZ Potsdam

This thesis is confidential and cannot be made public until December 31, 2019.

An electronic version of this thesis is available at <http://repository.tudelft.nl/>.

Abstract

To develop high enthalpy geothermal systems in the Netherlands, reservoirs with a depth greater than 4000 m need to be targeted. The Lower Carboniferous limestone is proposed as the main target due to its depth and wide occurrence. To investigate the potential of this formation, the physical rock properties are studied in a variety of laboratory experiments. This study consists of two parts: (1) the geomechanical and hydraulic characterization of the intact rock and (2) the permeability evolution of a fracture altered rock.

Analogous rock samples from a quarry were used to determine tensile, compressive and shear strength and the elastic moduli. Further rock properties such as porosity, microstructure and mineralogy were measured by a gas pycnometer, mercury intrusion porosimetry and electron microscope analyser. The permeability was determined by flow-through experiments at different effective pressures. Subsequently, shear fractures were generated by triaxial deformation and a punch-through shear test to investigate the effect on the permeability.

A high degree of heterogeneity between the samples and a clear transverse anisotropy was observed. The maximum intact rock permeability is 150 μD at low effective pressures (2 MPa) and at reservoir conditions the permeability is below 1 μD . This results in an insufficient matrix conductivity and enhancement of the reservoir is needed to improve the reservoir connectivity. Both shear experiments show an increase in permeability of one to four orders of magnitude. The fractures show to be sustainable in terms of time and pressure variations. In combination with its physical rock properties, it can be concluded that the application of hydraulic stimulation within the Lower Carboniferous limestone is a reliable technique to improve the reservoir permeability.

Acknowledgements

I would like to thank everyone who supported me during the nine months of pursuing my thesis. Foremost, I would like to thank professor David Bruhn, who gave me the opportunity to perform my thesis within the Geothermal Systems department at GFZ Potsdam. His knowledge, patience and great enthusiasm inspired me a lot in the establishment of this work. He kept faith in me until the end in which I am really thankful.

Special thanks to Christian Kluge who supervised me from day to day. I really appreciate his dedication, eagerness and constant availability during the time I have been in Potsdam. I enjoyed working together and spending the time in the laboratory. I also would like to thank dr. Guido Blöcher for his supervision and being a member of my assessment committee. His supervision and critical look really improved the quality of the thesis.

I also want to thank Tanja and Christian for operating and maintaining the MTS and other devices I used within the laboratory of GFZ Potsdam. In addition, I would like to thank Ellen, Wim and Joost for the CT images and Karel for performing the ultrasonic wave experiments. Furthermore I would like to thank dr. Fiorenza Deon for the electron microprobe images and her guidance with the interpretations. Also thanks to dr. Richard Bakker who provided me extra data and came up with helpful suggestions.

Next I would like to mention the SURE project its partners and the Stichting Molengraaff fonds for their support.

Ultimately, I would like to thank all family and friends for their motivational support during my thesis and the encouragement throughout the years.

Delft University of Technology
August 5, 2018

Twan Goense

Table of Contents

Abstract	4
Acknowledgement.....	6
Table of Contents.....	8
1 Introduction	10
1.1. Geothermal Energy Demand	10
1.2. Lower Carboniferous Limestone	11
1.3. Enhanced Geothermal Systems	12
1.4. Shear and Tensile fractures.....	13
1.5. Research Objective.....	13
2 Reservoir Characteristics	16
2.1. Geological Setting	16
2.2. Well Data.....	17
2.3. Karstification	18
2.4. Porosity and Permeability.....	20
2.5. Seismic Data	20
2.6. Sample Location.....	20
3 Methodology	22
3.1. Rock Specimen.....	22
3.2. Rock Parameters	23
3.3. Mechanical Testing System (MTS)	24
3.4. Mechanical Characterization	25
3.4.1. Brazilian Tensile Strength test.....	25
3.4.2. Unconfined Compressive Strength Test	26
3.4.3. Triaxial Compressive Test	27
3.4.4. Acoustic Measurements	29
3.5. Hydraulic characterization	29
3.5.1. Helium Pycnometer	29
3.5.2. Hydrostatic weighing.....	30
3.5.3. Mercury Intrusion Porosimetry	30
3.5.4. Gas Permeameter	31
3.5.5. Hydraulic Response in the Triaxial Cell	33
3.6. Fracture Characterization	34
3.6.1. Punch-Through Shear Test	34
3.6.2. Triaxial Induced Shear Fracture	37
4 Mineralogical Characteristics.....	40
5 Results.....	44
5.1. Tensile strength	44
5.2. Mode I Fracture toughness	46

5.3.	Mode II Fracture toughness	46
5.4.	Unconfined Compression Strength	47
5.5.	Triaxial Compressive strength.....	49
5.6.	Failure Criteria.....	50
5.7.	Elastic Moduli	51
5.8.	Porosity	52
5.8.1.	Porosity Change	53
5.8.2.	Bulk Volume Change	54
5.8.3.	Biot's Coefficient	55
5.8.4.	Pore Size Distribution	56
5.9.	Permeability	57
5.9.1.	Punch-Through Shear Permeability.....	59
5.9.2.	Shear Fracture Permeability	63
6	Discussion	68
6.1.	Representativity of the Investigated Samples	68
6.2.	Mechanical Characterization	68
6.3.	Hydraulic Characterization.....	72
6.4.	Influence of the Bedding on Mechanical and Hydraulic Properties.....	73
6.5.	Reservoir Improvement by Shear Fracturing.....	73
6.6.	Reservoir Implications and the Potential of EGS within the Lower Carboniferous Limestone.....	75
7	Conclusions and Recommendations.....	78
	Bibliography.....	79
	List of figures.....	84
	List of tables	88
	Appendix A	89
	Appendix B	90
	Appendix C	91
	Appendix D.....	92
	Appendix E	93
	Appendix F	94
	Appendix G.....	96
	Appendix H.....	97
	Appendix I.....	98

1

Introduction

1.1. Geothermal Energy Demand

Over the past decades the worldwide energy consumption has grown tremendously. Compared to 2015, the U.S. Energy Information Association (EIA) predicts an increase of the world energy demand of 28 percent by 2040. The conventional energy sources such as coal, oil and natural gas will remain to play a significant role in the fulfilment of the energy demand. However, following the objectives on reducing greenhouse gas emissions as set out by the Paris Agreement, renewable energy sources will have to cover a major part of future demand. Currently, renewables are the world's fastest-growing energy source and the EIA predicts an average increase of 2.3 percent per year until 2040 (Figure 1.1; EIA, 2017).

World energy consumption by energy source
quadrillion Btu

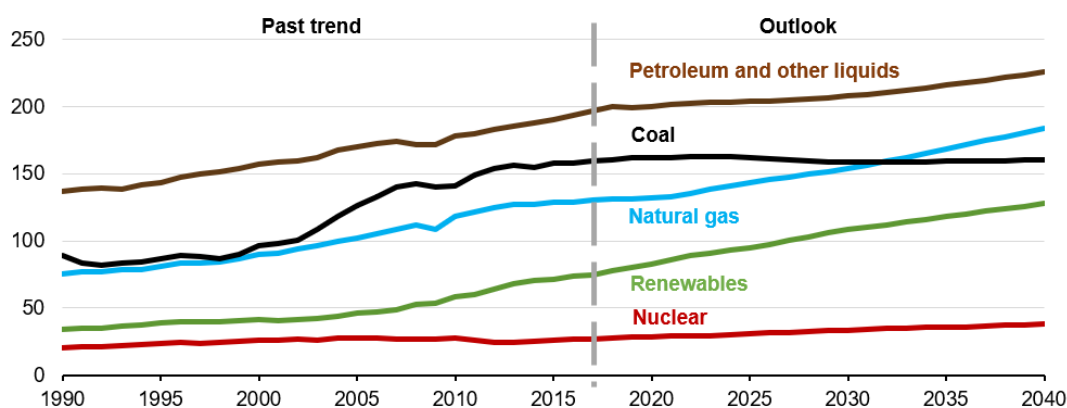


Figure 1.1: World Energy consumption (EIA, 2017)

Geothermal energy is considered as one of these renewable energy sources. Since it provides continuous heat and has low carbon emission, it has a growing share of the energy mix for many areas (Adams, 2015). Geothermal power has a capacity factor of over 90 percent which is significantly higher than solar and wind with 14 and 25 percent, respectively (Li, 2013). However, geothermal energy is still in a probing stage compared to solar and wind despite its considerable potential (Figure 1.2; Li, 2013). This is a result of high initial investment costs, long payback time and large geological uncertainties (Willems, 2017). In order to achieve further development of geothermal energy, these constraints must be overcome.

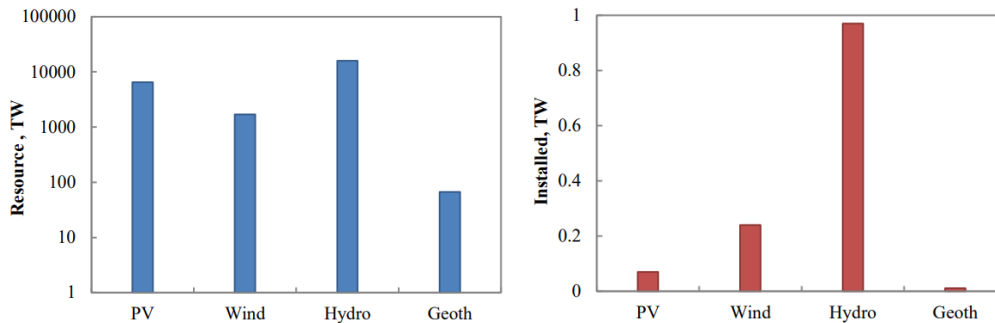


Figure 1.2: Left: Potential resources in TW (Jacobson, 2009), Right: Installed power in TW (Li, 2013)

Over the last decade, 16 geothermal projects have been installed in the Netherlands for heat production applications. With well depths between 1500 m and 3000 m and temperatures between 60 °C to 100 °C, these projects are low-enthalpy geothermal systems and are only used for heat production. It is mainly used in the horticultural sector, but the heat can also be applied to district heating networks. Within the Dutch industrial sector, higher temperatures are required. Around 31 percent of the industrial heat demand requires temperatures between 100 °C and 200 °C, which can almost completely be supplied by geothermal energy (Energierapport, 2016). According to an average thermal gradient of ~30 °C/km, geothermal systems with wells of more than 4000 m need to be realised to meet these temperatures. This is considered “ultra-deep” geothermal. In 2017, the Dutch Ministries of Economics, Infrastructure and the Environment, EBN, TNO and six consortia of companies have signed the “Green Deal Ultra-Diepe Geothermie (UDG)”. In this agreement the parties aim to increase the knowledge of ultra-deep geothermal energy and to reduce the risks of (ultra-)deep geothermal projects (Rijksoverheid, 2017). Fulfilment of this UDG agreement will be achieved by an exploration and resource assessment campaign and the potential realisation of ultra-deep geothermal doublets with the Lower Carboniferous limestone group as the main target.

1.2. Lower Carboniferous Limestone

The matrix porosity and permeability of the intact Lower Carboniferous limestone are low. In general, the porosity is around 1-2% and the permeability is in the order of a few mD. Nevertheless, Kramers et al. (2011) suggested this formation as a potential geothermal reservoir due to the dolomitization, karstification and the fracture frequency observed in geothermal reservoirs in Belgium. This results in sufficient secondary porosity and permeability. In addition, Boxem et al. (2016) described the Carboniferous limestone group specifically as a potential play for the ultra-deep geothermal energy within the Netherlands.

In the Dutch subsurface, the Lower Carboniferous limestone, also known as Dinantian carbonates or Kolenkalk, is widely present. The top of the formation is generally below 4000 m (Figure 1.3, TNO), for example in Luttelgeest (Mid-North Netherlands) the top is at 4355 m (well LTG-01, NLOG). In the south of the Netherlands, the Dinantian is located less deep and in Belgium and Germany the formation is even present at surface outcrops. The exploration of hydrocarbons in the Netherlands throughout the years has led to an extensive knowledge about the Dutch subsurface. The target of these efforts, however, has been limited to the upper 2 – 3 kilometres of the onshore subsurface. Therefore less than 20 wells have penetrated the Dinantian and high quality seismic data are only locally available in the Netherlands (van Hulten; 2012). As a consequence, the interpreted depth and thickness of the Dinantian formation is uncertain.

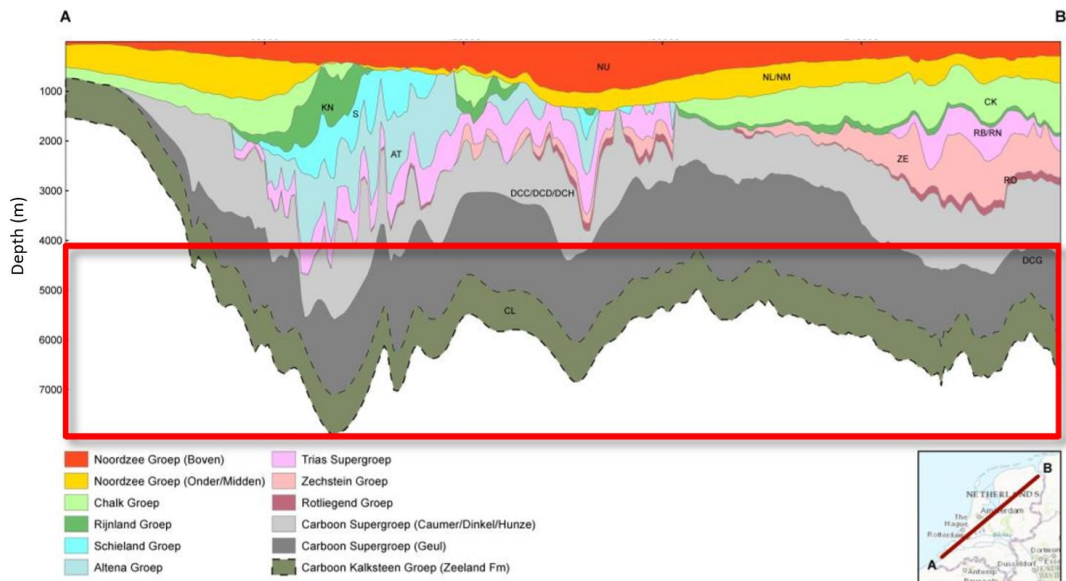


Figure 1.3: SW-NE cross section of the Dutch subsurface. The Lower Carboniferous limestone is indicated by Carboon Kalksteen Groep (CL). Since the thickness of the Lower Carboniferous is uncertain, the formation is indicated by a dashed line (TNO).

Two geothermal doublets located in Limburg have already targeted the Dinantian formation at around 2 km depth. Due to the presence of natural fractures and karst in these projects, productivity of the Lower Carboniferous limestone is sufficient. The wide occurrence at the depth of interest and the proven reservoir makes the formation a promising reservoir for the application of ultra-deep geothermal. However, the presence and the degree of natural fractures, dolomitization and karstification in the deeper located Dinantian limestones is unknown. Therefore, it is questionable if this potential target meets the criteria for an efficient heat production from a deep geothermal system. In case of inadequate production rates, the application of suitable reservoir enhancement techniques needs to be taken into account to improve the productivity.

1.3. Enhanced Geothermal Systems

Hydraulic stimulation, acidizing, thermal stimulation and radial jetting are techniques to enhance the connectivity of a geothermal reservoir. Enhanced Geothermal Systems (EGS) were first proven in poorly producing crystalline rocks by hydraulic stimulation (Soultz-sous-Forêts). The use of acid to enhance the permeability is based on dissolving or disperse materials in the near wellbore region (Economides and Nolte, 2000). Within thermal stimulation, cold water is injected into the reservoir to induce thermal stress resulting in fractures. In hydraulic stimulation, a fluid is injected into the reservoir under a high pressure to generate and displace fractures. A more recently developed method is Radial Jet Drilling (RJD). It uses high-pressure fluid to drill lateral holes from the main well bore, which enhances the connectivity to the reservoir. The main advantages of this method are the low water consumption, controllability of the connection and a small surface footprint. However, this technique is not fully understood yet and one of the disadvantages are the production of sand and the requirement of a minimum initial porosity of 3-4% (Abdel-Ghany et al, 2011). In order to further develop the RJD method and to investigate the effect in comparison with conventional stimulation techniques, an experimental and theoretic analysis must be performed. To quantify the stimulation performance of RJD, mechanical and hydraulic parameters of the proposed rock need to be derived from laboratory experiments. These parameters can be used to derive the quantitative dependency of the RDJ method on various physical properties of the rock. Understanding this dependency, a deliberate decision can be made for the optimal stimulation technique. Therefore the characterization of the mechanical parameters of a potential reservoir, such as the Lower Carboniferous is of high interest.

1.4. Shear and Tensile fractures

Fractures are surfaces or narrow zones of structural discontinuity. Due to either tension or shear, different types of fracture modes will form based on their relative motion across the fracture surface. The different types of fractures are divided into Mode I, Mode II and Mode III fractures (Figure 1.4). Fractures caused by extension are Mode I fractures: the motion is perpendicular to the fracture planes. Mode II and Mode III fractures are caused by shearing: sliding is both parallel to the fracture plane, but perpendicular to the edge in Mode II and parallel to the edge in Mode III.

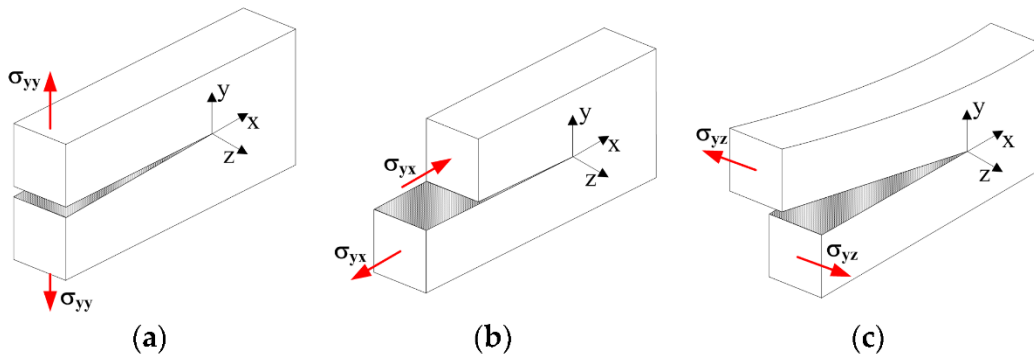


Figure 1.4: Different fracture modes. Left: extensional fracture (Mode I). Center: shearing fracture, perpendicular to edge (Mode II). Right: shearing fracture, parallel to the edge (Mode III) (Golewski, 2017).

In geothermal reservoirs, fractures cause connectivity between the pores and therefore improve the reservoir permeability. These fractures can be either natural or hydraulically induced fractures. Several sources and mechanisms such as changes in lithostatic pressure, fluid pressure, temperature, tectonic forces and other geological processes (folding, salt intrusion and volcanic activity) initiate and propagate fractures. Whether a tensile, shear or a combination of both fractures forms is mainly controlled by the in-situ stress, rock failure criteria and pore pressure (Phillips, 1972). A pure mode of fracturing will only be achieved in a fully homogenous stress field and homogenous rock. In practice, this is not the case and as a result the propagation of a fracture is a mixed mode of fracturing (Backers et al. 2005).

Nevertheless, it is important to investigate the tensile and shear fractures individually. The hydraulic and mechanical behaviour of one single fracture under certain reservoir conditions is the basis of a fractured reservoir model. The obtained parameters such as fracture permeability and aperture under different stress states can be used for upscaled and more complex models and will add to a better understanding of fractures within the Lower Carboniferous limestone.

1.5. Research Objective

This thesis focusses on the characterization of Carboniferous limestone physical rock properties, aiming to understand and improve the permeability by induced fractures. The study consists of two parts: the geomechanical and hydraulic characterization of the intact rock and the permeability evolution of a fracture altered rock. The physical parameters are obtained by laboratory experiments on analogous Carboniferous Limestone rock samples from the Aachen area.

The stresses acting on a reservoir are a combination of the natural stresses (overburden, hydrostatic pressure and tectonic stress) and artificially induced stresses (Schön, 2015). Based on the effective stress law, the effective stress in a reservoir is described as the total stress minus the pore pressure (Terzaghi, 1936). A change in the stress field could lead to deformation or failure of the reservoir rock. The deformation and failure behaviour of an intact rock are controlled by elastic and strength properties, respectively. In this study, the quantification of the elastic properties is performed both by a static method (compressive

deformation) and dynamic method (ultrasonic wave propagation). The rock strength properties (tensile, compressive and shear strength) are obtained from the indirect Brazilian disc test, uniaxial compression test and triaxial compression test to determine rock specific failure criteria (Colmenares and Zoback, 2002).

The rock mechanical behaviour is dependent on a combination of mineralogy, porosity, pore/grain geometry, bedding and microcracks (Basu et al., 2013, Dunn et al, 1973, Akesson et al., 2004). By investigating these physical (microscale) properties in terms of mean and variance, they can be linked to both the rock mechanical and hydraulic properties. Porosity is studied by a gas pycnometer and the pore geometry by Mercury Intrusion Porosimetry. In terms of hydraulic characterization, the permeability of the intact rock is determined by flow-through experiments (liquid and gas) using the steady state and pressure pulse methods.

For the suitability of the Carboniferous limestone as potential EGS target, the rock mass can be approached as consisting of two entities: the intact rock and the discontinuities. These pre-existing discontinuities consist of natural fractures, faults and bedding interfaces. The region around tip of these discontinuities has the highest stress concentration and fracture propagation will therefore initiate at this location. The fracture toughness is the critical stress intensity to initiate crack propagation (Backers et al., 2002). Since the extent of natural fractures is unknown, both the fracture toughness of extensional (Mode I) and in-plane shear (Mode II) fractures by performing Brazilian disc tests and punch-through shear tests are investigated. If besides the fracture toughness, the stress field and rock geometry are known, initiation and propagation of the fractures can be estimated (Backers et al., 2002). As a result, these properties contribute to an estimation of the stimulation effect in natural fractured reservoirs.

The minimum transmissivity of a commercial geothermal well is generally in the range of 1 to 100 Dm (IFC, 2013). In case the overall reservoir permeability is not sufficient, stimulation of the reservoir is needed to improve the connectivity and productivity. Hydraulic fracturing is intended to improve the flow by creating fractures in the near well-bore formation. McClure and Horne (2013) demonstrated that in most cases a mix of both fracture modes will be present. Evans (2015) stated permeability enhancement is mainly found within shear fractures. Therefore, shear induced fractures are investigated to determine the fracture permeability and to understand the effect of enhancing the reservoir by hydraulic stimulation. Due to the pressure distribution and fluctuations within the reservoir, permeability changes are evaluated at different effective pressures. In addition, the effect of shear displacement on the permeability is studied by either the punch-through shear test or a triaxial induced shear fracture. Since both methods create shear fractures, based on a different experimental approach, a comparison in shear fracture behaviour is performed in terms of permeability and fracture geometry.

The outcome of this study contributes to the understanding of the Lower Carboniferous limestone and the development of (ultra-)deep geothermal energy in the Netherlands. The mechanical and hydraulic characterization enlarge the knowledge of the investigated rock and are a fundamental requirement for the decision of optimal stimulation technique. In addition, the fracture characterization provides the basis for the quantification of the effect of induced shear fractures on the reservoir permeability.

2

Reservoir Characteristics

2.1. Geological Setting

During the formation of the Northwest European Carboniferous Basin (NWECEB), an extensional west-to-east sedimentary basin from Ireland to the west of Poland was formed (Kombrink, 2008). In the area above the London Brabant Massif (LMB), horst and graben structures with thick carbonate platforms were formed during the Dinantian period by a rifting event. This rifting was a consequence of subduction of the Palaeo-Tethys in Brittany and Central France (Leeder, 1992). During this period mainly two facies were deposited, the carbonate "Kolenkalk" facies and the clastic Culm facies (McCann, 2008). The carbonate facies are shallow marine limestone and contain predominantly algal reefs, calcareous debris and dark bituminous limestones (McCann, 2008). The transition to the deeper Culm facies is characterized by debris and calciturbidites and is hard to identify (McCann, 2008).

The horst and graben structures initiated during the Dinantian led to the occurrence of isolated carbonate build-ups on the intra-basinal highs (Reijmer et al, 2017). This resulted in a carbonate sequence varying between 500 m and 1000 m in thickness (Fraser and Gawthorpe, 1990). Kombrink (2010) interpreted the Dinantian structural and stratigraphic setting of the Northern Dutch platform based on fault block setting (Figure 2.1). The Dinantian deposits in the Netherlands are named Zeeland formation, consisting of three consecutive members: Beveland, Schouwen and Goeree member (Appendix E). The Dinantian carbonate platforms of the NWECEB are mainly found on structural highs in northern England, Friesland and Groningen, but also exist in fault-bounded graben areas, such as the Lauwerszee Trough (Kombrink, 2008; Kombrink et al, 2010).

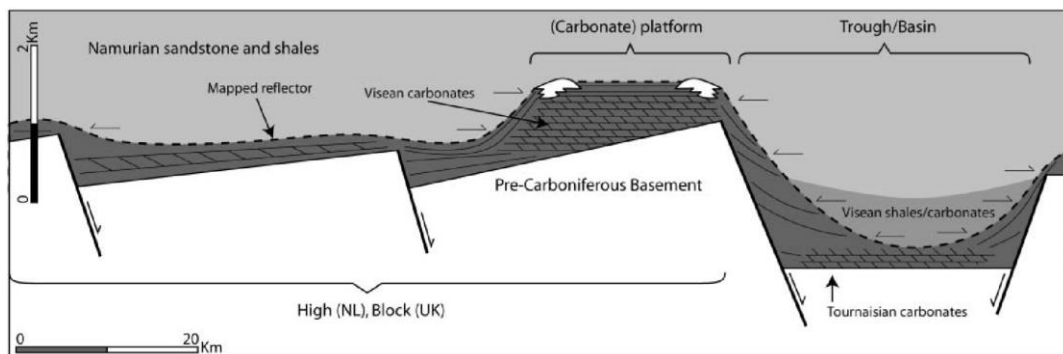


Figure 2.1: Schematic cross-section showing the interpreted structural and stratigraphic setting of the horst and graben structure (Kombrink, 2010).

In the southern onshore part of the Netherlands the Lower Carboniferous consists in general of black limestone and in the northern offshore area clastic sediments are found (Duin et al, 2006). The Campine Basin consists of shallow-marine limestone (Kolenkalk) with a varying thickness as a result of half-graben structures and local block faulting (Kombrink, 2008; Figure 2.3). According to the stratigraphic sequence, the Carboniferous is overlain by the Permian sediment groups Lower and Upper Rotliegend and Zechstein (Figure 2.2). Only on structural highs unconformities are present at the top of the Carboniferous (Figure 1.3,

TNO). In the southwest of the Netherlands and in the northern offshore (Elbow Spit High) the Lower Carboniferous is not present at all.

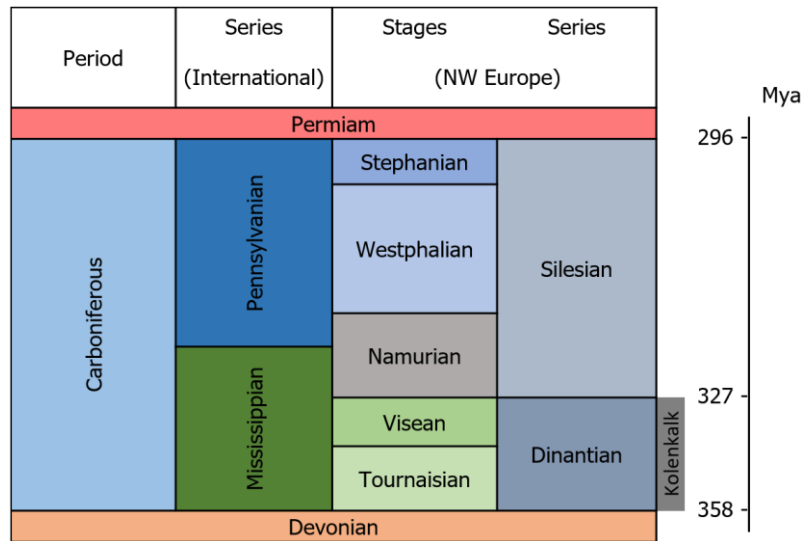


Figure 2.2: Stratigraphy of the Carboniferous period

Finally, in the late Carboniferous, NW-SE inversion took place in the NWEBC causing severe uplift of NW-SE trending basins, but this had minor effect on the NW-SE basins structure itself (Ziegler, 1990). Currently the stress regime in the Netherlands is extensional at all depths where the largest horizontal stress direction is NW-SE.

2.2. Well Data

In the Netherlands and the northern part of Belgium, Dinantian formations are targeted at different locations (Figure 2.3). In particular in Limburg, the northern part of Belgium and in the near offshore of Zeeland the number of wells is higher compared to the rest of the Netherlands. These wells are all located in the Campine basin which has been a proven reservoir by the geothermal doublets in the vicinity of Loenhout (BE), Turnhout (BE) and Californie. In the northern, central and eastern part of the Netherlands, the wells Uithuizermeeden-02 (UHM-2), Luttelgeest-01 (LTG-1) and Winterswijk-01 (WSK-01) target the Dinantian succession. The UHM-2 and LTG-1 both penetrated a platform feature, while the WSK-01 targeted presumably the more clay comprising Kulm facies (nlog, 1978). The data from these wells are used to establish the presence of karst (see Chapter 2.3), the porosity and permeability (see Chapter 2.4).

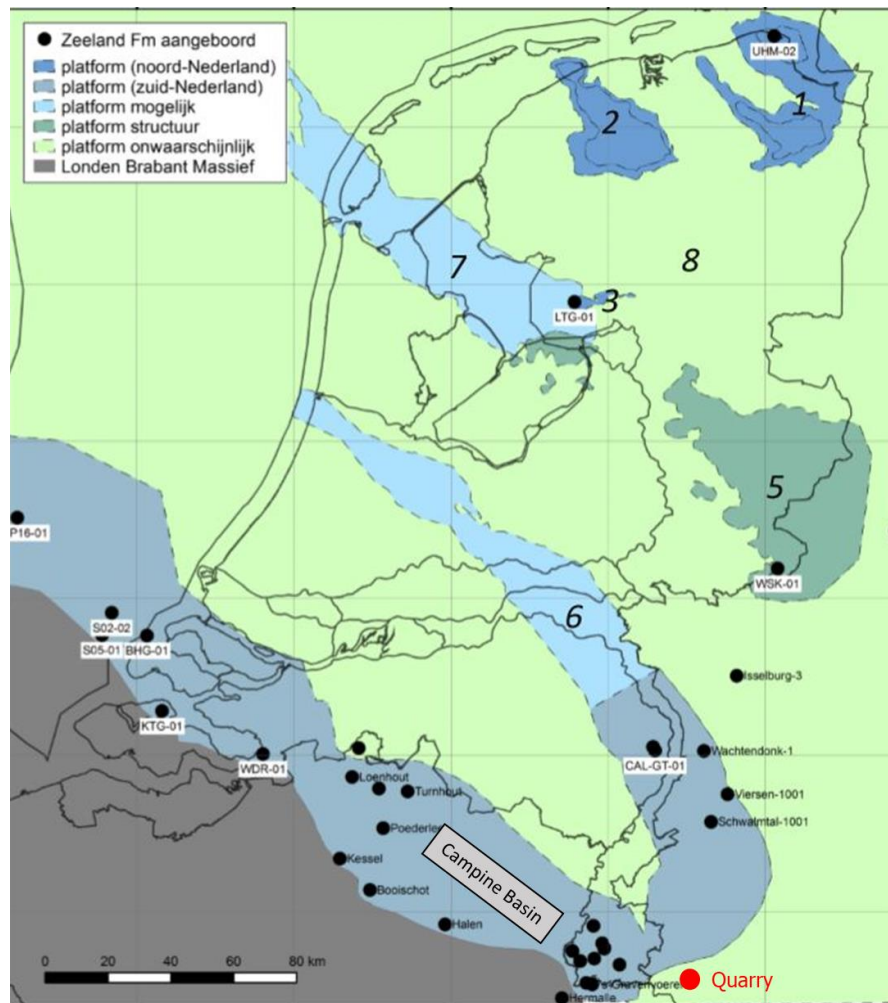


Figure 2.3: Overviews of the wells and carbonate platforms of the Dinantian. Boots (2015), Hoornveld (2013) and Kombrink (2013).

2.3. Karstification

Karstification is the process of carbonate dissolution and can result in a significant increase of pore and fracture connectivity of the reservoir. A combination of relative sea level drop at the right conditions (temperature, salinity and pH) can initiate the karst process (Figure 2.4). As a result of the sea level drop during and after the Dinantian, the exposure of the limestone has led to partial karstification of the platforms. Boxem (2016) attributed the karstification to a hiatus between the Dinantian and the Cretaceous. If no deposits are directly overlying the Dinantian, karst has originated at the surface.

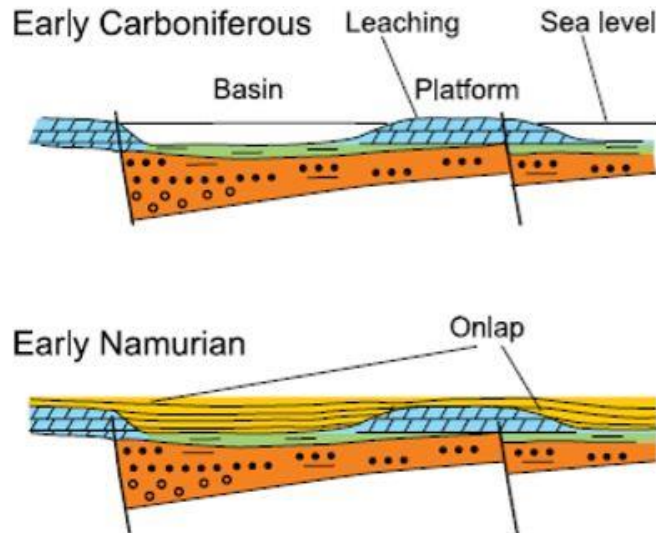


Figure 2.4: Schematic overview of the depositional environment during the Carboniferous indicating the karstification process during and after the deposit of the Dinantian (Geluk et al. 2007).

Within the different locations of the carbonate platform, the reservoir potential changes. Figure 2.5 shows the Derbyshire carbonate platform, a UK Carboniferous hydrocarbon play which could be an analogue for the carbonate platforms in the Netherlands. Intraplatform karst at the top of the platform and the forming of karst at the platform slope are pointed out as the possible karstified locations. Besides the meteoric karstification during the Late Dinantian, hydrothermal karstification took place and altered the formation. The hydrothermal karstification improved the reservoir properties locally, however in other areas this fluid circulation occluded the porosity within mainly fault zones and slope deposits (Reijmer et al., 2017; Hoornveld, 2013).

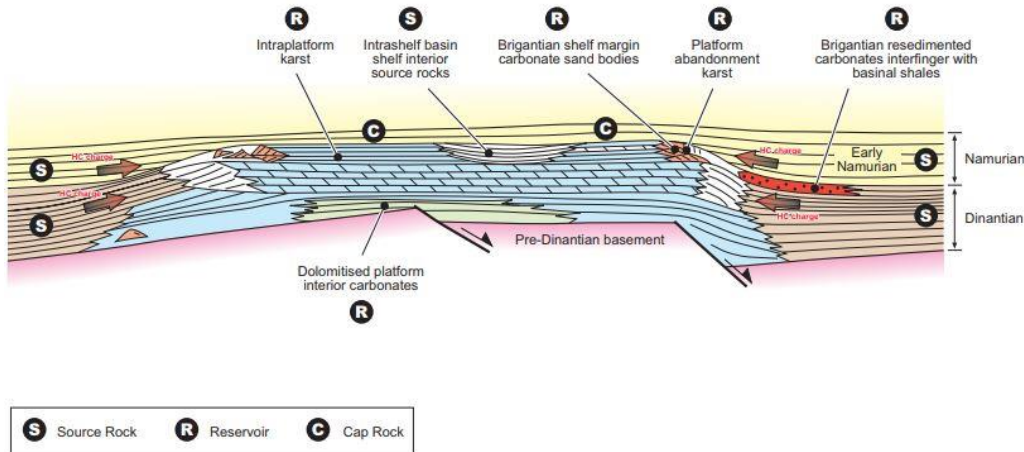


Figure 2.5: Carbonate play showing potential reservoir quality of the Dinantian carbonates (Total, 2007).

Karstification has been identified at different locations within the Campine basin. A well in Turnhout (BE) showed permeabilities up to 1.5 D at depths below 2000 m (Bos and Laenen, 2017). In the CAL-GT-01 well, karst features were encountered resulting in significant fluid losses. Also wells in the northern part of the Netherlands (e.g. LTG-01 and UHM-2) which have penetrated the Dinantian formation showed fluid losses as an indication for karst (Reijmer et al., 2107). However, there is no clear evidence for karst in these deeper located wells.

Besides the improvement of the reservoir permeability, karstification can lead to stress concentrations due to the discontinuity of the rock. Therefore fracture initiation as the stress field changes is presumably near the karstified areas. Karstification starts at fractures, where

water can percolate and dissolve minerals from the rock walls. The newly formed fractures can thereafter be affected by new karstification processes.

2.4. Porosity and Permeability

Based on the analysis of cores, well logs and production data the reservoir properties of Dinantian reservoirs are established (Table 1). The primary porosity and permeability of the Carboniferous limestone is low and assumed insufficient for significant flow (van der Hoorn et al., 2012), which is presumably the result initiated by the Kellwasser Event.

Well	Porosity [%]	Permeability [mD]	Depth [m]	Reference
LTG-01	< 2	0 - 9	4303-5070m	(van Hulten and Poty, 2009)
UHM-02	< 4	0.04	4682-5344m	(Gutteridge, 2002; IF, 2012)
WSK-01	1.6	0.2	4180-4399m	(nlog, 1978; IF, 2012)
CAL-GT-01	0.5 - 20	5-200	1802-2706m	(nlog, 2012; TNO, 2015)
Merksplas-Beerse	2 (max 20)	2000-3000	1630-1761m	(Vandenberghe, 2000)

Table 1 : Overview of porosity, permeability and depth of the Dinantian at the specified well locations.

During the Devonian this event caused the extinction of carbonate producing organisms. This led to the absence of skeletal framework reef-building organisms, resulting in a poor matrix porosity as a result of burial and compaction of the lime-muds (Total, 2007; Reijmer, 2017). Besides the non-skeletal organisms, the depositional environment has an influence on the porosity and permeability. Reijmer (in Hoornveld, 2013), suggested a lower porosity at the platform flat compared to the slope as a consequence of the low energetic environment. On top of that, microbes formed steep platform slopes, which became unstable resulting in fractures. Therefore the reservoir permeability is assumed to be higher at the platform ramp due to these fractures (Hoornveld, 2013).

High local porosity and permeability values within the Dinantian are only found in the relative shallow subsurface. Within the LTG-01 and UHM-02 no high porous or permeable features are encountered. The higher porosity and permeabilities are only confirmed at karst features and fracture zones. From this it can be concluded that no sufficient fluid flowrates can be obtained within the non-fractured and non-karstified Dinantian formation.

2.5. Seismic Data

Detailed seismic data are useful to map the presence and exact locations of carbonate platforms and slopes to target the potential reservoir more accurately. High quality 3D seismic in the northern onshore part of the Netherlands has already led to the interpretation of the Friesland High, Groningen High and Lauwerszee Trough (Kombrink et al, 2010.). However, due to a formation depth of more than 4000 m, high quality seismic data of the Lower Carboniferous is only locally available. In addition, seismic interpretation of the Mississippian markers is inconvenient due to the overlying Permian Zechstein evaporites, which are widely present in the subsurface of the Netherlands. Multiples generated by the Zechstein formation are hard to distinguish from the Carboniferous reflections and Westphalian coal layers also impede the interpretation of the formation (Kombrink, 2008)

2.6. Sample Location

The Carboniferous Limestone rock samples used in this research are taken from the Kornelimunster quarry operated by Lambert Hoven GmbH & Co. (Figure 2.6). This quarry, located East of Aachen, mines limestone from the Lower Carboniferous (Figure 2.6). Two different carbonate rocks are present in this quarry: the "Aachener Blaustein" and the "Massenkalk". The Aachener Blaustein is a partly dolomized rock and the Massenkalk is a

limestone (from G.R. Geel, TNO). The rock samples investigated in this study are Aachener Blaustein and presumably originated during the Tournaisian. Besides, this area is close to the transition between the shallow marine carbonates and the deep sea Culm facies. In order to identify the exact rock type of the rock samples, thin sections have been analysed by an optical microscope and a scanning electron microscope (EPMA).



Figure 2.6: Location of the Kornelimunster quarry, the quarry the rock samples are collected (Left). The more zoomed location including the geological formations at surface (Right).

3

Methodology

To quantify the characteristics of the Lower Carboniferous limestone, a variety of laboratory experiments have been performed. In this chapter all experiments that contribute to the mechanical, hydraulic and fracture characterization are described. The physical background, methodological approach and obtained parameters for each individual experiment are clarified.

3.1. Rock Specimen

In total 34 rock samples were prepared and tested using different experimental setups and are named with a unique code (Table 2). The samples are all from the same block and were drilled *parallel* (x/y-direction) or *perpendicular* (z-direction) to the bedding (Figure 3.1). No distinction is made between the lateral orientation (x- and y-direction) of the samples, since the same lateral direction have been used for all parallel cores. The investigated rock samples in this study are assumed to be intact and coherent without any macroscopic irregularities, unless otherwise specified.

To quantify the effect of a multiple fracture structure, the hydromechanical effect of a single fracture needs to be studied. Therefore, all performed fracture experiments are based on one single fracture within an intact rock.

Cylinders with a diameter of 50 mm or 25 mm were drilled using water as lubricant from three sub-blocks in the laboratory of GFZ Potsdam. Afterwards, the sample's end faces were ground plan-parallel in order to obtain parallel ends and the right core length. Prior to testing all specimens were placed in an oven and dried for at least 24 hours at 50 °C. In Appendix A a detailed overview of all the rock samples and specific dimensions is given.

Rock type	Rock name	Year	Location	Sample block	Sub block	Sample no.	Orientation
<i>C</i>	<i>KO</i>	<i>6</i>	<i>AA</i>	<i>01</i>	<i>03</i>	<i>07</i>	<i>p</i>
Carbonate	Kolenkalk	2016	Aachen	Big block	Large core		Parallel (p) or perpendicular (s)

Table 2: Rock specimen name determination.

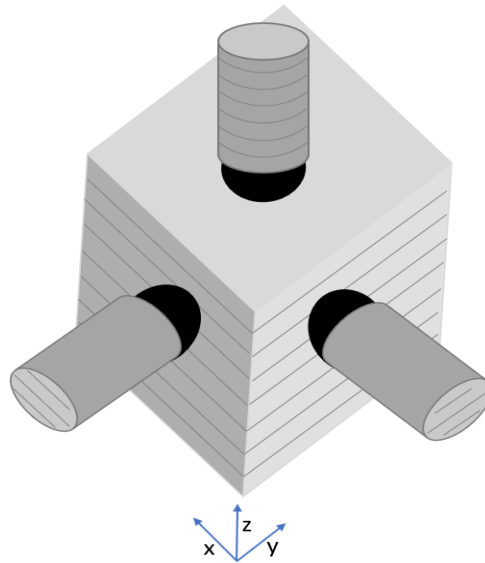


Figure 3.1: Different orientations of the drilled core samples. The perpendicular (s) cores are drilled in the z-direction, the parallel (p) cores are drilled in either the x- or y-direction.

3.2. Rock Parameters

In Table 3 all the used methods to determine the various parameters are listed. The mentioned parameters can be subdivided in mechanical parameters and hydraulic parameters. The mechanical properties, consisting of unconfined compressive strength, confined compressive strength and tensile strength are important to define the specific failure criteria. The elastic moduli, the Poisson's ratio and Young's modulus, reflect the ability of the rock to deform elastically. The fracture toughness of both mode I and mode II describes the propagation of existing fractures, as this is of high importance in a natural fractured reservoir. In terms of reservoir potential, the permeability and porosity are the key parameters: describing the reservoir rock capacity with regard to the fluid continence.

Parameter	Unit	Method
Mechanical		
Matrix density	kg/m ³	Helium Pycnometer
Pore size distribution	mm	Mercury Intrusion Porosimetry
Tensile Strength	MPa	Brazilian Test
Unconfined compressive strength	MPa	Uniaxial compression test
Poisson's ratio	[-]	Uniaxial compression test &
Young's modulus	GPa	Ultrasonic measurements
Bulk modulus	MPa	
Failure angle	rad	
Internal friction coefficient	[-]	Triaxial compression test
Cohesion	MPa	
Fracture toughness (mode II)	MN/m ^{1.5}	Punch through shear
Fracture toughness (mode I)	MN/m ^{1.5}	Brazilian Test
Hydraulic		
Porosity	[-]	Helium Pycnometer Hydrostatic weighing Mercury Intrusion Porosimetry
Permeability	Darcy	Fluid flow through Gas flow through

Table 3: Overview of rock parameters and the used methods.

3.3. Mechanical Testing System (MTS)

All tensile, uniaxial and triaxial strength tests as well as some hydraulic tests were performed using the MTS 815 apparatus (Figure 3.2). This mechanical testing system (MTS) is a servo controlled compressive machine with 2000 kN axial loading capacity. The apparatus consists of a stiff loading frame with a closed triaxial cell, a set of independently operating Quizix 6000-Series pumps for a fluid flow and a data-monitoring and acquisition system. In situ conditions can be simulated by hydrostatic pressures up to 140 MPa and temperatures up to 150 °C using oil as the confining medium. The axial strain and lateral strain of the core samples are measured by two Linear Variable Differential Transformers (LVDTs) and a circumferential chain extensometer, respectively. The resolution of the vertical and circular extensometer is $1 \cdot 10^{-3}$ mm resulting in a axial strain resolution of $2 \cdot 10^{-5}$ mm/mm and a lateral strain resolution of $1 \cdot 10^{-6}$ mm/mm. The temperature is continuously monitored by two thermocouples, installed at the top and bottom of the specimen.

Pore pressure is simulated by the use of two independent up- and two downstream Quizix pumps (Figure 3.2). These pumps operate in constant pressure or constant flow rate mode and monitor accurately the volume change of the sample as a result of changing temperature or stress. The pressure difference over the sample is determined by a differential pressure sensor in the range of 0.01 to 1 MPa. The recording frequency for both the MTS and Quizix system was 1 s^{-1} .

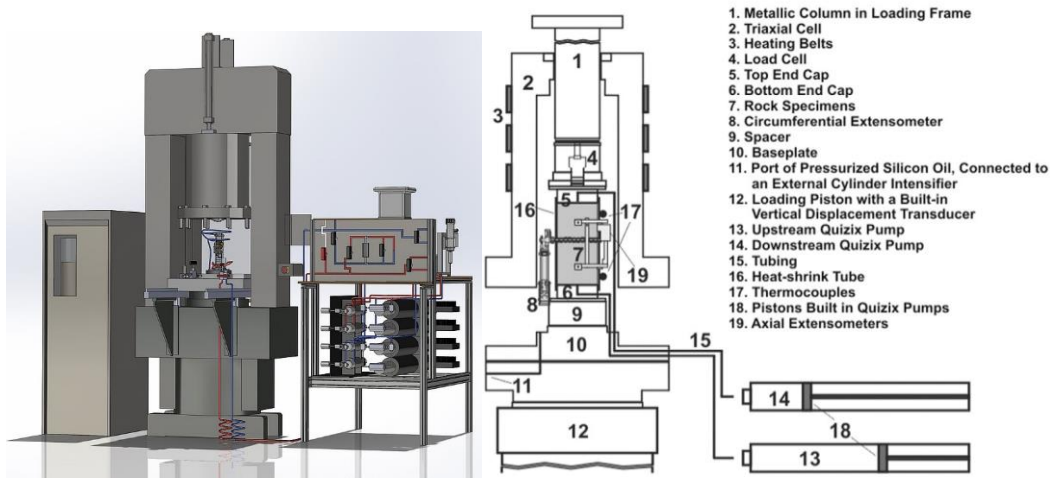


Figure 3.2: Schematic overview of the MTS (Left) and a cross sectional overview of the triaxial cell and its connection with Quizix pumps (Pei, 2016).

3.4. Mechanical Characterization

3.4.1. Brazilian Tensile Strength test

The Brazilian tensile strength test measures the tensile strength of an intact rock and the mode I fracture toughness (K_{IC}). It is designed to apply uniaxial compression on a thin circular disc of rock. The disc is placed between two parallel platens and the load is directed vertical (Figure 3.3). These discs have a diameter of 50 mm and a thickness of approximately 25 mm according to ASTM Standards (ASTM, 2005). The used displacement rate was 0.001 mm/s and the experiment was performed at ambient conditions. During compression of the rock sample, failure will occur by an extensional fracture parallel to the load. The failure is due to the reached tensile stress and which is given by:

$$\sigma_3 = -\frac{2P}{\pi Dt} = -T_0 \quad (1)$$

where σ_3 is the minimum axial stress at failure [MPa], P the maximum applied load [N], t the thickness of the specimen [mm], D the diameter of the specimen [mm] and T_0 the tensile strength of splitting. The maximum tensile stress appears in the centre of the disc and propagates outward (Hondros, 1959) and therefore the failure initiates at the centre of the core. Differently oriented samples are tested to determine the orientation dependency of the rock. Besides the tensile strength, the Brazilian test is a proposed method to measure the rock fracture toughness. It is a function of load P [N], specimen geometry B and the intensity factor coefficient $\Phi(c/R)$ as described by Guo et al. (1993).

$$K_{IC} = B * P * \Phi\left(\frac{c}{R}\right) \quad (2)$$

$$B = \frac{2}{\pi^2 * R^2 * t * \alpha} \quad (3)$$

where R is the radius of the disc [m] and α corresponds to the arc distance. The arc distance is the contact length between the sample and the jaw and is in this case 5° . Figure 3.4 shows the stress intensity factors and their dependency on the variable α . The $\Phi(c/R)$ is 0.112 and is established from the maximum value of the $\alpha = 5^\circ$ curve.

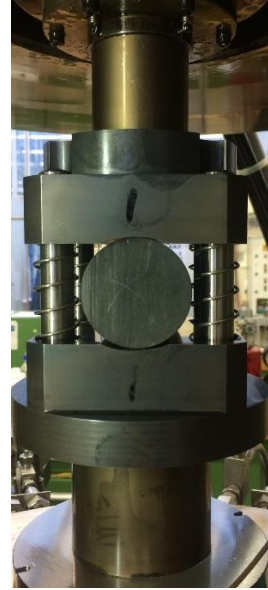
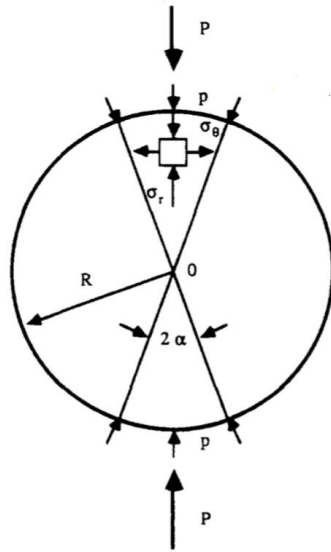


Figure 3.3: Left: Schematic overview of diametral compression during Brazilian disc test (Guo, 1993). Right: the experimental setup of the Brazilian disc test within the MTS.

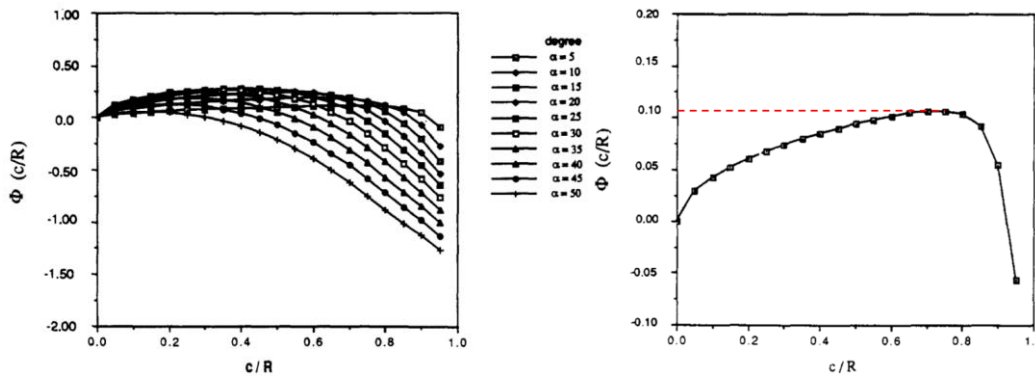


Figure 3.4: Stress intensity factors as a function of dimensionless crack length for different α (left) and the Stress intensity factor as a function of dimensionless crack length for only $\alpha = 5^\circ$ scenario (right).

3.4.2. Unconfined Compressive Strength Test

The unconfined compressive strength (UCS) test is an experimental test to determine three different characteristics of a rock sample: unconfined compressive strength, Young's modulus and Poisson ratio. Unsaturated cylindrical samples of 100 mm in length and 50 mm in diameter are placed in a shrink tube to protect the extensometers from debris. The membrane effect, suggested by the British Standard Institution (1990), is assumed negligible for the UCS testing. During the test the bottom plate of the MTS moves up at a displacement rate of 0.0002 mm/s and thereby loads the rock sample. The apparatus monitors the load and both the axial and lateral displacement by extensometers. The two axial extensometers are placed vertically on the opposite direction of the sample and the circumferential extensometer is placed at the middle of the sample. All UCS tests are performed at room temperature (21 - 23 °C).

The UCS describes the maximum axial load an unconfined cylindrical specimen can withstand before permanent deformation occurs. The axial stress σ_a [MPa] is the axial force F_a [N] per unit area A [mm²] applied on the rock sample, therefore the UCS can be deduced from the maximum applied force per area eq. (4).

$$\sigma_a = \frac{F_a}{A}, \quad UCS = \frac{F_{max}}{A} \quad (4)$$

The Poisson's ratio ν , a dimensionless parameter, describes the ratio of the lateral strain to the axial strain within the linear elastic region by:

$$\nu = -\frac{\text{Strain in direction of load}}{\text{Strain perpendicular to load}} = -\frac{\epsilon_l}{\epsilon_a} \quad (5)$$

Where the axial strain ϵ_a is a dimensionless parameter describing the axial displacement ΔL [m] over the length L_0 [m] of the cylindrical core:

$$\epsilon_a = \frac{\Delta L}{L_0} \quad (6)$$

Assuming a uniform strain distribution within the lateral direction, the lateral strain ϵ_l is equal to the circumferential strain ϵ_c derived from the circumferential extensometer:

$$\epsilon_c = \frac{\Delta C}{C_0} = \epsilon_l \quad (7)$$

Where ΔC is the change in circumference [m] and C_0 the original circumference [m].

The Young's modulus E [MPa] describes the rigidity or stiffness of a specimen i.e., the tendency to deform along the axis of the applied opposing forces. In eq. (8) the Young's modulus is described as the axial stress divided by the axial strain. The greater the Young's modulus the stiffer the material.

$$E = \frac{\text{axial stress}}{\text{axial strain}} = \frac{\sigma_a}{\epsilon_a} \quad (8)$$

3.4.3. Triaxial Compressive Test

A triaxial compression (or confined compression) test is performed to determine the shear strength and stiffness. During the triaxial compression test a rock specimen is subjected to three principle stresses in which two of them are of equal magnitude. The third principle stress has the largest magnitude and therefore the following relation holds:

$$\sigma_1 \geq \sigma_2 = \sigma_3 > 0 \quad (9)$$

Based on three confined compression tests at different confining pressures, Mohr stress circles can be constructed. The failure points can be calculated by the maximum principle stress σ_1 , the least principle stress σ_3 and the angle of failure θ .

$$\tau_0 = (\sigma_1 - \sigma_3) \sin(\theta) * \cos(\theta) \quad (10)$$

$$\sigma_0 = \sigma_3 + (\sigma_1 - \sigma_3) \cos^2(\theta) \quad (11)$$

Where θ is the angle between the maximum principle stress and the fracture plane. The construction of Mohr failure criterion is explained in more detail in Appendix D.

The cylindrical rock samples of 100 mm height and 50 mm diameter are placed vertically between two end caps and surrounded by a heat shrink tube (Figure 3.5). First, the sample

is put under vacuum for around 24 hours to reach a pressure of ~ 1.2 kPa. Afterwards the chamber is filled with oil and the confining pressure is increased to 2 MPa. Saturation is performed by a pressure controlled fluid flow (0.2 MPa) at one side of the sample. After the sample is fully saturated, a constant flow rate is applied for around 48 hours. Finally the confining pressure is increased to either 20, 30, 40 or 50 MPa. During the confinement ramp of 12 MPa/hr, either a constant flow rate is applied to determine the permeability, or the volumetric change is monitored by setting a constant pressure at both sample ends (see 3.5.5).

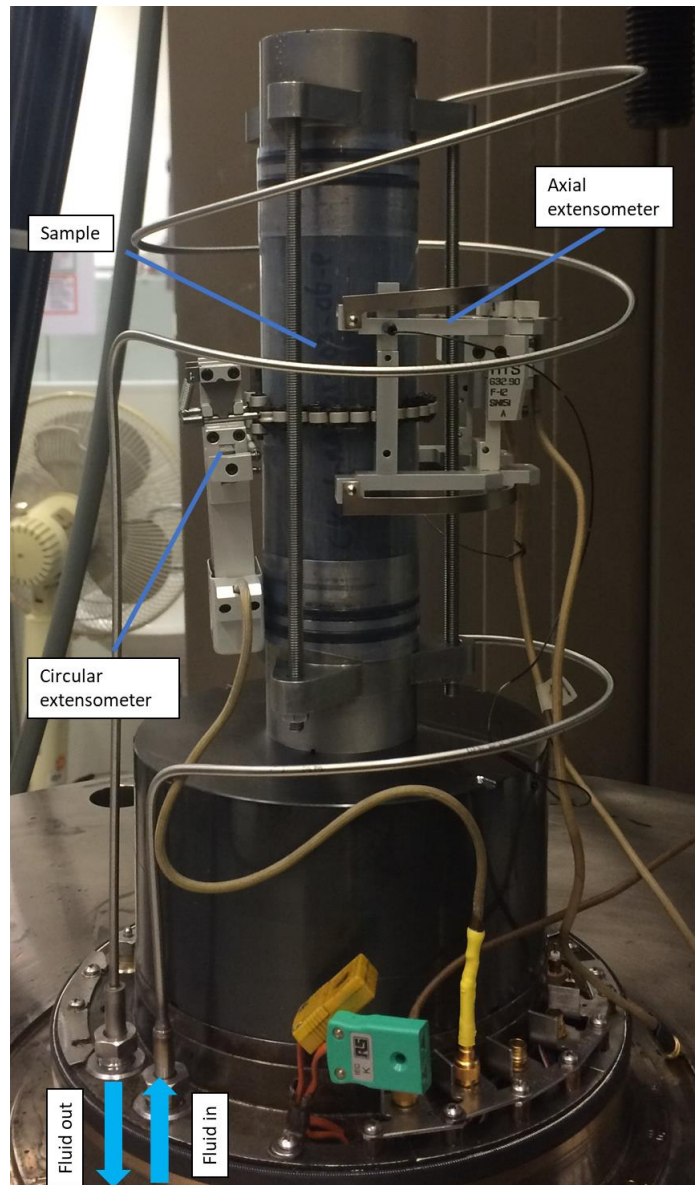


Figure 3.5: An overview of the sample prior to the triaxial test. Both circular and axial extensometers are attached to the sample.

After a relaxation period, axial loading is performed at a rate of 0.0004 mm/s and at a constant pore pressure of 0.1 MPa. During the axial loading, the vertical and lateral strain is monitored by the extensometers. Pore volume change is monitored by the amount of fluid that is squeezed out. After the failure of the sample, axial loading was continued for around 0.15 mm to displace the formed shear fracture which is explained in more detail in (3.6.2).

3.4.4. Acoustic Measurements

Besides the determination of the elastic moduli by a static method (3.4.2), a dynamic method is used to determine the elastic moduli. A commonly used method is to subject the rock sample to compressional (P) and shear (S) waves. Based on the density and the transit time of both the p-wave and s-wave, the Young's modulus and Poisson's ratio can be obtained:

$$v = \frac{V_p^2 - 2V_s^2}{2(V_p^2 - V_s^2)} \quad (12)$$

$$G = \rho v_s^2 \quad (13)$$

$$E = 2G(1 + v) \quad (14)$$

Specific p-wave and s-wave transducers measure the wave velocity through the sample. Both transducers are placed at the top and bottom of the sample (Figure 3.6). To guarantee fully contact between the transducers and the sample, a special paste is smeared on both transducers. A frequency of 1 MHz is used for both the p- and s-wave. To create the same conditions compared to the static derived moduli, unsaturated samples are used and the test is performed at ambient conditions.



Figure 3.6: Overview of the setup during ultrasonic p- and s-wave measurements.

3.5. Hydraulic characterization

3.5.1. Helium Pycnometer

The matrix density and effective porosity of a rock sample are determined using a helium gas pycnometer. Helium is used since it can be considered as a non-absorbing ideal gas at standard temperature and pressure (Weber and Bastick, 1968). The pycnometer consists of two chambers: one with the sample and an empty reference chamber (Figure 3.7). The sample chamber is pressurized to P_1 . After a stable pressure is reached a valve to the empty cell is opened, resulting in a lower pressure P_2 . Based on the known chamber volumes the gas pycnometer measures the matrix volume (V_{ma}):

$$V_{ma} = V_c + \frac{V_r}{1 - \frac{P_1}{P_2}} \quad (15)$$

Since the mass and total volume of the rock sample are known, the matrix density and effective porosity can be calculated by:

$$\rho = \frac{M}{V_{ma}} \quad (16)$$

$$\varphi = \frac{V_t - V_{ma}}{V_{ma}} \quad (17)$$

Where ρ is the matrix density [kg/m^3], M the sample mass [kg], V_t the total sample volume [m^3] and φ the effective porosity [-].

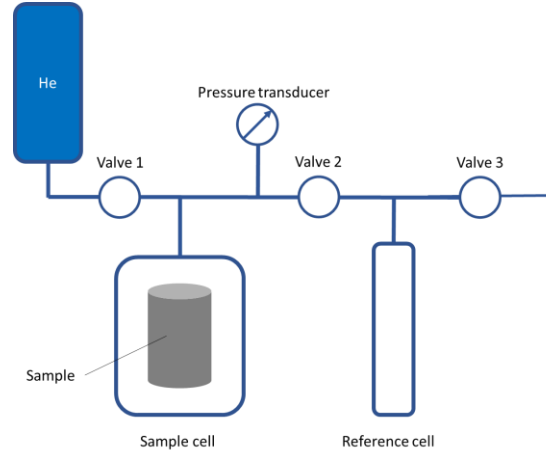


Figure 3.7: Schematic overview of the Helium pycnometer

According to Tamari (2004) the gas pycnometer can determine the volume of the rock matrix with a relative uncertainty of $\leq 0.2\%$. However, the largest uncertainty arises from measuring the bulk volume. Based on an error of 0.05 mm in both the length and diameter, the bulk volume uncertainty is already $\sim 0.5\%$.

3.5.2. Hydrostatic weighing

The porosity is also determined based on the dry and wet weight of the sample. First the dry sample weight is measured. Subsequently, the samples are put under vacuum (0.6 kPa) and saturated in a water bath. After full saturation the porosity could be determined by eq. (18).

$$\varphi = \frac{\left(\frac{m_{bulk} - m_{grain}}{\rho_{water}}\right)}{V_{bulk}} = \frac{V_{pores}}{V_{bulk}} \quad (18)$$

The uncertainty in this experiment is mainly due to measuring the sample dimensions (0.05 mm), resulting in a porosity uncertainty of 0.36%.

3.5.3. Mercury Intrusion Porosimetry

Mercury intrusion porosimetry (MIP) is an experimental technique used for the characterization of pore size distribution. By penetrating mercury into the pores of a specimen, the volume of penetrated liquid metal as a function of pressure is measured. The mercury volume that intrudes at each pressure increment, corresponds to the volume of pores of each size class. Since mercury is a non-wetting fluid, an externally imposed pressure is required to intrude the liquid into the pores of the rock sample. The relationship between the imposed pressure P [Pa] and the capillary radius is described by Washburn (1921):

$$P = \frac{-2\gamma \cos \theta}{r} \quad (19)$$

Where γ is the interfacial energy of mercury [N/m] , θ the contact angle of mercury with the material [°] and r the pore radius (assuming cylindrical pores) [m]. For the interfacial tension energy and the mercury contact angle, the common values of 0.485 N/m and 140° are used, respectively. Besides the determination of the pore size distribution, the total porosity is determined from the total intruded volume mercury. It is measured by a mercury penetrometer (an electrical capacitance dilatometer) and has an accuracy of 0.1 μL .

Although the MIP is a widely used technique for the determination of pore distribution, it does not measure the true pore sizes, since large internal pores are only accessible via narrow throats. This misinterpretation is called: the "ink bottle" effect and is identified by monitoring the mercury extrusion during depressurizing the rock sample. Moreover, microstructural damage caused by mercury porosimetry and the rock drying process have a major effect on the determined MIP (Olsen et al., 1997; Moro and Böhni, 2001). A proper interpretation of the pore size distribution by only using MIP is not recommended. Another technique that can be used to quantify the pore size distribution is X-ray Computed Tomography (XRCT) (Lawrence, 2017).

3.5.4. Gas Permeameter

The gas permeameter determines the permeability of a rock specimen based on Darcy's law. The steady state and pressure pulse methods are used to determine the sample's permeability. A cylindrical rock sample with a height of 40 or 50 mm and a diameter of 25 mm is put in a neoprene rubber jacket. Afterwards, the sample is placed in a hollow steel cylindrical chamber (Figure 3.8). Between the specimen and the threaded steel cylinder there is a space for hydraulic fluid to adjust the confining pressure. The recording frequency of the pressures and flow rates is 0.1 s^{-1} .

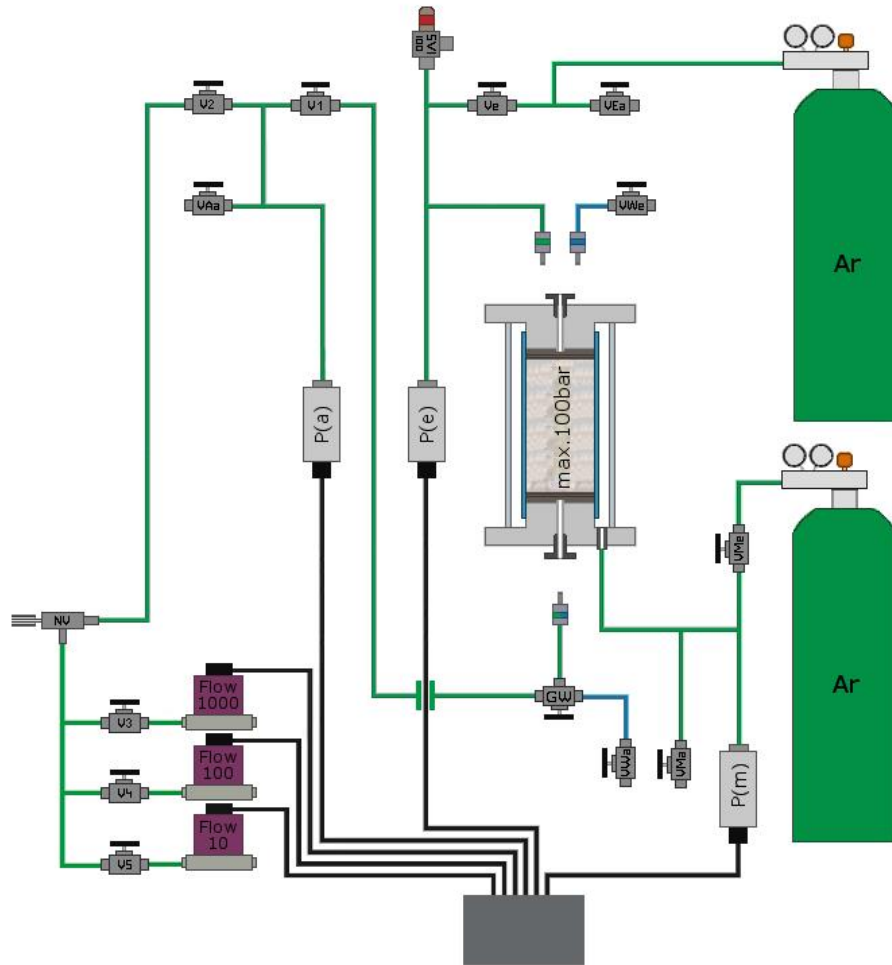


Figure 3.8: Schematic overview gas permeameter: P(e) is the inlet pressure, P(a) the outlet pressure and P(m) the confining pressure. Different flow gauges can control the flow rates, with their maximum flow rate indicated (mL/min). Argon is used for the confining pressure as well for the flowing medium (from Milsch, GFZ).

By controlling the flow and setting a constant confining pressure of 5 MPa and an outlet pressure of ~ 0.15 MPa, the inlet pressure at the top of the sample is monitored over time. After achieving a constant inlet pressure at a certain flow rate, the flow rate is increased for the next step. In total four steps of different flow rates are performed to obtain the permeability. The intrinsic permeability is described by Darcy's law by:

$$k = -\frac{Q\mu dL}{A dP} \quad (20)$$

where Q is the flow rate [m^3/s], A the cross sectional area of the flow [m^2], k the intrinsic permeability [m^2], μ the viscosity of the pore fluid [$\text{Pa}\cdot\text{s}$], dP the pressure difference between the top and bottom of the specimen [Pa] and dL the length of the rock specimen [m]. Eq. (20) only holds for liquid fluids. For the use of gas, there are mainly two complications: compressibility and gas slippage. Gas is a compressible fluid and the application of high pressure during the gas permeameter test causes compression. The modified flow equation for compressible fluids is expressed by:

$$Q = -A \frac{k_{gas}}{\mu L} \frac{(P_{in}^2 - P_{out}^2)}{2P_{out}} \quad (21)$$

Klinkenberg (1941) discovered a higher gas permeability with respect to liquid permeability and attributed this to the slippage of gas molecules along grains. In comparison to a liquid, the average velocity of gas in the vicinity of pore walls is nonzero and therefore contributes to the flow. The Klinkenberg correction translates the gas permeability obtained by equation (21) into the equivalent liquid permeability by:

$$k_{gas} = k_{liquid} \left(1 + \frac{b}{P} \right) \quad (22)$$

$$b = \left(\frac{c\kappa T}{\pi\sqrt{2}r^3} \right) \quad (23)$$

Where b is the Klinkenberg slip factor (Pa), P the average pressure of the sample (Pa), c a constant, T the temperature (K), r the sample radius and κ the Boltzmann's constant (JK^{-1}). For high pressures the second term of equation (22) becomes negligible and the liquid permeability is equal to the gas permeability if $2/(P_{in}+P_{out}) = 0$. Extrapolation of the k_{gas} is performed by linear extrapolation.

Based on a maximum pressure difference of 5 MPa and a minimum measurable flowrate of 0.02 mL/min, this method can measure the permeability down to 10 nD. In addition to the steady state method, the pressure pulse method is examined and performed to manifest the correlation between both methods (see Appendix I).

3.5.5. Hydraulic Response in the Triaxial Cell

Prior to the uniaxial loading of the samples within the triaxial cell, either the permeability or the volume change is monitored during an increasing confining pressure.

Permeability

Permeability is tested prior to the axial loading with the MTS. Different confining pressures and larger sample dimensions are used compared to the gas permeameter. The permeability determination is based on Darcy's law by the flow of distilled water. The permeability is determined for all samples at a confining pressure of 2 MPa and a fixed outlet pressure in the range of 0.1 to 0.2 MPa. Constant flow rates were in the order of 0.001 to 0.01 ml/min.

To quantify the effect of the effective pressure on the permeability, a constant flow is applied during the increase of confining pressure for two samples. The effective pressure is determined based on the effective pressure theory of Terzaghi (1936):

$$P_{eff} = P_{con} - P_{pore} \quad (24)$$

Where the mean pore pressure is assumed as:

$$P_{pore} = P_{out} + 0.5(P_{in} - P_{out}) \quad (25)$$

Until the limit of the differential pressure sensor was reached (1 MPa), the permeability could be monitored as a function of effective pressure.

Volume change

The squeezed out fluid volume is monitored during an increasing confining pressure and at a constant pore pressure of 0.1 MPa. Since this squeezed out volume is equal to the pore volume reduction, the porosity change at different confining pressure is determined. From both the circular and axial extensometers the volumetric strain and therefore the change in bulk volume as a function of effective pressure is obtained. The relation of the bulk volume change and pore volume change is described by the Biot's coefficient α :

$$\alpha = \frac{dV_{\varphi}}{dV_b} = \frac{dV_{\varphi}}{V_b de_v} \quad (26)$$

The change in bulk volume is the sum of the change in pore volume and matrix volume. Since both matrix and pore volume decrease with increasing effective pressure, the Biot's coefficient is less or equal than one.

3.6. Fracture Characterization

3.6.1. Punch-Through Shear Test

Besides tensile fractures, shear fractures appear at the subsurface under specific stress conditions. The mode I fracture toughness describes the stress intensity necessary to initiate and propagate a tensile fracture, determined by the Brazilian disc test (3.4.1). A testing method to determine the mode II fracture toughness (K_{IIC}), the critical stress concentration to initiate and propagate a shear fracture, is determined by the punch-through shear (PTS) test. This test, introduced by Backers (2012) and ISRM listed, creates a shear fracture by vertically loading a sample with prefabricated fractures (Backers, 2012). Besides the K_{IIC} , the evolution of the fracture permeability can be investigated by this method.

For the experimental setup, cylindrical rock samples with a height of 50 mm and a diameter of 50 mm are used. Circular notches with a depth of 5 mm and 15 mm are drilled into the center of top and bottom surfaces of the sample (Figure 3.9). The notch depths differ in comparison to the method of Backers et al. (2002), who used a bottom depth of 30 mm. According to Backers (2012), it is considered this has no effect on the K_{IIC} relation. A circular ring at the top notch is placed in order to prevent deformation of the inner cylinder. The sample is placed between a load stamp and a bottom supported assembly, surrounded by a heat shrinking tube (Figure 3.10). The whole assembly is installed in the MTS including the circular extensometer to monitor the lateral strain.

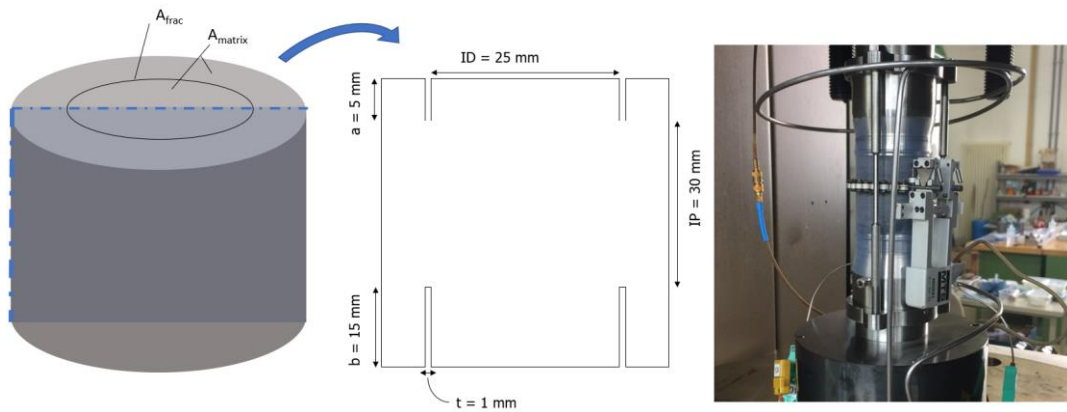


Figure 3.9: Left: 3D visualization of the sample used for the PTS tes. Middle: a cross section including the dimensions of the PTS sample. Right: The PTS sample placed in the MTS surrounded by the circular extensometer.

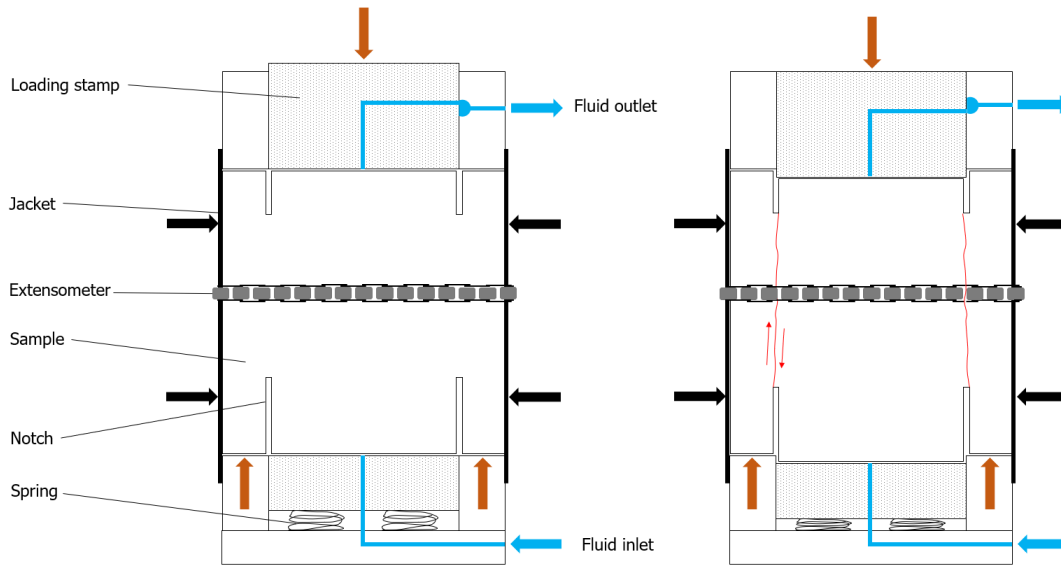


Figure 3.10: Overview of PTS setup. Left: Initial stress state before the axial loading. Right: situation after applying the axial load to the sample.

After the saturation process (see 3.4.3), both confining pressure and pore pressure are increased simultaneously in order to increase the effective pressure gradually. To simulate subsurface effective pressure conditions, a final confining pressure of 40 or 60 MPa and a pore pressure of 20 MPa is applied to the sample. A constant pressure difference between the inlet and outlet is set at 0.5 MPa in order to monitor the permeability evolution. The loading piston moves up until an axial force of 2 kN is reached. With a displacement rate of 0.01 mm/min, the loading stamp starts to push the inner cylinder downwards, resulting in a vertical stress build-up.

At a certain vertical stress, a fracture starts to grow from the bottom notch to the upper notch (Figure 3.10). After full development of the fracture, the vertical load reaches its maximum level F_{max} . The mode II fracture toughness can be evaluated from the achieved maximum load and the effective pressure by (Backers, 2012):

$$K_{IIC} = 7.74 * 10^{-2} F_{max} - 1.80 * 10^{-3} P_{eff} \quad (27)$$

After failure of the sample, displacement is continued with the same displacement rate to the maximum of 1.2 mm.

Permeability

The PTS experiment gives the opportunity to analyse the effect of a shear fracture on permeability. Prior to axial loading, the intact rock permeability is determined based on steady state flow at an effective pressure of 2 MPa. After full development of the shear fracture, the total permeability is measured as a function of fracture displacement. This permeability is the result of the matrix permeability and the fracture permeability. Assuming the intact matrix permeability remains constant, the fracture permeability is derived by using arithmetic averaging:

$$k_{frac} = \frac{(A_{frac} + A_{matrix})k_{total} - A_{matrix} * k_{matrix}}{A_{frac}} \quad (28)$$

where the fracture area is determined based on the fracture aperture thickness and circular length. The aperture thickness is derived from the lateral strain and CT images, which is explained in more detail in the next paragraph.

Afterwards, at a fixed fracture displacement of 1.2 mm, the influence of different effective pressures on the permeability is monitored. To simulate pressure changes in the reservoir, the pore pressure of the PTS sample is varied by 5 MPa. Besides monitoring the permeability, the lateral strain can be obtained from the circular extensometer.

By increasing and decreasing the pore pressure, it is assumed the effective pressure changes according to the effective pressure law. An increase of effective pressure presumably leads to a further closure of the fracture, resulting in a lower fracture permeability. On the other hand, a decrease of the effective pressure shows the opposite (Walsh, 1981). This increase and decrease of the pore pressure, a so-called pore pressure cycle, is repeated three times.

A different approach to obtain the fracture permeability is described by the cubic law. It is a simplified relation between the aperture thickness and the fracture permeability, assuming smooth-wall fractures with a uniform aperture over the total length of the fracture, and is described as:

$$k_{frac} = \frac{a^3}{12} \quad (29)$$

Where k is the permeability [m^2] and a the fracture aperture [m].

Aperture thickness

The permeability of a fracture is dependent on the mean aperture of the fracture. Based on the continuous strain measurements of the circular extensometer, the aperture can be determined as a function of effective pressure and fracture displacement. Assuming the aperture is zero at the maximum axial load, the aperture is described as a function of the lateral strain.

$$a = \frac{Diameter_{Fmax}}{2} * (Strain_{Fmax} - Strain_{lat}) \quad (30)$$

Within a pore pressure cycle, the change in effective pressure causes an expansion or a compression of the rock sample. Therefore, the strain measured by the circular extensometer is a combination of the lateral strain of the rock matrix and the change in aperture. Eq (30) is corrected for the former effect by incorporating the relation between effective pressure and elastic strain of the intact material. Since the PTS samples are all oriented in the z-direction, the strain is derived from the CKO6-AA-01-02-08s sample (Figure 3.11).

$$a_{corrected} = a + \frac{Diameter_{Fmax}}{2} * P_{eff} * 2.24 * 10^{-5} \quad (31)$$

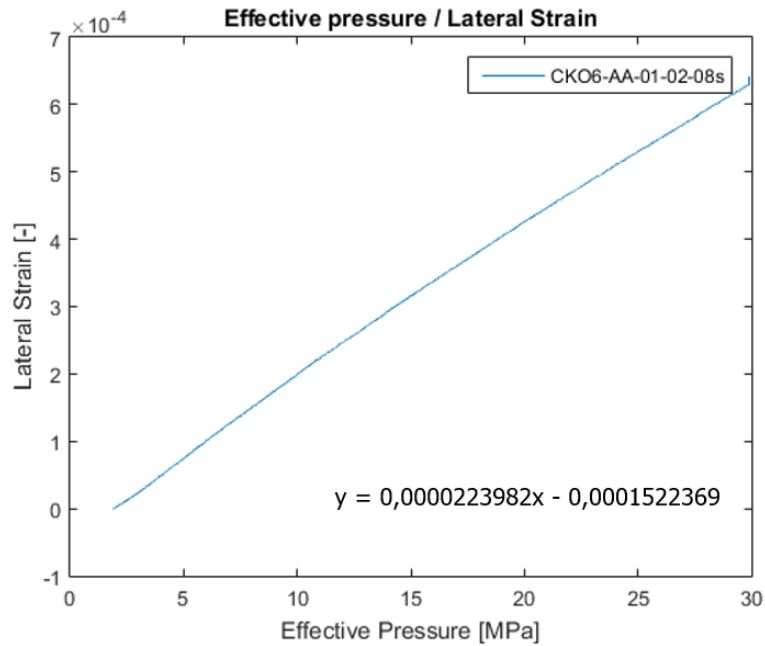


Figure 3.11: Lateral strain as a function of effective pressure. The lateral strain is monitored during a confining pressure ramp from 2 until 30 MPa. Effective pressure is derived from the effective pressure law.

3.6.2. Triaxial Induced Shear Fracture

The triaxial compressive test (3.4.3) initiates a shear fracture at the maximum axial load. The fracture cuts both the top and bottom ends allowing a flow along the fracture (Figure 3.12). After a vertical fracture displacement of ~ 0.15 mm, a constant pressure difference over the sample is applied to obtain the permeability. A slowly decreasing confining pressure ramp and a constant pore pressure of ~ 0.2 MPa is set to obtain the permeability as a function of effective pressure.

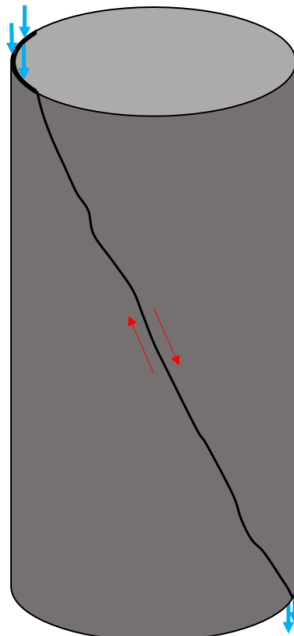


Figure 3.12: Schematic overview of the steady state flow through the triaxial induced fracture.

During the decrease of effective pressure, both the expansion of the sample and the opening of the fracture are monitored by the circular extensometer. The expansion of the sample is elastic-strain and strongly dependent on the effective pressure (Figure 3.11). The total

strain measured by the circumferential extensometer can be described as the sum of elastic and non-elastic strain (Figure 3.13):

$$\varepsilon_{total} = \varepsilon_{non-elastic} + \varepsilon_{elastic} \quad (32)$$

During the decrease of effective pressure, the change in aperture can be described as a function of the elastic strain:

$$\Delta a_h = \frac{\Delta C - \varepsilon_{elastic} * C_I}{2} \quad (33)$$

Where C_I is the circumference before hydrostatic unloading and Δa_h the aperture change in the horizontal direction. The change in circumference (ΔC) is measured by the extensometer. Since the fracture plane is not perpendicular to the circular extensometer, the horizontal aperture must be corrected for the fracture plane angle (θ) to obtain the true fracture aperture:

$$\Delta a_v = \frac{\Delta a_h}{\cos \theta} \quad (34)$$

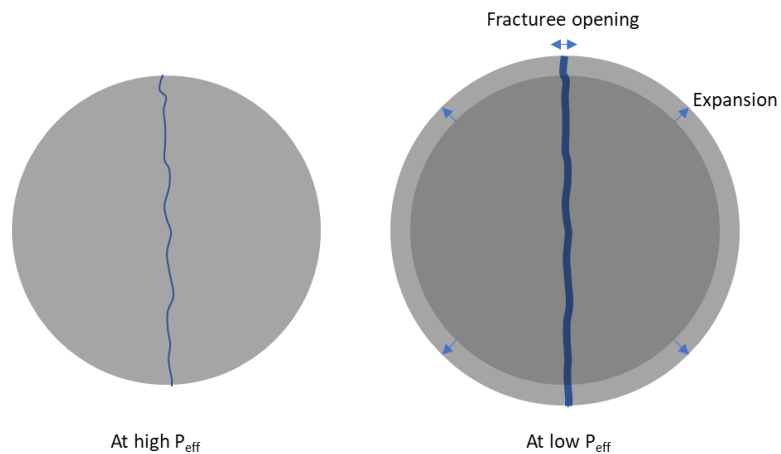


Figure 3.13: A schematic overview of the effect of hydrostatic unloading. Both expansion and fracture opening play a role. Therefore the expansion effect is corrected to determine the aperture (eqs. 34).

4

Mineralogical Characteristics

An electron probe microanalyzer (EPMA) is used to determine the mineral composition, grain size, grain geometry and microcrack structure. Within the EPMA, an electron beam is transmitted to the 30 μD thin sections. As a response, each element in the sample emits a characteristic X-ray which is detected by the electron microprobe. A high resolution image is generated which gives the opportunity to identify the textural structure on a micro scale level (1 μm). By the use of point analysis the chemical composition of almost every single mineral can be determined. However, before conducting point analyses a standard should be used to calibrate the instrument. The analyses presented in this thesis are not point analyses but back-scatter detector (BSE) spectra where the intensity of each single element is plotted in a spectrum. The resulting analyses will calculate the mineral composition norming all the oxides at 100%, not considering water which may occur in some mineral phases. The different minerals within the sample differ in their brightness related to the atomic weight of the elements forming the mineral. ImageJ software is used in order to estimate the mineral fraction of the thin sections.

CKO6-AA-01-02-13s

The thin section consists in general of calcite minerals ranging from $< 50 \mu\text{m}$ up to $300 \mu\text{m}$. The dark grey minerals are dolomite or quartz. These can be distinguished based on their edge shape: quartz minerals have sharper edges in comparison to the altered dolomite (Figure 4.1). The smaller white minerals are pyrite or iron oxides and cover only a few per cent of the total rock composition. The black material is either porosity or pyrite in case white spots are present. Around 65% of the thin section is calcite, 30% is dolomite/quartz and the remainder 5% are pores, iron-oxides and pyrite accessories. According to the Dunham classification (1962) the section can be interpreted as a wackestone/packstone.

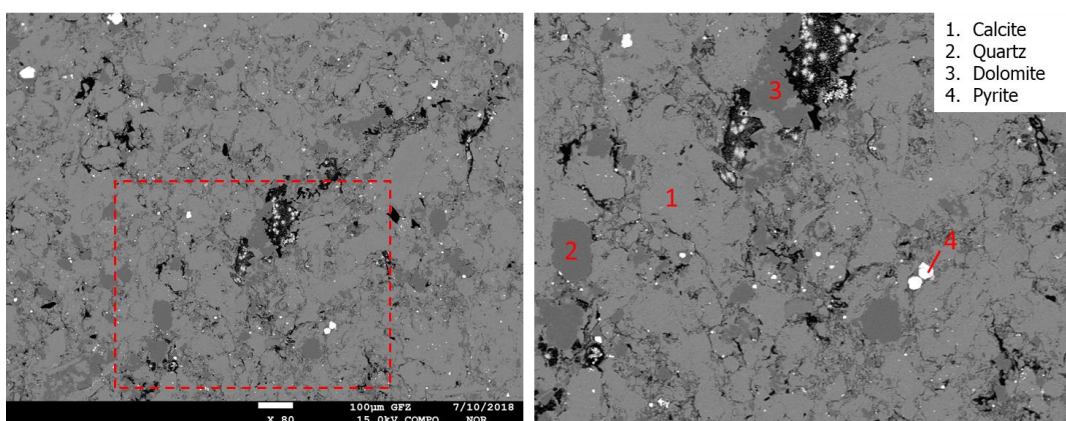


Figure 4.1: Electron microprobe image of the CKO6-AA-01-02-13s. Right: determination of the mineral composition

The CKO6-AA-01-02-13s thin section also contains a mineralized calcite fracture with a thickness of around $150 \mu\text{m}$ (Figure 4.2). The mineralized calcite is probably secondary precipitated from water circulation in the rock. Within this vein a micro-crack network, oriented parallel to the fracture, is present (Figure 4.2). The width of these cracks is in the

order of a few μm . This network only extends within the calcite vein, and no connection with the intergranular cracks in the matrix can be observed. Figure 4.2 shows the calcite vein under an optical microscope, indicating a non-displaced fracture. This part of the thin section, without considering the vein, already shows a higher calcite fraction compared to Figure 4.1.

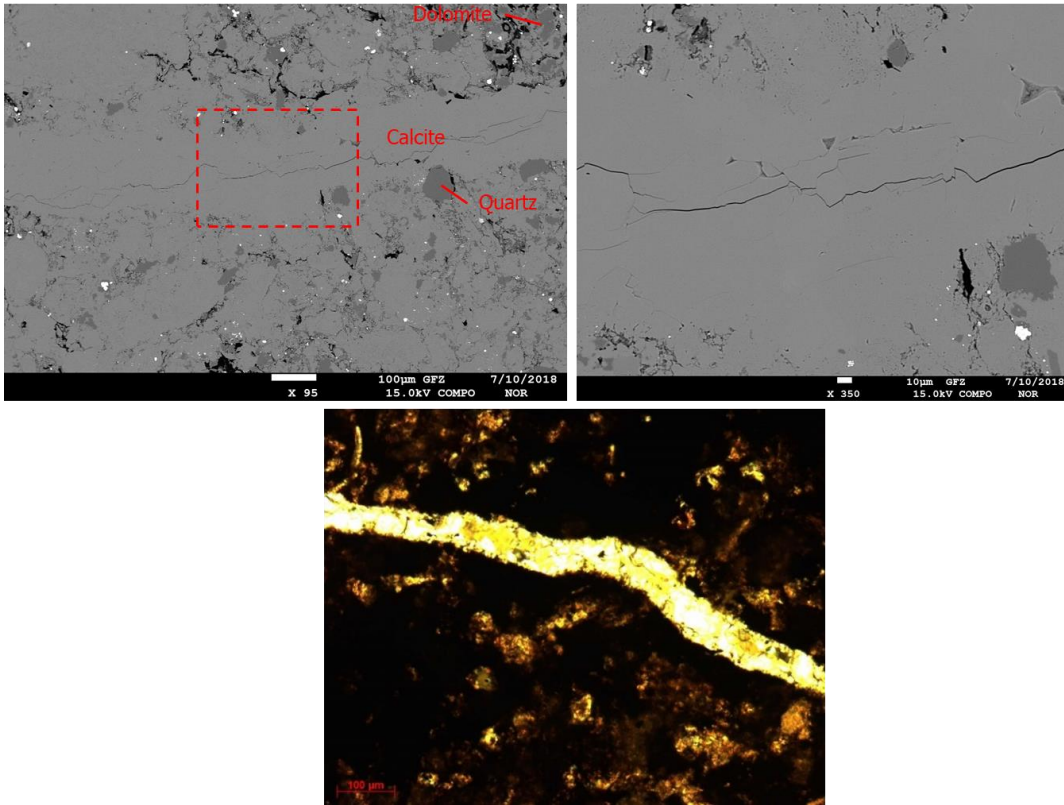


Figure 4.2: Electron microprobe image of the calcite vein within the CKO6-AA-01-02-13s (top). An image from the optical microscope shows the clearly the vein within the matrix (bottom).

CKO6-AA-01-01-19s

An alternation of larger and smaller grains with a preferred horizontal orientation shows clearly the bedding within this thin section (Figure 4.3). Within the small grain layers, significantly more dolomite and a higher porosity is present. Since dolomitization occurred along the horizontally aligned minerals, horizontal pores are formed. Porosity within the large grain layers is most likely intercrystalline porosity, initiated during the recrystallization of the carbonate fragments into calcite.

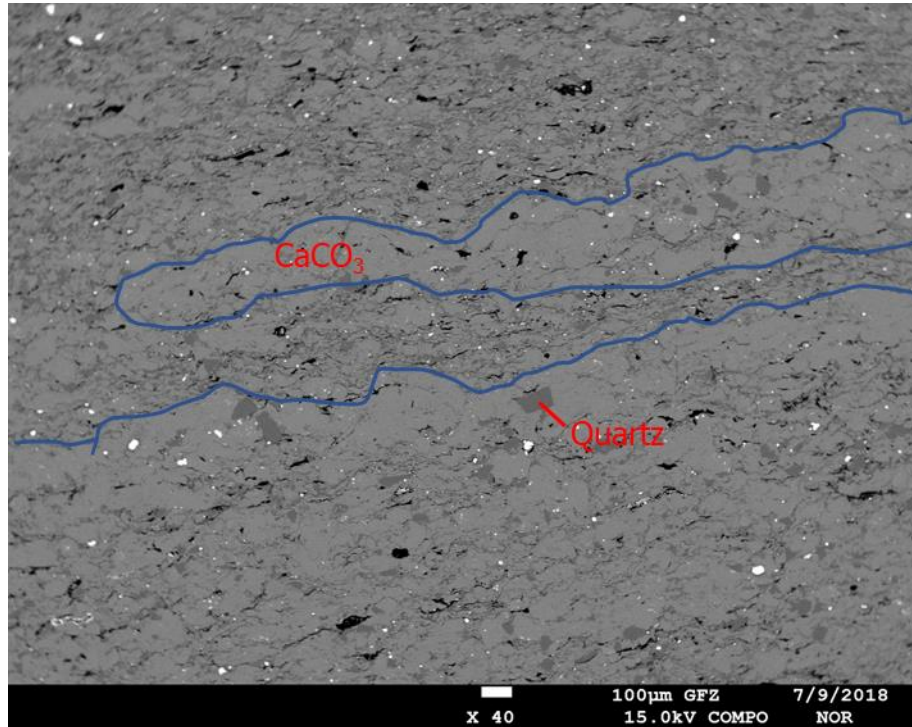


Figure 4.3 Electron microprobe image of the CKO6-AA-01-01-19s highlighting the layers of different grain sizes and mineralogy. The top part shows (partly) dolomized calcite minerals.

CKO6-AA-01-01-12spar

In contrast to the CKO6-AA-01-01-19s and CKO6-AA-01-02-13s, this thin section shows more shells and shell fragments (Figure 4.4). Grain sizes are significantly larger with a maximum up to 2.5 mm. Outer boundaries of minerals are strongly weathered and are partly dissolved. Besides the intercrystalline porosity, which is present within Figure 4.4, secondary intraparticle porosity can be identified in Figure 4.5. A brachiopod is highlighted in Figure 4.6.

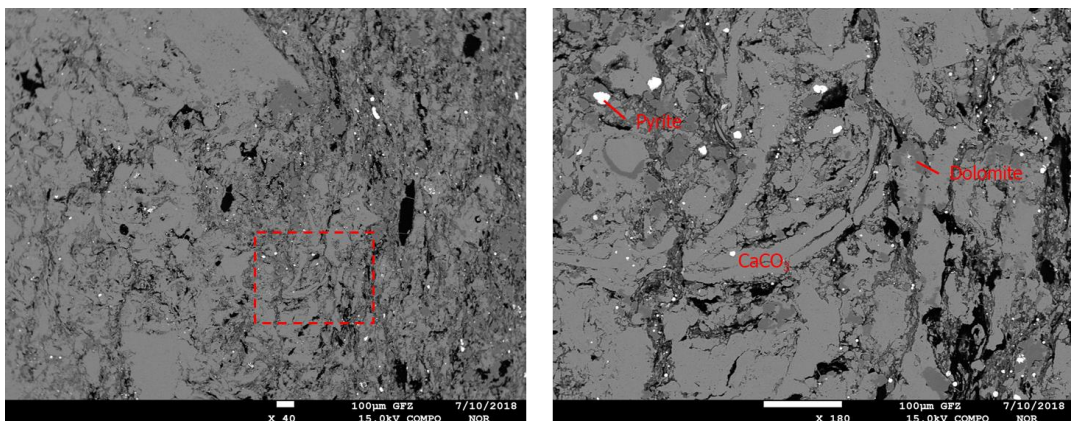


Figure 4.4 Electron microprobe image of the CKO6-AA-01-01-12s showing shells and shell fragments.

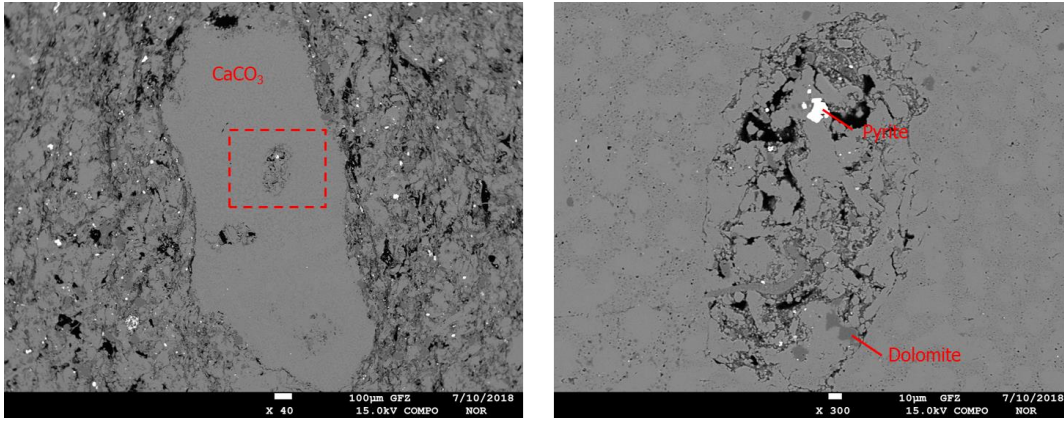


Figure 4.5 Electron microprobe image of the CK06-AA-01-01-12s showing a bioclast with intraparticle porosity.

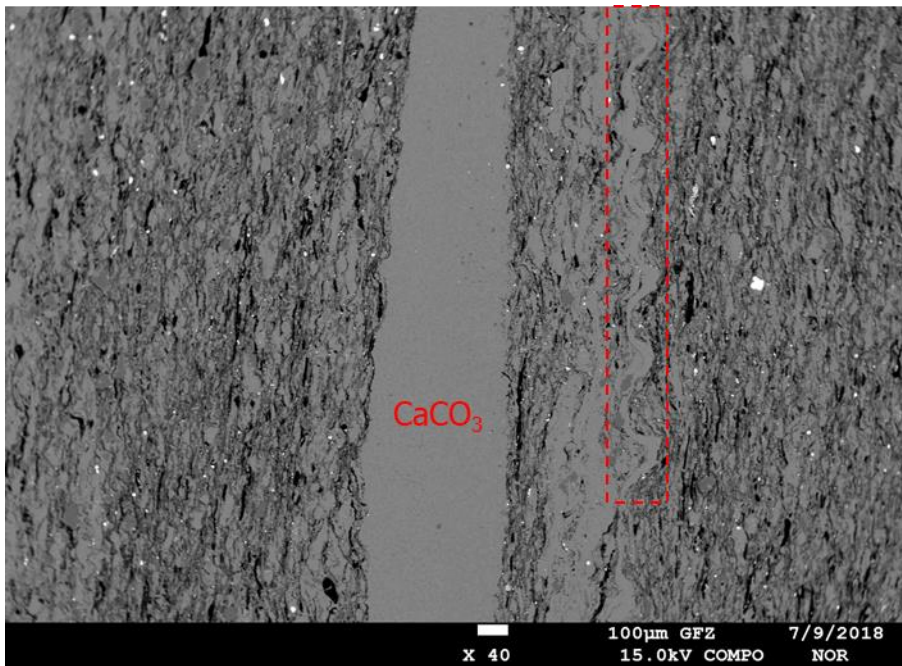


Figure 4.6: Electron microprobe image of CK06-AA-01-01-12s highlighting a brachiopod. Besides, a large shell fragment and a relatively high degree of dolomite content.

5

Results

5.1. Tensile strength

Nine different rock samples were loaded at three different orientations relative to their bedding (Figure 5.1). The maximum tensile strength is recorded for all samples except the CKO6-AA-01-02-11s sample. This sample showed cracks in different orientations (Figure 5.5) and therefore the failure is interpreted as a non-tensile fracture (Markides and Kourkoulis, 2013). The other samples showed a single vertical tensile fracture as indicated by Figure 5.3 and Figure 5.4. The cores with the axial load parallel to the bedding showed a tensile fracture along a bedding plane (Figure 5.3). The other orientations showed an arbitrary vertical fracture with small fractures along the bedding (Figure 5.4).

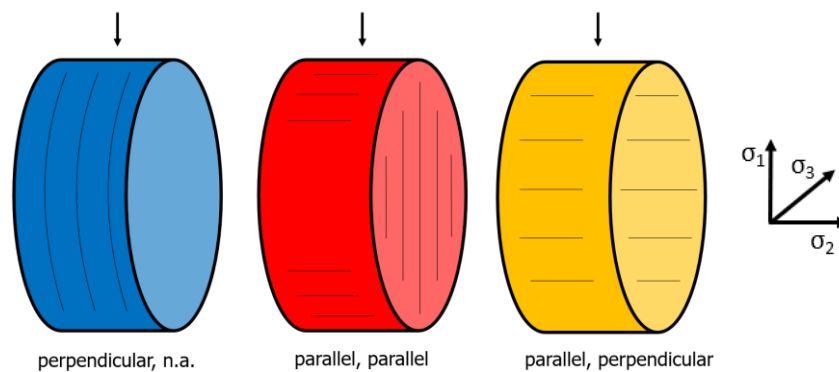


Figure 5.1: Schematic overview of the bedding and stress orientation during the Brazilian strength test. The first part indicates the bedding orientation, the second part the load direction with respect to the bedding plane.

The tensile strength results show a clear difference between the different sample orientations (Table 4; Figure 5.2). The discs with their bedding orientation parallel to the vertical load show a tensile strength of 4.1 MPa. In the case of the other orientations, the load is perpendicular to the bedding. These samples show a tensile strength of 7.6 and 6.5 MPa, which is 2 times larger compared to the samples with the load parallel to the bedding.

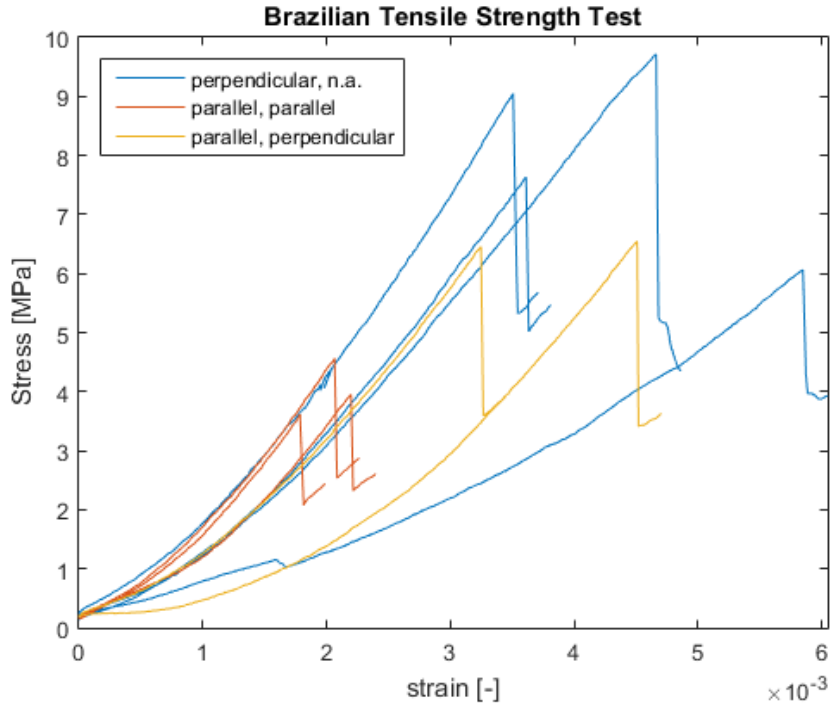


Figure 5.2: Stress-strain curves of the Brazilian disc test of the different oriented samples.

Sample code	Pmax [kN]	Pmin [kN]	σ_t [MPa]	K_{IC} [MN/m ^{1.5}]	bedding orientation w.r.t. tensile stress
CK06-AA-01-02-07s	15,9	10,4	8,3	1,3	<i>n.a.</i>
CK06-AA-01-02-03s	17,2	10,1	8,3	1,1	<i>n.a.</i>
CK06-AA-01-02-12s	12,8	8,2	6,1	0,9	<i>n.a.</i>
CK06-AA-01-02-11s	22,1*	<i>n.a.</i>	<i>n.a.</i>	<i>n.a.</i>	<i>n.a.</i>
<i>Average + Standard deviation</i>	<i>15,3 1,85</i>	<i>9,6 1,00</i>	<i>7,6 1,06</i>	<i>1,1 0,15</i>	
CK06-AA-01-03-09p	8,5	5,0	3,9	0,5	parallel
CK06-AA-01-03-11p	9,9	5,5	4,6	0,6	parallel
CK06-AA-01-03-08p	7,7	4,4	3,6	0,5	parallel
<i>Average + Standard deviation</i>	<i>8,7 0,91</i>	<i>5,0 0,45</i>	<i>4,1 0,39</i>	<i>0,5 0,04</i>	
CK06-AA-01-03-12p	14,0	7,3	6,5	0,8	perpendicular
CK06-AA-01-03-10p	14,5	8,1	6,5	0,8	perpendicular
<i>Average + Standard deviation</i>	<i>14,3 0,23</i>	<i>7,7 0,38</i>	<i>6,5 0,05</i>	<i>0,8 0,02</i>	

Table 4: Results from the Brazilian tensile strength test. *not included in the average and standard deviation.

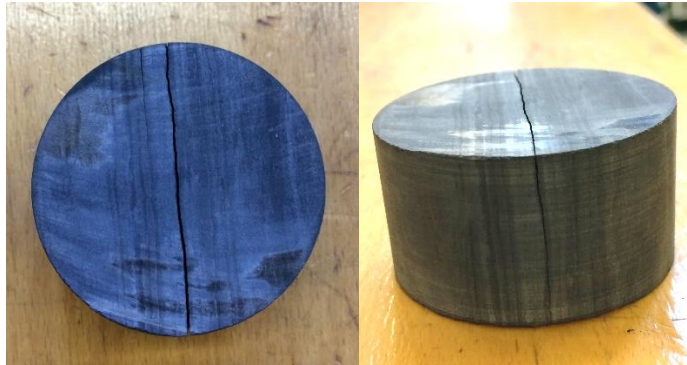


Figure 5.3: CK06-AA-01-03-09p after Brazilian test showing a mode I fracture along the bedding

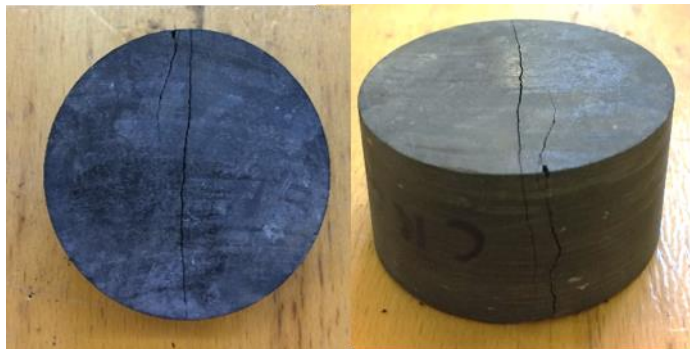


Figure 5.4: CK06-AA-01-02-03s after Brazilian test showing an arbitrary vertical tensile fracture.



Figure 5.5: CK06-AA-01-02-11s after Brazilian testing showing non tensile failure

5.2. Mode I Fracture toughness

The fracture toughness of the tensile fractures created by the Brazilian disc test is determined based on the relation of Guo et al (1993). In the case the load is parallel to the bedding, the fracture toughness is $\sim 0.5 \text{ MN/m}^{1.5}$, which is significantly lower compared to the samples loaded perpendicular to the bedding (Table 4). These samples show an average fracture toughness of $\sim 1.1 \text{ MN/m}^{1.5}$ and $\sim 0.8 \text{ MN/m}^{1.5}$. The results of fracture toughness values from this investigation are comparable to the fracture toughness values obtained by Bakker (Appendix C).

5.3. Mode II Fracture toughness

To obtain the mode II fracture toughness, four different PTS tests are performed. Within three PTS experiments a horizontal aligned fracture initiated at the top of the bottom notch during the axial loading stage. Since no shear fracture initiated from the bottom notch to the upper notch, the mode II fracture toughness could not be obtained. The results of the successful experiment are divided into two parts: the displacement as a result of the axial loading including the K_{IIC} and the permeability evolution during the experiment (Chapter 5.9.1).

A confining pressure of 40 MPa and a pore pressure of 20 MPa was applied to the CKO6-AA-01-02-02s sample. At a displacement of 0.621 mm it reached its maximum axial load of 133.4 kN (Figure 5.23). Based on the relation of Backers (2012), the mode II fracture toughness of this sample was established at 10.3 MN/m^{1.5}.

5.4. Unconfined Compressive Strength

Four UCS tests are performed, two on the x/y-oriented and two on the z-oriented samples. The x/y oriented samples showed a UCS of 116 MPa and 158 MPa, the z-oriented samples 124 MPa and 152 MPa (Table 5). The stress - strain curves in Figure 5.6 are almost linear for all samples, indicating a fully elastic region until ultimate compressive failure.

Sample code	UCS [MPa]
CKO6-AA-01-03-07p	116
CKO6-AA-01-03-02p	158
CKO6-AA-01-01-06s	124
CKO6-AA-01-01-11s	152
<i>Average + Standard deviation</i>	<i>138 20</i>

Table 5: Unconfined compressive strength results from 4 different samples.

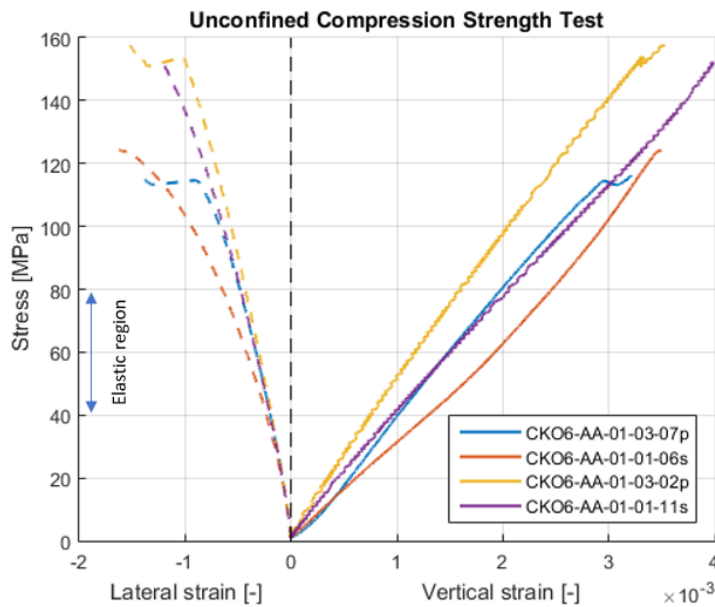


Figure 5.6: Stress strain curve of the UCS test.

x/y-oriented samples

Prior to the ultimate failure of both the CKO6-AA-01-03-07p and CKO6-AA-01-03-02p, a crack was audible and confirmed by the axial and lateral strain (Figure 5.7). Since both cracks initiated just before the maximum strength, these cracks presumably initiated the failure of the sample. Both fractured rocks show a complex fracture structure with the main fractures parallel to the bedding planes. Parallel and close to these fractures smaller fractures and some small conjugates are present.

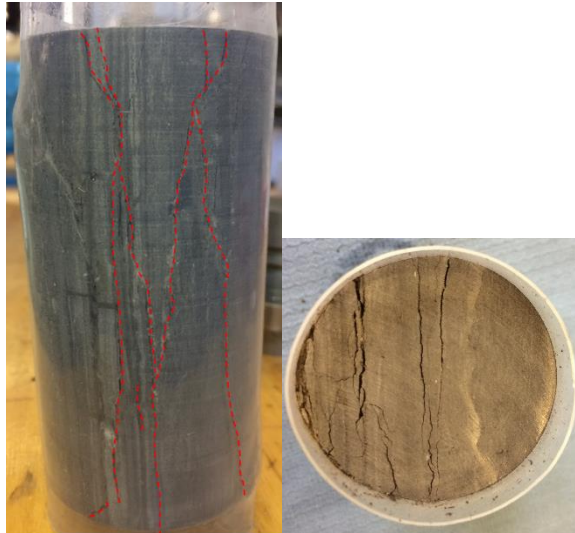


Figure 5.7: CKO6-AA-01-03-07p rock sample after uniaxial compression test.

z-oriented samples

In contrast to the x/y-oriented samples, no pre-failure was recognized during the axial displacement of both z-oriented cores. Again a complex structure of fractures was formed with two main vertical fractures. In the case of the CKO6-AA-01-01-11s one main fracture was vertical and one main vertical fracture shifted along the bedding plane at the center of the sample (Figure 5.8).



Figure 5.8: CKO6-AA-01-01-11s rock sample after uniaxial compression test.

5.5. Triaxial Compressive strength

Triaxial loading was performed with seven samples, at the confining pressures of 20, 30, 40 and 50 MPa. Table 6 shows the compressive strength obtained from the loading tests. During the axial loading, the axial and lateral strain were monitored by the extensometers (Figure 5.9 and Figure 5.10). In addition, the change in pore volume was monitored in order to recognize further closure or opening of the pore space.

Sample code	Confining Pressure [MPa]	σ_{max} [MPa]
CKO6-AA-01-03-06p	20	197
CKO6-AA-01-03-01p	30	229
CKO6-AA-01-03-05p	40	306
CKO6-AA-01-02-01s	20	205
CKO6-AA-01-02-08s	30	203
CKO6-AA-01-02-10s	40	228
CKO6-AA-01-02-05s	50	241

Table 6: Overview of the triaxial test data including the confining pressure.

The x/y-oriented cores showed a clear increase in compressive strength as the confining pressure increases (Figure 5.9). At the confining pressure of 20 MPa, the rock sample showed an UCS of 197 MPa which is significantly lower than the UCS of 306 MPa at 40 MPa. The z-oriented cores on the other hand showed no significant difference as a function of the confining pressure (Figure 5.10). Their UCS is slightly increasing at a higher confining pressure, however, based on the differential pressure there was almost no increase in compressive strength.

The samples with a confining pressure of 20 MPa show a different fracture structure in comparison to the tests performed at higher confining pressures (Appendix B). The CKO6-AA-01-03-06p has 3 main diagonal fractures and the CKO6-AA-01-02-01s one main fracture interrupted by a complex conjugate fracture structure. All samples with a confining pressure of at least 30 MPa showed one main diagonal shear fracture.

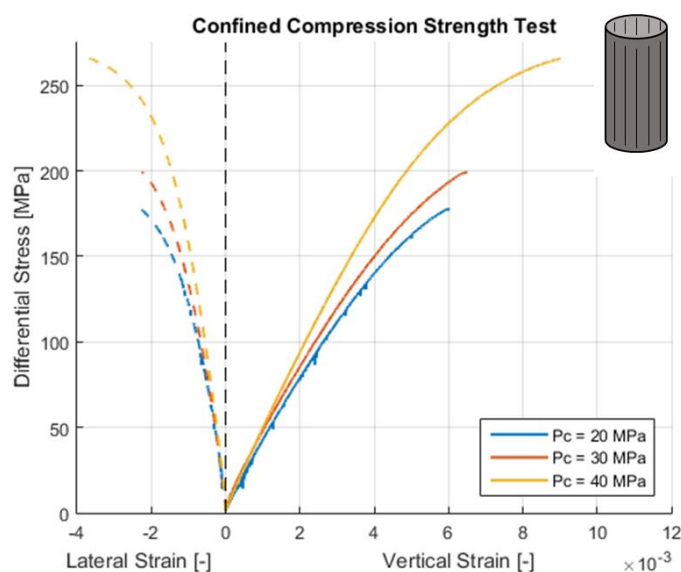


Figure 5.9: Stress-strain curves of the confined compressive strength test of the x/y-oriented cores.

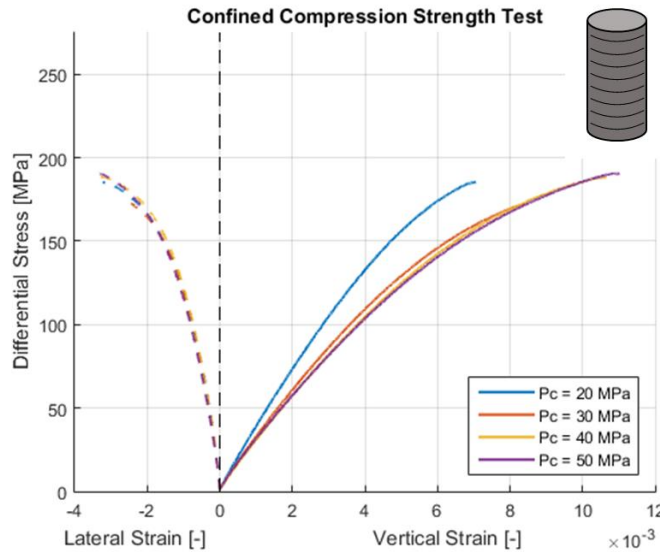


Figure 5.10: Stress-strain curves of the confined compressive strength test of the z oriented cores.

5.6. Failure Criteria

A failure envelope was constructed based on the indirect Brazilian test data, the UCS tests and triaxial compression test. As discussed in appendix D, anisotropy causes a significant strength difference for both the tensile and confined compressive stress tests. Therefore two different failure envelopes were constructed based on one sample orientation (Figure 5.11 and Figure 5.12).

Orientation	Cohesion [MPa]	Friction coefficient [-]	Failure angle [°]
x/y-orientation	46.4	0.38	~ 27
z-orientation	31.6	0.77	~ 27

Table 7: Cohesion and angle of friction based on the UCS and CCS tests specified according to the sample orientation.

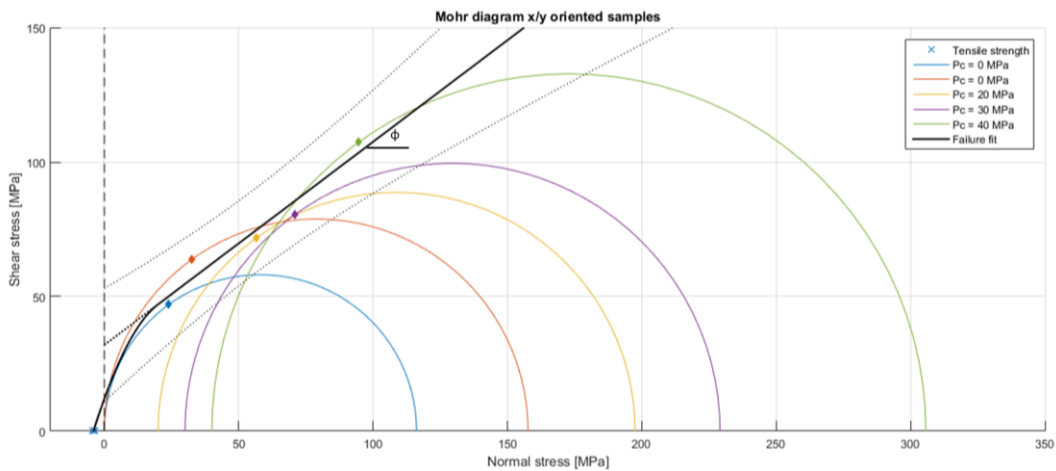


Figure 5.11: Mohr Coulomb failure envelope including Tensile strength, confined compressive strength and unconfined compressive strength of the x/y-oriented samples. 90% confidence intervals show the upper and lower bound of the failure envelope.

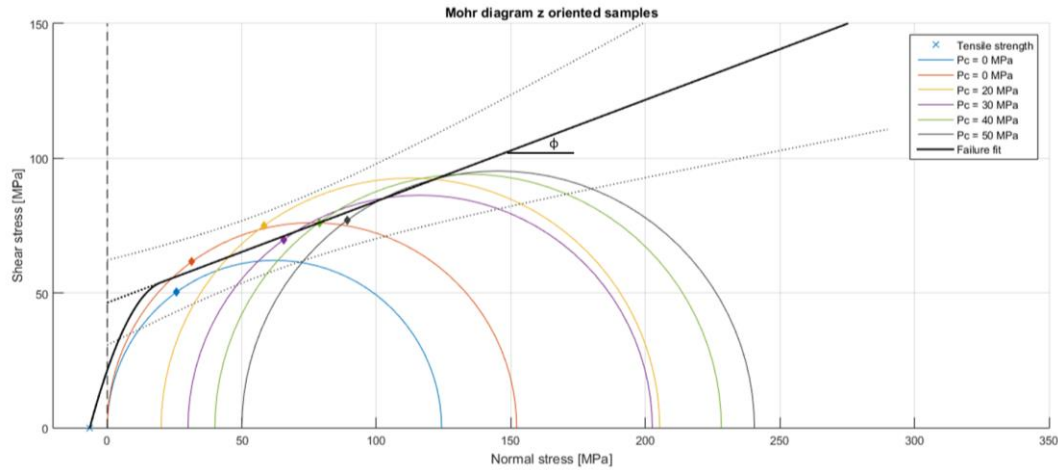


Figure 5.12: Mohr Coulomb failure envelope including Tensile strength, confined compressive strength and unconfined compressive strength of the z-oriented samples. 90% confidence intervals show the upper and lower bound of the failure envelope.

For the construction of the failure envelopes, a failure angle of 27° is assumed based on the measured failure angles of the deformed samples (Appendix B) and a best fit of the failure envelope itself. A difference in the friction coefficient between the different orientations is clearly shown by failure envelopes. The friction coefficient of the parallel samples with 0.38 is significantly lower compared to a friction coefficient of 0.77 of the perpendicular samples.

5.7. Elastic Moduli

Both the Poisson's ratio and Young's modulus are determined within the elastic region of the stress strain curve of both the unconfined and triaxial compressive tests (Table 8). Due to micro-crack closure of pre-existing cracks, the strain shows a non-linear behaviour at vertical stresses below 25% of the failure strength. Plasticity starts to have an effect at vertical stresses of over 75% of the failure strength. The interval between the vertical stress of 40 MPa and 80 MPa is chosen, because the non-linear behaviour of the rock is not affecting the determination of the elastic moduli (Figure 5.6).

Sample code	Confining Pressure [MPa]	Young's modulus [GPa]	Poisson's ratio [-]
CKO6-AA-01-03-07p	0	41,0	0,296
CKO6-AA-01-03-02p	0	46,0	0,280
CKO6-AA-01-03-06p	20	34,8	0,312
CKO6-AA-01-03-01p	30	36,9	0,289
CKO6-AA-01-03-05p	40	44,1	0,281
CKO6-AA-01-01-06s	0	34,2	0,357
CKO6-AA-01-01-11s	0	36,1	0,251
CKO6-AA-01-02-01s	20	32,6	0,305
CKO6-AA-01-02-08s	30	25,2	0,234
CKO6-AA-01-02-10s	40	24,1	0,216
CKO6-AA-01-02-05s	50	23,6	0,230

Table 8: Overview of the Young's modulus and Poisson's ratio obtained from the confined and unconfined compressive strength tests.

The values of the Young's modulus and Poisson's ratio (Table 8) depend on the sample orientation. The Young's modulus of the x/y-oriented samples is higher in comparison with

the z oriented samples. In addition, the Young's modulus of the z-oriented samples decreases at higher confining pressures. Within the x/y-oriented samples no clear trend can be recognized. The Poisson ratio shows lower values for the x/y oriented samples at higher confining pressures. The z-oriented samples do not show a clear dependency of the confining pressure.

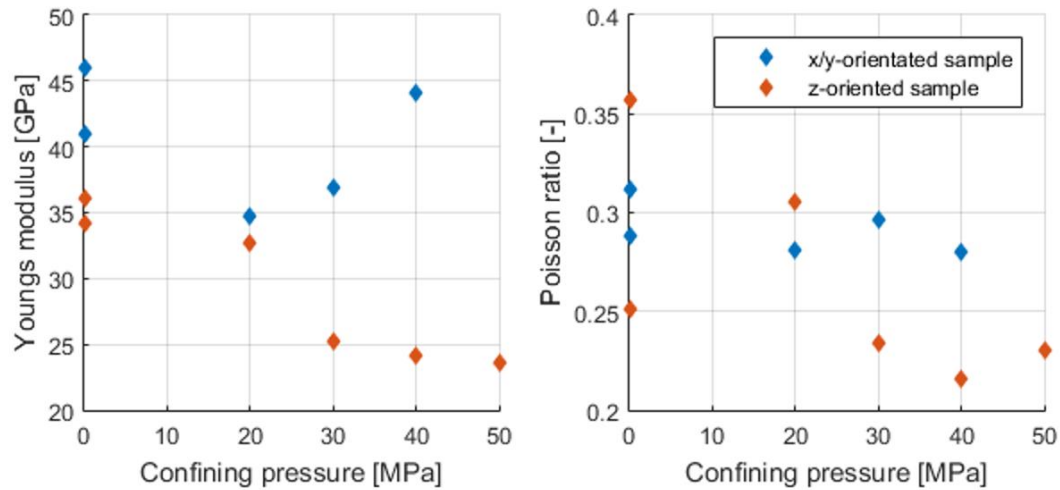


Figure 5.13: The Young's modulus and the Poisson ratio as function of the confining pressure.

Elastic moduli are also determined by ultrasonic wave velocities. Two z-oriented samples are used to establish the first arrival of both p- and s-waves, parallel and perpendicular to the bedding (Appendix F). Based on the eqs. (12), (13) & (14) the Young's modulus and Poisson's ratio of the investigated samples are derived. The two different samples show nearly similar elastic moduli depending on their orientation. The Young's modulus parallel to the bedding is ~ 57 GPa and therefore clearly larger than the Young's modulus perpendicular to the bedding (~ 46 GPa). The Poisson's ratio shows a similar relation: a larger Poisson's ratio is obtained from the x/y-direction (~ 0.28) in comparison to the z-direction (0.19 and 0.23).

Sample code	Orientation	Young's modulus [GPa]	Poisson's ratio [-]
CKO6-AA-01-01-10s	z	45,4	0,192
CKO6-AA-01-01-10s	x/y	56,3	0,278
CKO6-AA-01-02-04s	z	46,6	0,234
CKO6-AA-01-02-04s	x/y	56,7	0,272

Figure 5.14: Poisson's ratio and Young's modulus derived from ultrasonic measurements.

5.8. Porosity

The porosity was determined by three different methods: Mercury Intrusion Porosimetry, Helium pycnometry and by the hydrostatic weighing method. All methods show porosity values between 0.21 and 1.00%, with a maximal uncertainty of $\pm 0.88\%$ (Table 9). This uncertainty is mainly affected by measuring the sample dimensions (Helium pycnometer and dry/wet method). The MIP method is not dependent on the sample dimensions and is therefore the most accurate method, as indicated by the uncertainty range.

Sample code	Porosity [%]	Uncertainty [%]
Helium Pycnometer		
CKO6-AA-01-03-18p	0.82	±0.85
CKO6-AA-01-03-13p	0.21	±0.86
CKO6-AA-01-03-15p	1.00	±0.88
Hydrostatic Weighing		
CKO6-AA-01-01-10s	0.82	±0.36
CKO6-AA-01-02-05s	0.87	±0.36
Mercury Intrusion Porosimetry*		
CKO6-AA-MIP1	0.30	±0.3
CKO6-AA-MIP2	0.21	±0.3

Table 9: Overview of porosity values determined by the different methods. *error range from Kuila (2013).

5.8.1. Porosity Change

During the hydrostatic and axial loading of the sample, pore fluid is squeezed out of the sample. The outflow pore fluid and therefore the pore volume reduction is monitored by maintaining a constant pressure of 0.1 MPa at both the inlet and outlet (Figure 5.15).

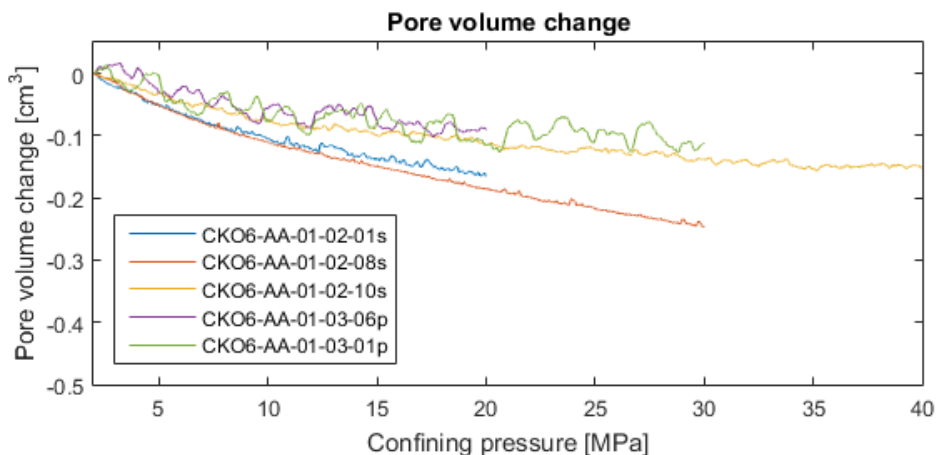


Figure 5.15: The pore volume change during the confining pressure ramp.

All samples show an exponential decrease of the pore volume. At a confining pressure of 20 MPa, the average pore volume change is 0.14 cm³ with a maximum at 0.18 cm³ and the minimum at 0.11 cm³. The CKO6-AA-01-03-01p and CKO6-AA-01-03-06p samples show a more volatile behaviour, which can be explained by the temperature sensitivity of hydraulic pumps: the larger the amount of liquid in the cylinder, the larger the error due to temperature variations within the laboratory. Based on the volatility of the curve, the error is determined at ± 0.03 cm³ for the parallel samples and ± 0.01 cm³ for the perpendicular samples. At a confining pressure of 20 MPa the pore volume change corresponds to a porosity decrease between 0.04% and 0.097%. Based on the obtained average porosity of 0.8% of the intact rock, the relative porosity change is between 5% - 12%.

During the vertical loading a pore pressure of 0.1 MPa was applied to the sample. The pore volume change was monitored by setting both top and bottom at 0.1 MPa pore pressure. A

decrease of pore volume is recognized as an indication of micro crack closure in the beginning of the axial loading. Figure 5.16 shows the pore volume change during the axial loading. The pore volume change after ultimate failure is highlighted. The CKO6-AA-01-03-06p and the CKO6-AA-01-03-01p are dominated by presumably temperature changes. Nevertheless, a pore volume decrease prior to failure within all samples can be identified, varying from 0.01 cm³ to 0.07 cm³. Due to the fluctuation of the volume, the opening of microcracks or dilation of the sample before failure cannot be established based on the squeezed out pore volume data. Except the CKO6-AA-01-03-01p sample, all samples showed an increase of pore volume after ultimate failure. Since all samples show at least one main fracture intersecting both the top and bottom of the sample, the pore volume increase can be explained by to the opening of the shear fracture (Appendix B).

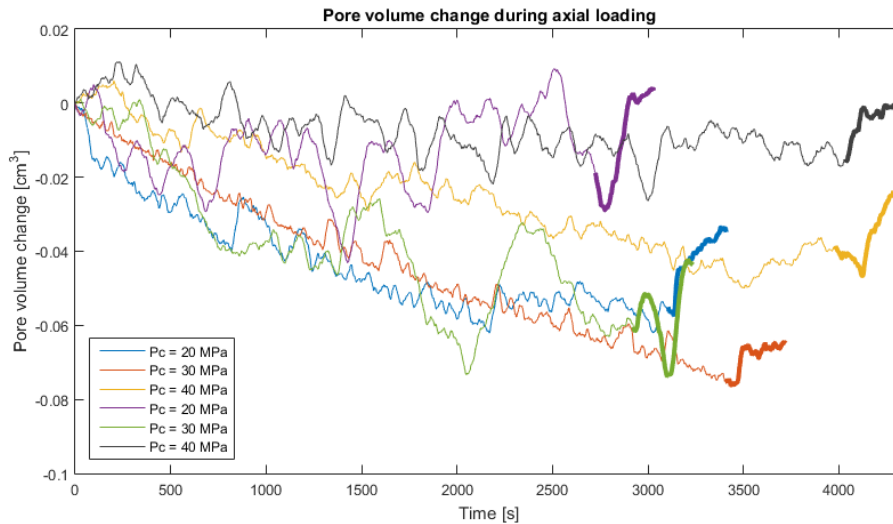


Figure 5.16: Squeezed out pore volume during confined compression test. The highlighted part (bold) shows the pore volume change after ultimate failure. Only CKO6-AA-01-03-01p (green) sample shows no clear increase of pore volume after sample failure.

5.8.2. Bulk Volume Change

The compressive force applied by the confining pressure causes a compaction of the cylinder in all directions. The circular and axial extensometers are used to determine the total compaction during the ramp of the confinement (Figure 5.17).

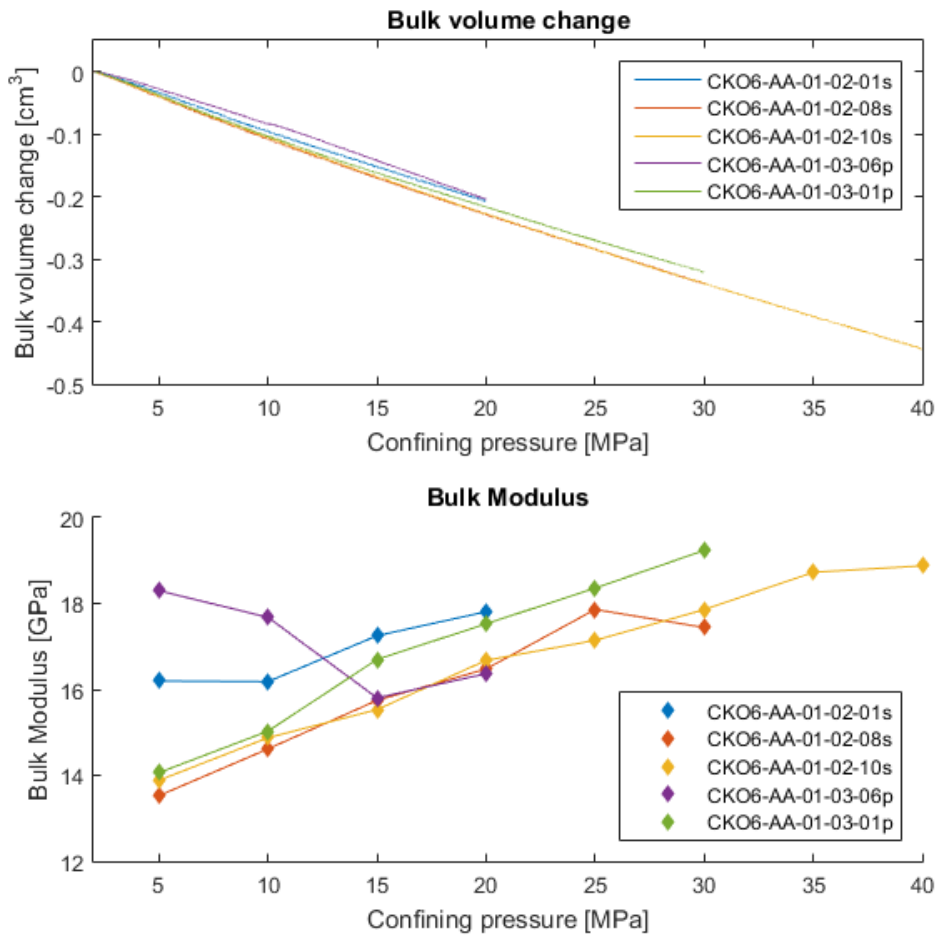


Figure 5.17: Bulk volume change and Bulk Modulus evolution as a function of the confinement pressure.

The change in bulk volume of all the tested samples show a linear and almost equal trend resulting in a slightly increasing Bulk modulus (Figure 5.17).

5.8.3. Biot's Coefficient

The Biot's coefficient represents the ratio between the volume of water squeezed out of a rock to the total volume change due to deformation. The Biot's coefficient is obtained by the one-step testing method (Frankquet and Abbas, 1999). Figure 5.18 shows the Biot's coefficient of five different samples as a function of effective pressure. The Biot's coefficient shows an exponential decay for all samples. The CKO6-AA-01-03-01p and the CKO6-AA-01-03-06p samples show a relative large variation due to the temperature changes. Remarkably, the Biot's coefficient shows a value above one, indicating a larger pore volume change than bulk volume change. This is not possible, and therefore this can be explained by a jacket effect: during increasing confining pressure the jacket deforms into the pores. A change in fluid volume will be monitored by the pumps, however the circular extensometers remain unchanged (Blöcher, 2014).

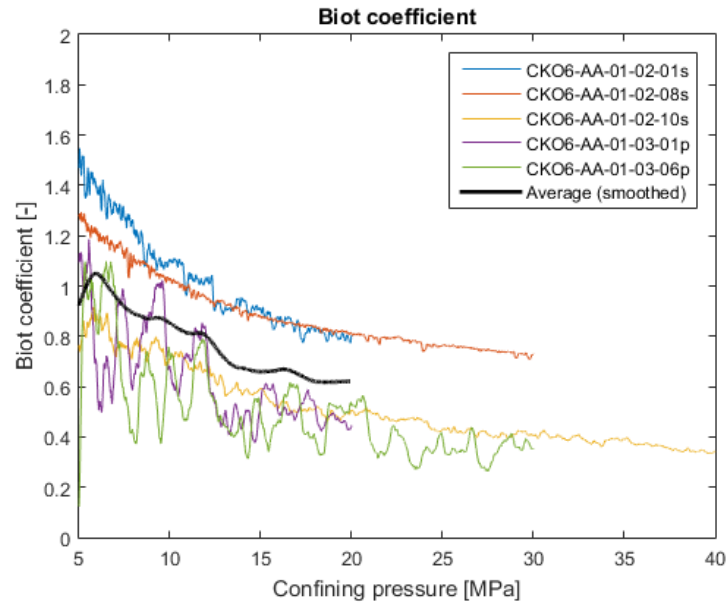


Figure 5.18: Biot's coefficient determined from the one-step testing method (Frankquet and Abbas, 1999).

5.8.4. Pore Size Distribution

Two MIP experiments were performed to determine the porosity and pore size distribution. Two half cylindrical rock fragments are evaluated in terms of total mercury intrusion volume as a function of pressure. Figure 5.19 shows the rough data of the experiment. Both curves show an intrusion of $\sim 0.4 \text{ mm}^3/\text{g}$ at around 0.1 bar. Mercury started to penetrate the pores of the CKO6-AA-MIP2 sample between 60 and 200 bar. Within the CKO6-AA-MIP1 the mercury intrusion started at around 200 bar, showing an exponential increase until a pressure of 2000 bar. Using the relation of Washburn (1921), the pore diameter distribution is obtained (Figure 5.19). The CKO6-AA-MIP1 shows a main pore diameter in the range of $0.01 - 0.05 \mu\text{m}$, for the CKO6-AA-MIP2 a diameter of between 0.05 and $0.3 \mu\text{m}$ is found.

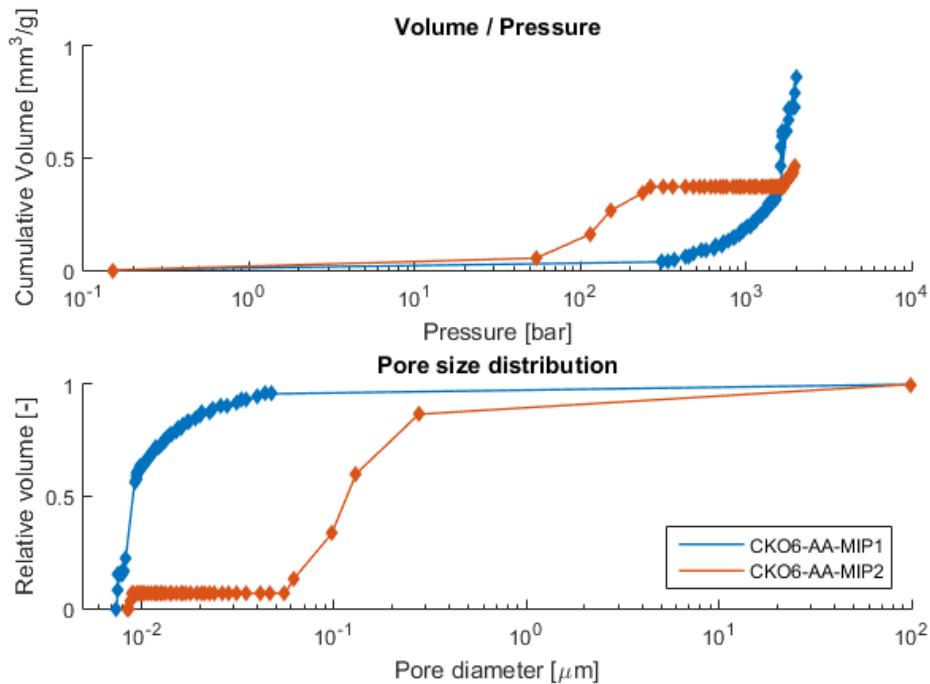


Figure 5.19: Pore size geometry determined by the Mercury Intrusion Porosimetry.

5.9. Permeability

The permeability was determined by three different methods. Figure 5.20 shows the results of the permeability values obtained from the steady state flow in the triaxial cell. A steady state fluid flow is applied by the Quizix pumps to determine the matrix permeability at a confining pressure of 2 MPa. By maintaining a constant pressure at the outlet, the flow rate is set in the way the minimum pressure difference was 0.02 MPa. In order to prove Darcy's law, different flow rates are used to define the rock permeability. The permeability derived from this experiment ranges from 3 to 154 μD . Figure 5.20 shows a clear distinction between the sample orientation and the permeability. In case the flow is perpendicular to the bedding, the permeability ranges from 3 to 24 μD . In case the flow is parallel to the bedding the permeability ranges from 47 to 154 μD .

For the CKO6-AA-01-03-05p and the CKO6-AA-01-05s samples, the permeability was measured while the confining pressure is slowly increased at a constant flowrate. At around 12 MPa a differential pressure between top and bottom exceeded the limit of the differential pressure sensor. After the differential pressure was reached, the flow rate was pressure controlled and the aim was to obtain the permeability based on the volume change. Although there is a pressure difference of 0.9 MPa no steady flow could be observed.

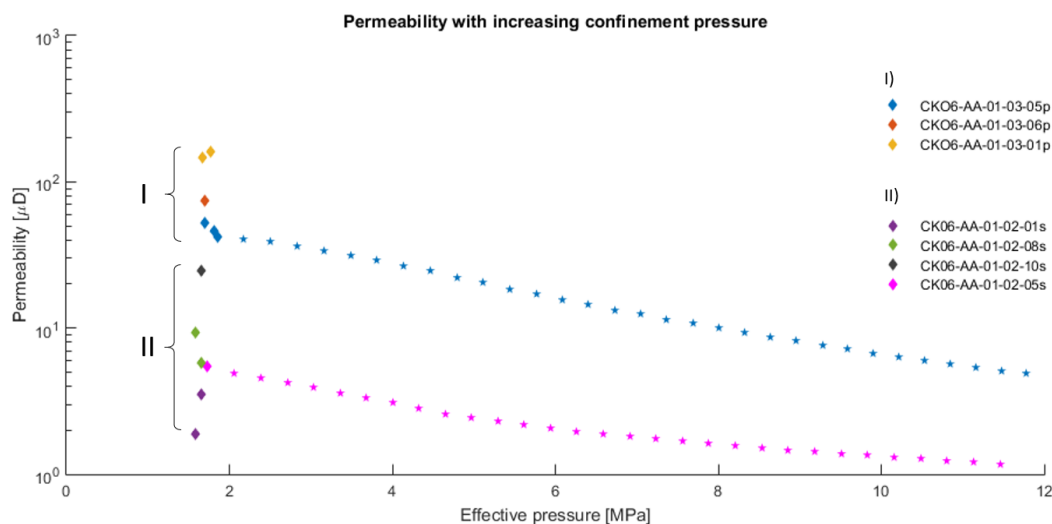


Figure 5.20: Permeability of the different rock samples at a constant confining pressure of 2 MPa. Within some experiments different flow rates are used which resulted in multiple values. The values are grouped by orientations. Two samples show the permeability as a function of effective pressure.

At a confining pressure of 40 MPa a flowrate controlled test was performed for the CKO6-AA-01-03-06p sample to determine the permeability. Since no stable inlet pressure could be established at a flow rate of 0.0005 ml/mm, the permeability is below the limits of the system i.e., lower than 1 μD . It is assumed the permeabilities of all samples are below the lower limit of 1 μD at a confining pressure of 40 MPa.

Sample code	Confining Pressure [MPa]	Permeability ($P_c \sim 2$ MPa) [μ D]
CKO6-AA-01-03-06p	20	74
CKO6-AA-01-03-01p	30	154
CKO6-AA-01-03-05p	40	47
<i>Average + Standard deviation</i>		<i>92 56</i>
CKO6-AA-01-02-01s	20	3
CKO6-AA-01-02-08s	30	8
CKO6-AA-01-02-10s	40	25
CKO6-AA-01-02-05s	50	5
<i>Average + Standard deviation</i>		<i>10 10</i>

Table 10: Permeabilities tested within the triaxial system at a confining pressure of 2 MPa

Gas permeameter

Two rock samples were investigated at four different steady state flow rates. A flow rate was kept constant for around 30 minutes in order to ensure a stable flow (Figure 5.21). The confining pressure is kept constant at 8 MPa for the duration of the entire experiment. Using Darcy's law and the Klinkenberg correction a fluid permeability of 0.31 μ D and 0.17 μ D is obtained (Figure 5.22). The CKO6-AA-01-03-17p shows the expected increasing gas permeability as a function of $2/(P_{in}+P_{out})$, resulting in the 0.17 μ D fluid permeability. On the other hand the CKO6-AA-01-03-16p shows almost no increase in permeability as a function of $2/(P_{in}+P_{out})$.

In addition, two pressure pulse experiments were performed to determine the permeability. Since the P_1 and P_2 showed an erroneous value based on the V_1 and V_2 ratio, no permeability could be obtained from this experimental setup. Presumably, temperature changes within the duration (~ 8 hrs) of the experiment affected the pressure response.

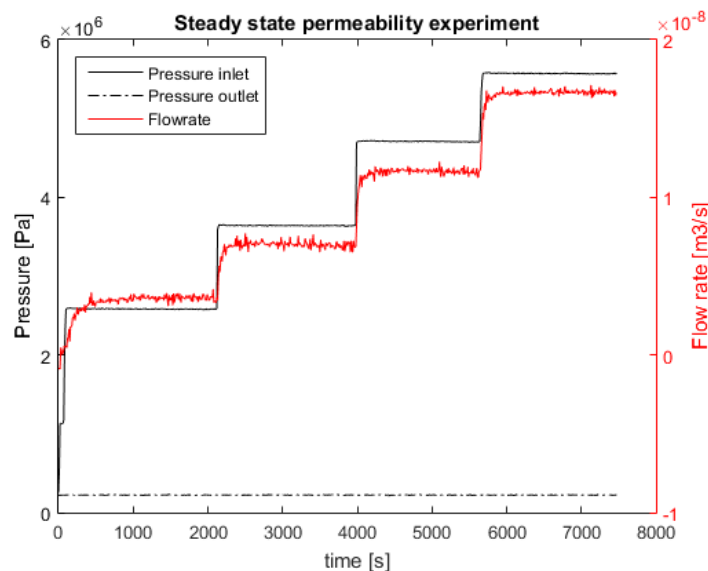


Figure 5.21: Permeability measurements at four different pressure levels.

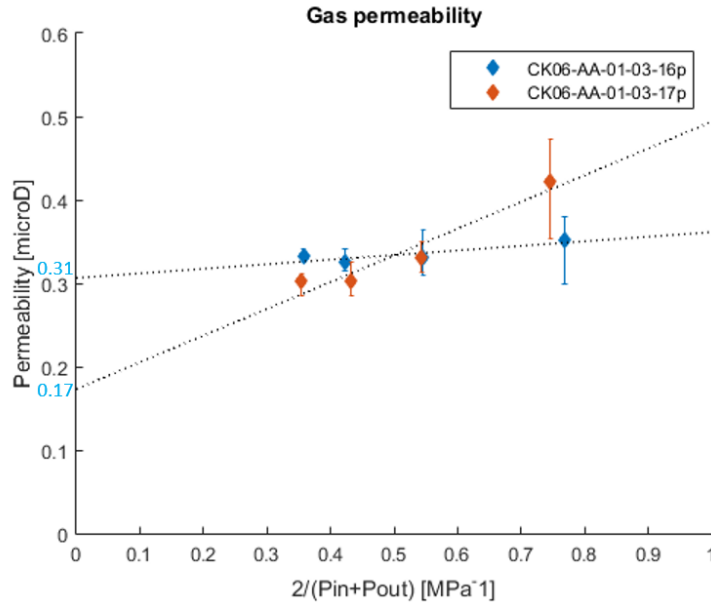


Figure 5.22: Permeability as a function of $2/(P_{in}+P_{out})$. The interception of the dotted line and the y-axis corresponds to the gas corrected permeability.

5.9.1. Punch-Through Shear Permeability

Besides the Mode II fracture toughness, the fracture permeability of a shear fracture was derived from the PTS test. Within three out of the four tested samples, the break-off of the lower inner cylinder was the reason no K_{IIC} could be obtained.

The intact rock permeability of the CK06-AA-01-02-02s sample was determined prior to axial loading at a confining pressure of 40 MPa and a pore pressure of 20 MPa. Since hardly any flow through the sample could be obtained at these conditions, the permeability was below the limits of the MTS i.e., below 1 μD . Therefore the sample was put at a fixed pressure difference of 0.5 MPa during the axial loading. At the maximum axial load, a flow through the sample started which resulted in a change in up- and downstream flow (Figure 5.24). Based on a fixed pressure difference of 0.5 MPa, the permeability started to increase as the displacement increased. At a displacement of 0.72 mm, the constant pressure difference was changed into a constant flowrate in order to determine the permeability more accurately. The permeability increased around two orders of magnitude within the first 0.1 mm after the shear fracture was formed. During this stage the change in lateral strain and axial load was relatively large.

From a displacement of 0.75 mm on, the axial load and the lateral strain became more constant, as well as the permeability. The permeability increased around one order of magnitude between a displacement of 0.75 mm and 1.2 mm and approached a constant permeability.

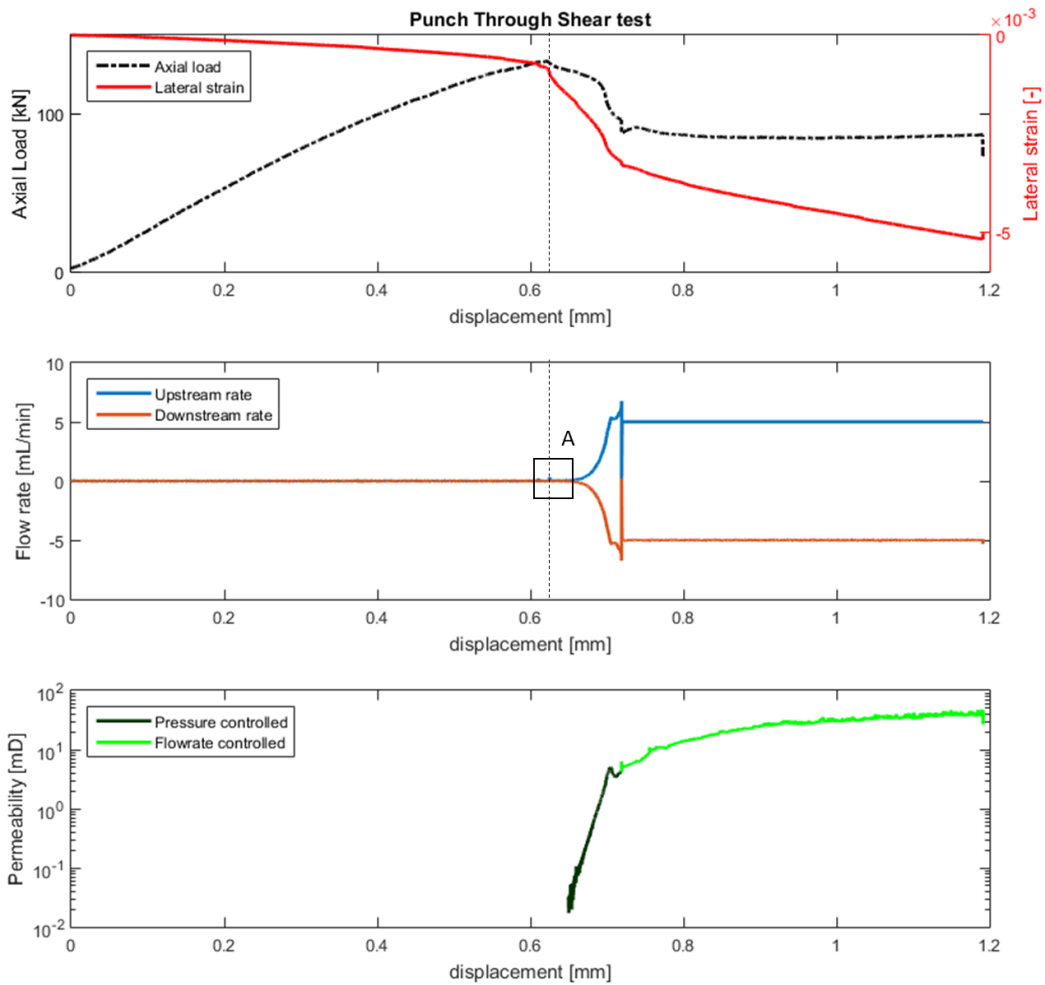


Figure 5.23: Punch Through Shear test of the CKO6-AA-01-02-02s as a function of the displacement rate.

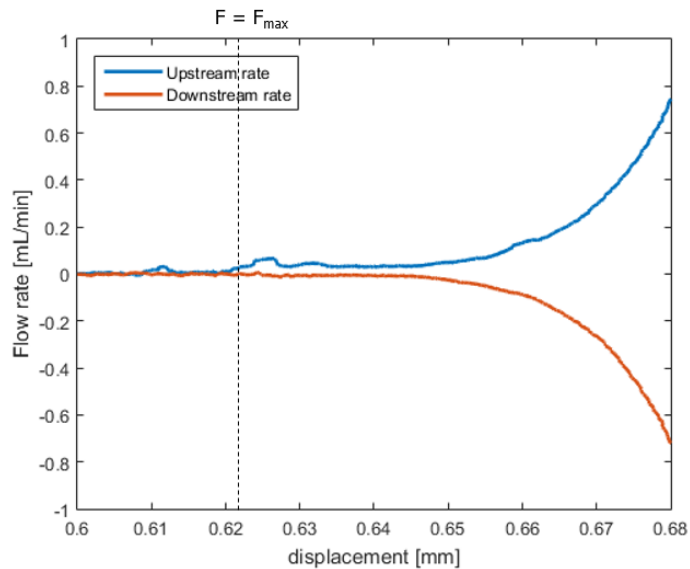


Figure 5.24: Detailed overview of Figure 5.23 showing the start of the inflow.

Until the failure of the sample, the lateral strain measured by the extensometer is a result of the applied axial force causing expansion in the horizontal direction. After failure, the decrease of strain is a result of both the lateral expansion and the opening of the fracture. Assuming the lateral strain before failure is only due to the expansion of the sample, the fracture thickness is zero at the moment failure occurs (3.6.1). Figure 5.25 shows the aperture thickness and fracture permeability as a function of the displacement. The largest

aperture change is in the stage after the failure. At full displacement of 1.2 mm the total fracture aperture is ~ 0.1 mm. The fracture permeability, derived by arithmetic averaging, shows an increasing trend with a final fracture permeability of almost 8 D at 1.2 mm displacement. In addition, the fracture permeability is determined based on the cubic law, resulting in a fracture permeability of 1×10^3 D. At the displacement of 1.2 mm, flow through is performed for around 14 hours, resulting in a relative small drop within both the aperture and permeability (Figure 5.26).

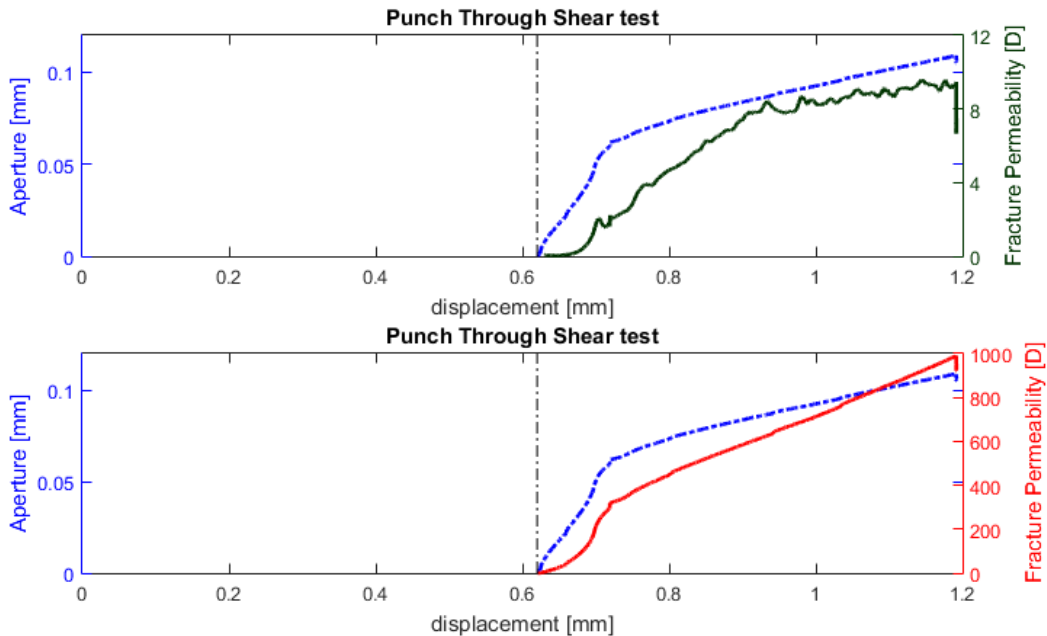


Figure 5.25: Mechanical aperture derived from the lateral strain. Top: the fracture permeability based on the arithmetic averaging. Bottom: the fracture permeability from the cubic law.

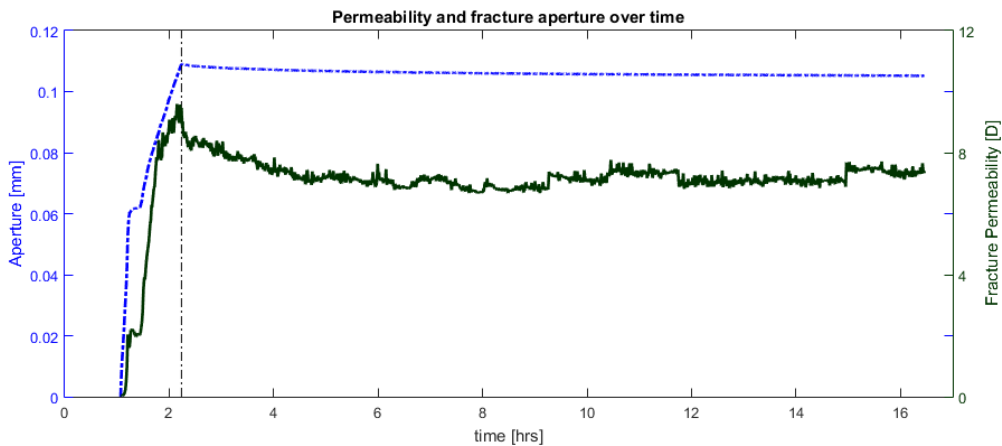


Figure 5.26: Fracture permeability and aperture during displacement (before vertical line) and at a constant displacement of 1.2 mm (after vertical line).

Effective pressure cycling

The effect of varying the effective pressure by changing the pore pressure of the sample is shown in (Figure 5.27). A full pressure cycle consists of 3 different pore pressure levels: 15 MPa, 20 MPa and 25 MPa. The pore pressure is kept constant for 20 minutes to achieve a steady state flow. Figure 5.27 shows clearly the response of the axial load, lateral strain and permeability as a result of pore pressure changes. In the case of a pore pressure of 15 MPa, the permeability decreased due to the closure of the fracture. The closure of the fracture is confirmed by the positive lateral strain. Since the displacement of the axial loading stamp remained fixed during the pore pressure cycling, the axial load increased

because of the vertical expansion of the sample. In case the pore pressure is 25 MPa the permeability, axial load and lateral strain showed the opposite response. After an increase or decrease of the pore pressure, the pore pressure is kept constant for 20 minutes at the intermediate pressure of 20 MPa. Figure 5.27 shows there is a difference in permeability and lateral strain regarding the pressure cycling direction. If the pore pressure is increased from 15 MPa to 25 MPa, the permeability is lower at the intermediate stage of 20 MPa with respect to the permeability within a decreasing pore pressure regime.

All three pressure cycles show similar responses in lateral strain and permeability. However, the axial load shows a decreasing trend over the whole period of pressure cycling. The largest loading drops can be recognized during and after the 25 MPa pore pressure level. The lateral strain shows an almost elastic behavior, since the initial value is similar to the final strain value. The total permeability after 3 cycles increased slightly from 36 mD to 45 mD.

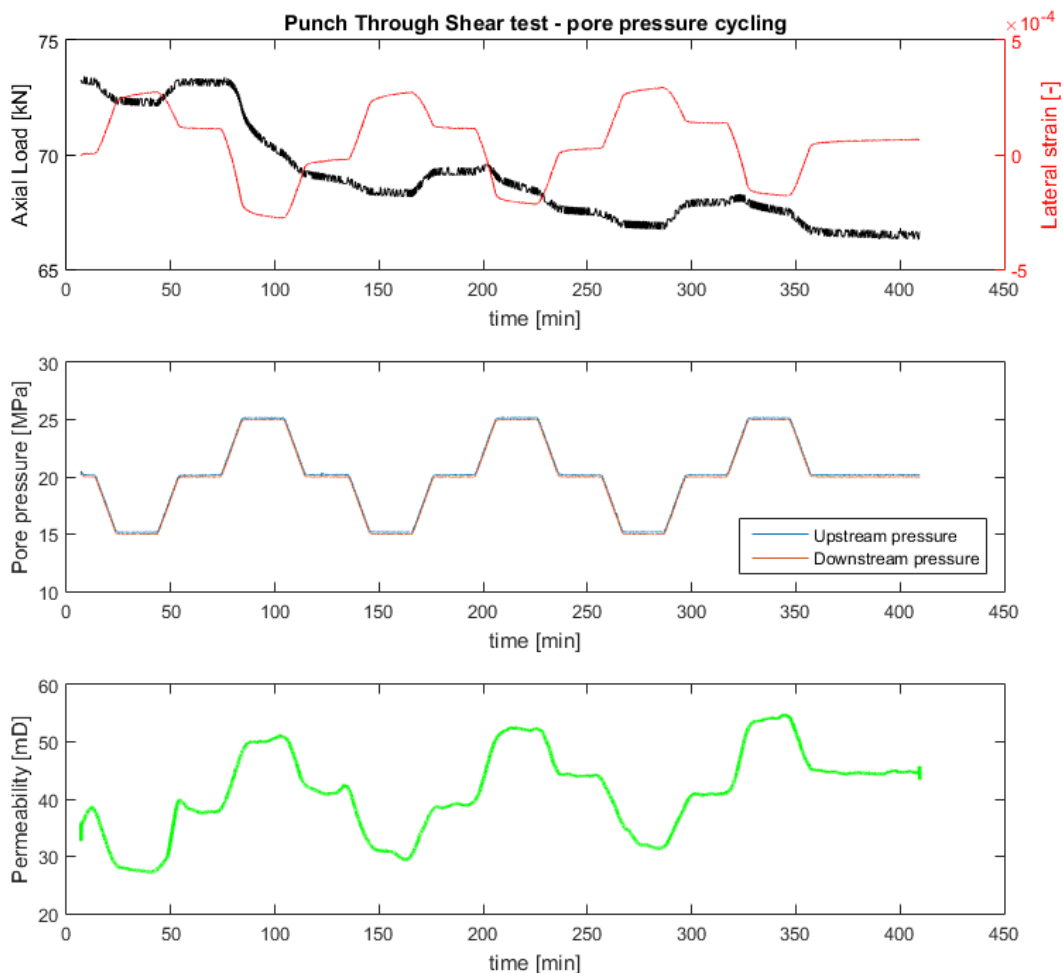


Figure 5.27: the effect of the axial load, lateral strain and permeability as a result of the pore pressure cycles.

The effect of the effective pore pressure on both the permeability and lateral strain shows a linear relationship (Figure 5.28). The aperture only shows a linear relationship if the effective pressure is decreased. In case the effective pressure is increased a more exponential increase of the aperture can be observed (Figure 5.28b). Between the different pressure cycles the variation in permeability is ~ 5 mD at the three effective pressure levels. The variation in mechanical aperture is $\sim 2 \mu\text{m}$.

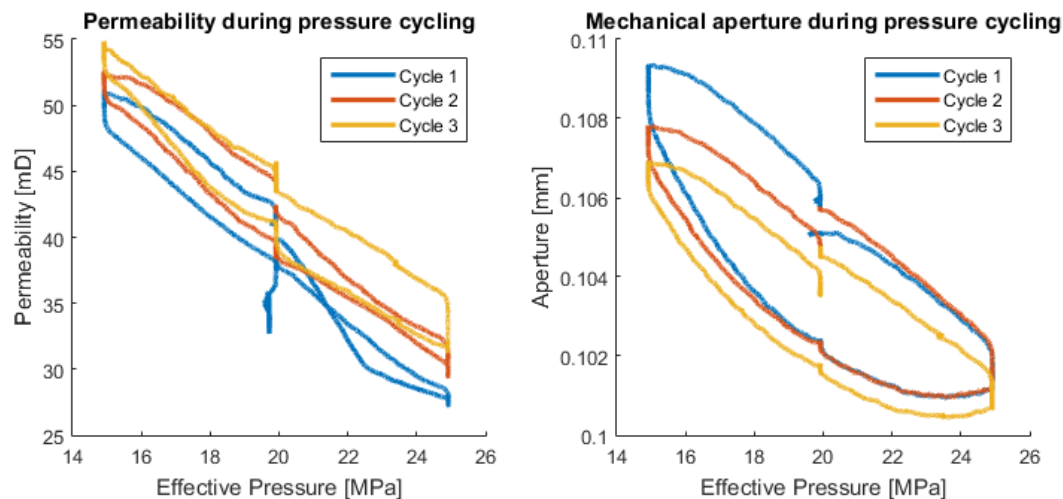


Figure 5.28: permeability and mechanical aperture during the three pore pressure cycles. The second pore pressure cycle is highlighted.

A cross plot of the lateral strain and permeability shows an overall increase of the permeability and decrease of lateral strain. Since it is assumed the permeability and lateral strain are positively correlated, this result is discussed in more detail in 6.5.

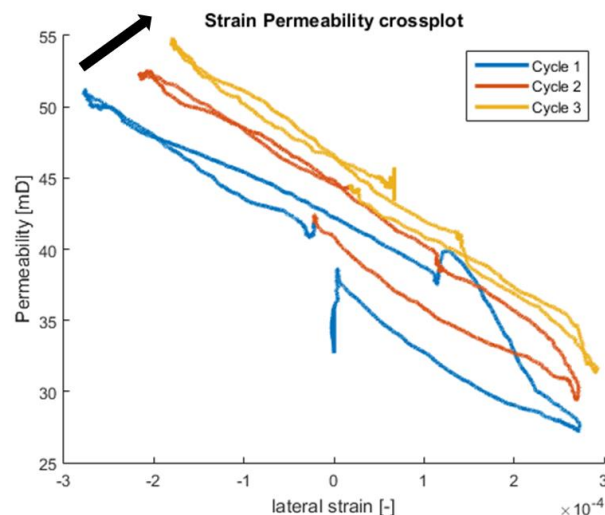


Figure 5.29: Cross plot of the lateral strain and permeability during effective pressure cycling.

After unloading of the axial force and decreasing both the pore and confining pressure the permeability was determined at ~ 2 MPa effective pressure. At these conditions the sample showed a total permeability of 2 D. Since the initial permeability of the sample before deformation was $10 \mu\text{D}$ at an effective pressure of ~ 2 MPa, the total permeability is improved by a factor 2×10^5 . However, during hydrostatic unloading of the sample, radial fractures initiated and created additional fluid paths (Appendix G).

5.9.2. Shear Fracture Permeability

After the failure of the CKO6-AA-01-02-08s and CKO6-AA-01-02-05s samples, displacement of the fracture is continued until a displacement of 0.22 mm and 0.15 mm, respectively, to create an opening of the shear fracture. Afterwards the permeability is measured during a decreasing confining pressure ramp. The sample showed a diagonal shear fracture which intersects both the top and bottom of the sample (Figure 5.30). During the pressure ramp a steady flow rate is used in order to obtain the permeability. The outlet pressure is set at 0.1 MPa.

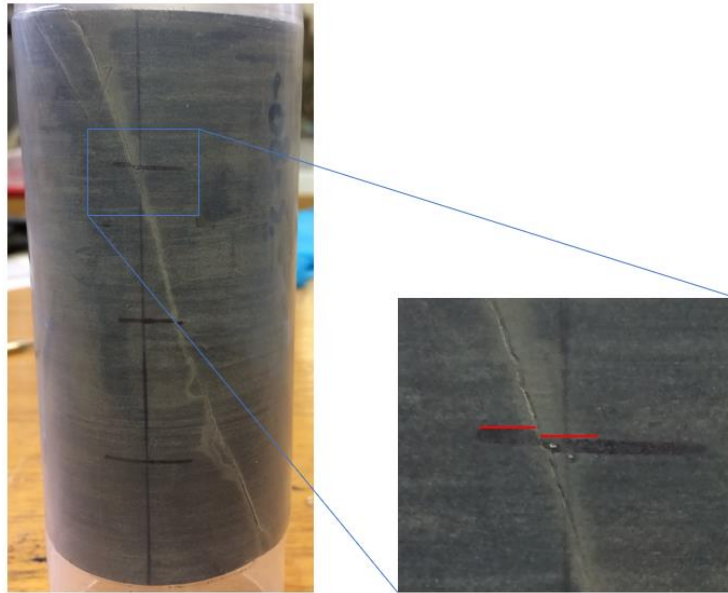


Figure 5.30: Shear fracture of the CKO6-AA-01-02-08s showing the displacement of 0.22 mm.

CKO6-AA-01-02-08s

As a result of the decrease in effective pressure, the flowrate of 0.01 ml/min was not sufficient to obtain the 0.1 MPa at the outlet. Therefore the fluid direction at the end of the sample changed at ~ 7 MPa effective pressure from outward to inward. From there on, steady state flow could not be obtained and the values are not taken into account. At 2 MPa confining pressure another steady flow was applied on the sample, resulting in a permeability of 84 μD (Figure 5.31). The intact rock permeability of this rock at 2 MPa effective pressure was 8 μD resulting in an increase of permeability of one order of magnitude. The aperture increased gradually to a maximum of 0.06 mm.

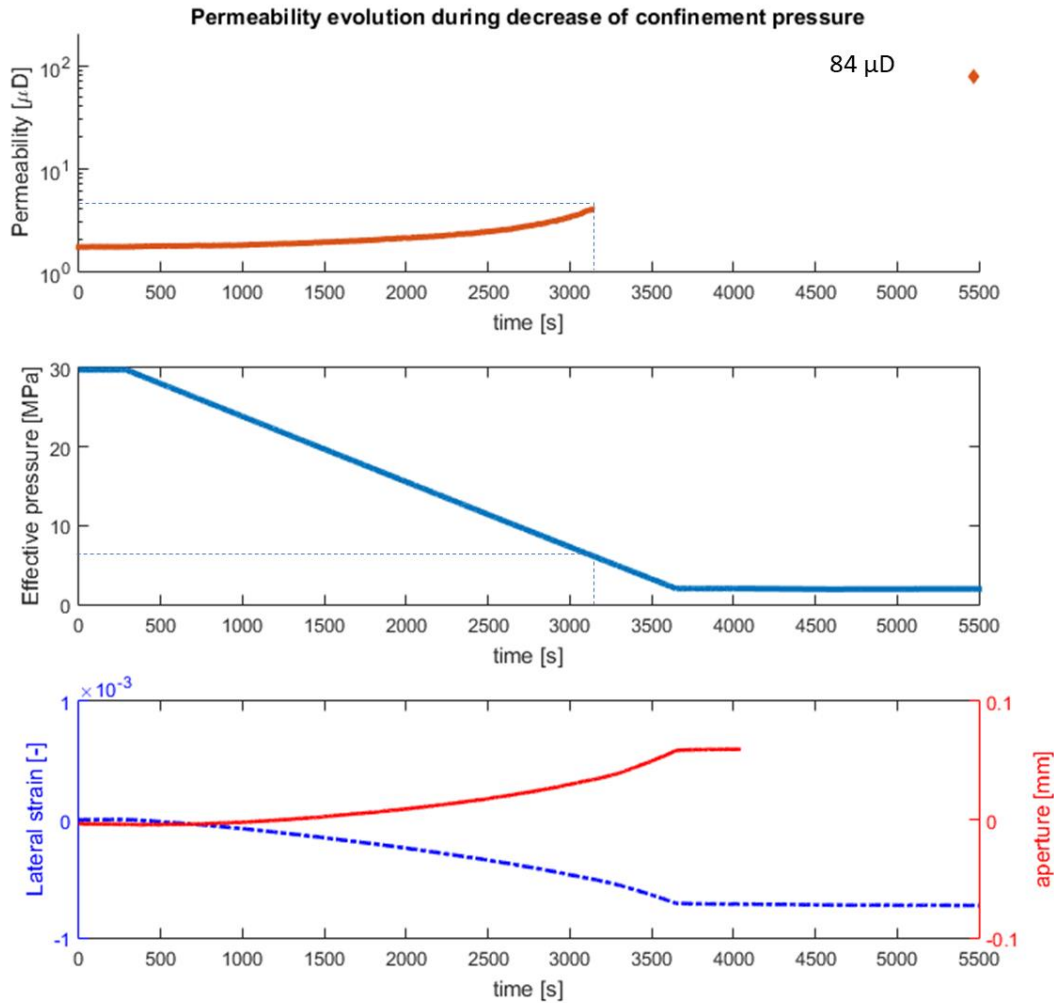


Figure 5.31: Permeability evolution after the shear displacement at different effective pressure of the CK06-AA-01-02-08s

CK06-AA-01-02-05s

A constant flow rate of 0.007 ml/min was set during the confining pressure ramp from 10 MPa to 2 MPa (Figure 5.32). At an effective pressure of 6 MPa the permeability started to increase significantly. Due to the further increase of permeability, the constant flow rate was not sufficient to obtain a steady state flow from a confining pressure of 4 MPa on. A final permeability of 128 μD was obtained at 2 MPa confining pressure. Since the initial permeability of this sample is determined at 5 μD , the permeability increased with a factor 25. A CT image is made to establish the shape of the fracture (Appendix G). It showed an irregular aperture thickness ranging from zero to a maximum of 0.3 mm at ambient conditions.

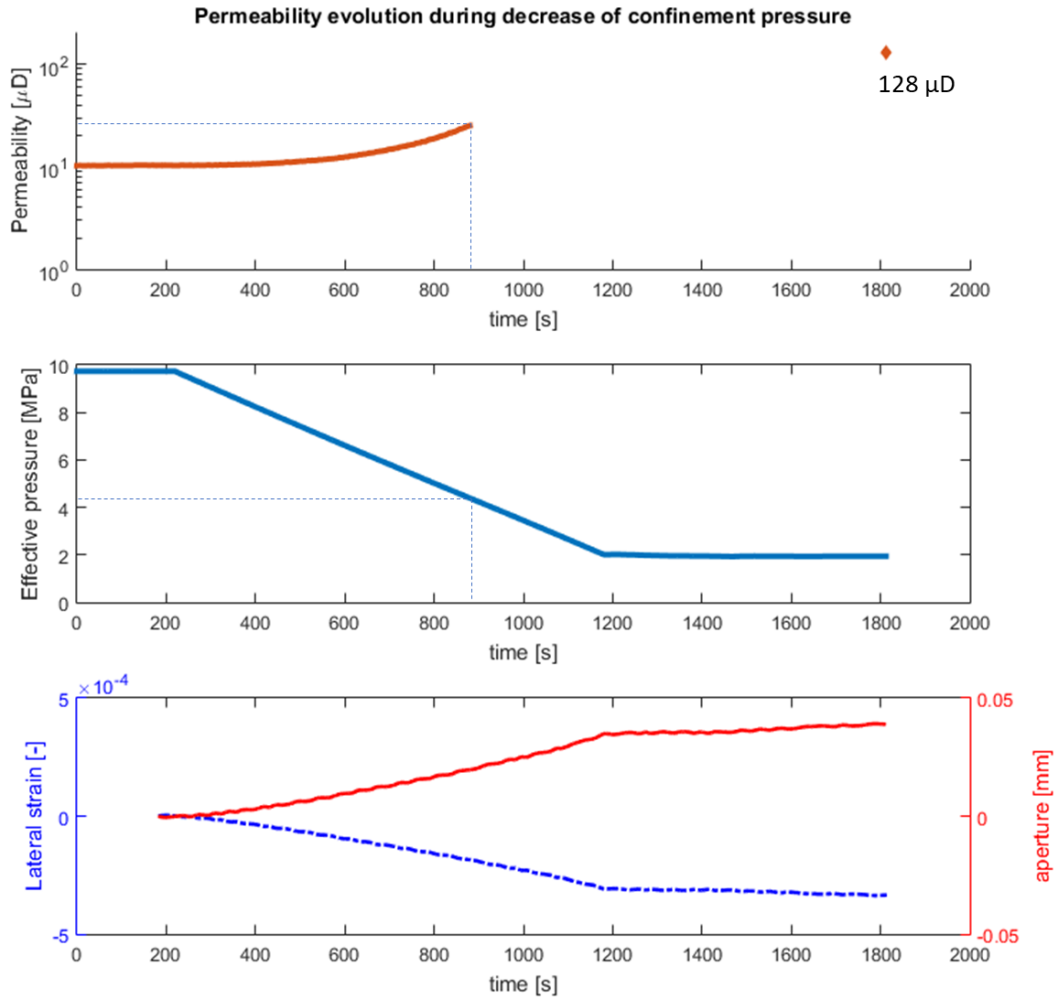


Figure 5.32: Permeability evolution after the shear displacement at different effective pressure of the CKO6-AA-01-02-05s

6

Discussion

6.1. Representativity of the Investigated Samples

The rock samples used for the laboratory experiments may differ from rock masses at the reservoir scale in terms of (hydro)mechanical behaviour. The small scale samples are intact rocks without fractures, whereas rock masses in the subsurface probably contain large scale fracture networks. The samples used in this study are from one block of approximately 1 m³ and only represent the properties of the intact rock matrix. Therefore it covers only a specific part of the Lower Carboniferous limestone formation. The mean and range of the values presented in Chapter 5 can be used as a reference. Additionally, the number of performed tests is different for each experiment, and should be considered within the representativity of the mean and range.

The absence of macroscopic discontinuities indicates that the derived parameters represent either the upper or lower bound. For example, in the laboratory experiments compressive strength is overestimated compared to the reservoir. Although it is not possible to cover varieties on reservoir scale in the laboratory, the Representative Elementary Volume (REV) of the samples covers the irregularities at the grain scale. In order to upscale our data to a representative reservoir scale, a more detailed large scale investigation of the Lower Carboniferous fracture system is required, which incorporates the macroscopic discontinuities.

As discussed in Chapter 2, the potential of the Lower Carboniferous is dependent on the location within the platform structure. Mineralogical analysis showed a laminated wackestone/packstone structure with fragmented bioclasts (e.g. brachiopods). This suggests the samples are presumably from the shelf/ramp of the platform. The deep sea Culm facies can therefore be excluded. Additionally, the present dolomitization confirms its Tournaisian origin according to Geluk et al. (2007).

6.2. Mechanical Characterization

The average UCS of the Lower Carboniferous rock is 138 MPa and can therefore be classified as a high-strength rock (ISRM, 1979). With a minimum UCS value of 116 MPa and a maximum of 158 MPa, the strength values vary considerably. This high strength and large range of UCS values is already presented by literature values (Table 11; Bell, 1981). Despite the higher porosity of 2.9%, the Lower Carboniferous limestone investigated by Bell (1981) is comparable to the rock in this study in terms of deformation behaviour, age and rock strength. The limestone from Bell is collected at Derbyshire and consists of over 95% calcium carbonate and its permeability is governed by karstic features.

Origin	Name	Age	Porosity [%]	UCS [MPa]			Reference
				Average	Min	Max	
Buxton, Derbyshire	Chee Tor Beds	Dinantian	2.9	106	65	171	Bell, 1981
Aachen	Kolenkalk	Dinantian	0.8	138	116	158	This study

Table 11: Literature values of the unconfined compressive strength of Carboniferous limestone

Since the porosity of our investigated samples are all in the range of 0.2% – 1%, the variation in compressive strength is presumably not affected by porosity variations. More likely, the compressive strength is affected by variations in micro-crack density, composition and textural properties (Bell, 1981; Hamdi et al., 2015). A diversity in the textural properties such as pore size diameter and grain size are indicated by MIP and the thin section analysis. The MIP showed a difference in pore diameter of one order in magnitude based on two different samples. Within the thin sections, heterogeneity on micro scale level is identified by different grain sizes, suggesting evidence for the variations in UCS (Singh, 1988).

In general, the rock strength increases as the confining pressure is raised. The confining pressure counteracts the opening of fractures, resulting in a larger compressive strength (Fossen, 2010). The x/y-oriented cores showed clearly this relation. In contrast, the z-oriented samples showed less increase of the compressive strength at higher confining pressures. According to Fossen (2010), the higher compressive strength due to the confining pressure is the result of a larger strain accumulation. As the Young's modulus is not increasing for the z-oriented cores at higher confining pressure, there is no extra strain accumulating prior to the deformation. This could explain the minor increase in compressive strength of the z-oriented cores. The x/y-oriented cores do show a higher Young's modulus at higher confining pressures, which corresponds to the 'strain accumulation'. As expected the compressive strengths are higher at higher confining pressures. According to the absolute values between both sample orientations, the compressive strengths are comparable at the lower confining pressures. However at higher confining pressures (40 MPa), there is a clear difference between the strength values of the different orientations. This results in an orientation dependent failure criterion, which is explained in more detail in 6.4.

Comparing the stress-strain relation of the triaxial compressive test to the UCS test, a clear difference in deformation behavior is observed. The UCS tests showed only elastic deformation prior to ultimate failure, suggesting a high degree of brittleness. The triaxial compressive tests showed an elastic behavior which turned gradually into inelastic deformation, meaning no specific yield point can be obtained. Within this inelastic deformation stage, no pore fluid flowed into the sample. This suggests there is no significant pore space increase or micro-fracture opening resulting in a potential improvement of the permeability or porosity prior to ultimate failure.

The tensile strength values showed a clear distinction between the different sample orientations. In case the bedding is parallel to the applied load, the tensile fracture formed along the bedding plane. In case the bedding was perpendicular to the applied load, small side fractures are formed along the bedding plane. Both observations indicate a plane of weakness along the bedding plane. Therefore the rock is considered as a transverse anisotropic rock. Although there is a wide difference in tensile strength values, the Brazilian disc tests performed by Bakker (Appendix C) showed almost no difference between tensile strengths of the different orientations. The samples used in this research showed clear coloured bedding layers from light grey to dark grey. However, the bedding was less visible in the samples of Bakker. Based on this observation, it is suggested the lower Carboniferous limestone can be described as a anisotropic heterogeneous rock.

Within the Brazilian disc test the failure is assumed to start at the centre under the following stress states:

$$\sigma_1 = \frac{6P}{\pi Dt}, \quad \sigma_2 = 0, \quad \sigma_3 = -\frac{2P}{\pi Dt}$$

Assuming a plane of weakness along the bedding, the lowest tensile strength is expected in case the minimum principal stress (tension) is perpendicular to the bedding. This is confirmed by the lower tensile strength values derived from the experiments in this research. The two other orientations both have the bedding parallel to the minimum stress,

however their bedding orientation with respect to the intermediate and maximum principle stress is different. The intermediate stress is assumed to be zero and therefore has no effect on the fracture initiation (Fairhurst, 1964). The maximum principle stress is in one case perpendicular and in the other case parallel to the bedding. Although there is a difference in stiffness based on the Young's modulus, both the orientations cannot be separated based on the tensile strength properties. Therefore, both orientations can be approximated as one group.

The fracture toughness values determined in this study show different values based on the fracture orientation with respect to the stress field. In case the load was perpendicular to the bedding, the fracture toughness was 1.5 to 2.0 times larger in case the load was parallel to the bedding plane. Considering the relative small standard deviation, tensile fractures within the bedding plane will propagate at lower stress levels. The fracture toughness values obtained by Bakker (Appendix C) did not show this relation. Although the fracture toughness values determined in this study are comparable to the results of Bakker, the average and wide range of the combined data show no bedding dependency.

In the study of Guo et al. (1993), the mode I fracture toughness of two different limestones using Brazilian disc tests was determined. A white and a grey limestone showed a mode I fracture toughness of $1.38 \text{ MPa}\cdot\text{m}^{0.5}$ and $1.58 \text{ MPa}\cdot\text{m}^{0.5}$, respectively and are higher compared to the average K_{IC} of $0.8 \text{ MPa}\cdot\text{m}^{0.5}$ obtained in this study. In comparison to other rock types, such as sandstone and basalt, the mode I fracture toughness is relatively low. The mode I fracture toughness of sandstone and basalt are $0.67 \text{ MPa}\cdot\text{m}^{0.5}$ and $3.01 \text{ MPa}\cdot\text{m}^{0.5}$, respectively. This relatively low K_{IC} indicates the rock is brittle and fractures in tensile mode will propagate more easily.

The fracture toughness, as described by equation (27), is based on a dimensionless crack length of 0.8. However, the exact crack length observed during the experiments was hard to identify, resulting in a possible range of dimensionless crack lengths. According to Figure 3.4 a smaller crack length has relatively minor effect on the fracture toughness. On the other hand a larger crack length results in a significant difference of the fracture toughness. Comparison of mutual differences between the fracture toughness values can be inconsistent if the initial crack length varies. So far, no fracture toughness data from the Lower Carboniferous limestone is available. In addition, fracture toughness data is retrieved from different experimental setups. Absolute values derived in this investigation can therefore be different in comparison to other data.

A mode II fracture toughness of $10.3 \text{ MPa}\cdot\text{m}^{0.5}$ is derived from the PTS test at an effective pressure of 20 MPa. Compared to the results of Backers (2002), the mode II fracture toughness is relatively high. This results in a high K_{IIc}/K_{IC} ratio of ~ 6.5 at 20 MPa, suggesting predominantly mode I fracturing. Within the three other PTS experiments no fracture toughness could be established since a horizontal fracture formed at the top of the bottom notch (Figure 6.1). This fracture caused the break-off of the lower inner cylinder.

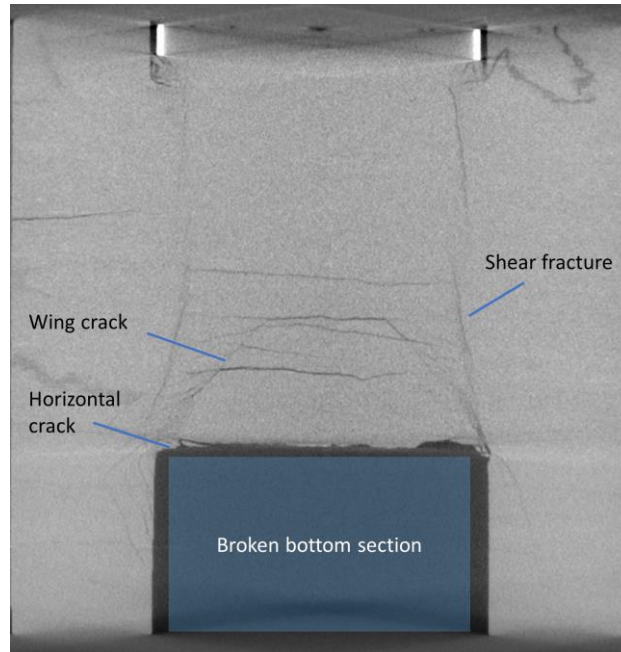


Figure 6.1: A CT image of the failed PTS experiment. The bottom part (highlighted) is broken by a horizontal crack. A wing crack and shear (not connecting top and bottom) fracture are both indicated.

According to the fracture development, the first fracture that appears is a wing-shaped crack initiated from the bottom notch (Backers, 2002). This wing-shaped fracture is also identified in the CT image of the failed PTS test (Figure 6.1; Appendix G). At a certain point, the wing crack continued horizontally resulting in the break off of the lower inner cylinder. Since all PTS samples have a bedding in the horizontal direction, the crack propagated along one of the weak bedding planes. Backers (2002) stated the relation between confining pressure and mode II fracturing is influenced by mode I fracturing for confining pressures below 30 MPa. At confining pressures above 30 MPa, only mode II fracturing is present and the initiation of wing-cracks is rare. However, in this investigation, wing cracks are observed at both an effective pressure of 20 MPa and 40 MPa. In addition, Backers concluded the influence of wing cracks on the shear fracture toughness is negligible. However, the wing cracks in this study do influence the fracture propagation and the final fracture pattern.

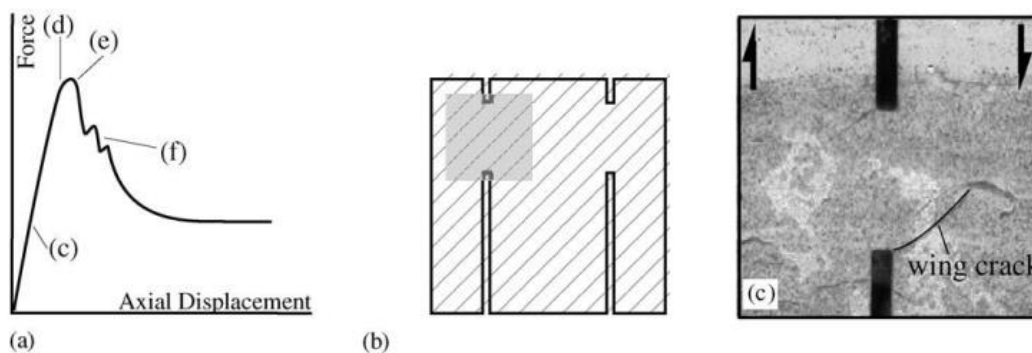


Figure 6.2: Fracture development of within the PTS experiment indicated by the different stages during the axial displacement (a). The location (b) and the geometry of the wing crack (c) at 30% of the maximum load are indicated (from Backers, 2002).

Since only one K_{IIC} value could be established, quantitative comparison with other K_{IIC} values and the K_{IC} value of the Carboniferous limestone is limited. The influence of weak bedding planes obstruct the initiation and propagation of a shear fracture. As the influence of the Mode I fracture toughness decreases with increasing confining pressure, predominant mode II fracturing will occur at higher confining pressures. Therefore, creating shear fractures might be possible at higher effective pressures. Overall, the PTS test is limited for transverse anisotropic rock samples at effective pressures below 40 MPa.

The elastic moduli of the samples are determined by axial loading and ultrasonic measurements both at ambient conditions. In addition, the static method is used for the determination of the moduli at reservoir conditions i.e., at saturated and confined samples. Since the elastic moduli describe the behaviour of the rock during elastic deformation, these parameters are of high importance for numerical models, especially in terms of a changing stress fields and hydraulic stimulation.

According to Walsh and Brace (1966), an increase of Young's modulus and Poisson's ratio is expected as cracks are more closed at higher confining pressures. The elastic moduli determined in this study did not show this relation. On one hand this can be attributed to the negligible fracture closure due to the low initial porosity of the rock sample. On the other hand micro scale mechanical rock properties affect the elastic moduli. Microcracks and grain contacts both affect the elastic moduli. Since the Young's modulus and Poisson's ratio are determined from different samples, the micro scale properties can be different for each sample. The heterogeneity of the samples therefore have a significant influence on the elastic moduli.

Eissa & Kazi (1988) showed the difference between static and dynamic data by different empirical relations. In general the values of the static moduli are around 10 per cent lower compared to the dynamic moduli. Since this 10 per cent is comparable to the discrepancy between different samples and measurement methods, both the elastic and static method should provide a good estimation of elastic moduli (Ciccotti, 2004). However, the obtained elastic moduli in this work show a larger difference (>10%) between the static and dynamic method. For example, the Young's modulus based on the static method within the x/y-direction is 23% less. Within the z-direction this is 24% less. Since the acoustic measurements showed clearly the p- and s-waves, the error of picking the right transit time is quite small. In addition, the determination of the bulk density by measuring the sample dimensions is done accurately. This excludes a difference in elastic modulus by the uncertainty of the ultrasonic measurements. However, the elastic moduli derived from the UCS test entail more uncertainties. The Young's modulus is defined in the elastic region, i.e. between 40 MPa and 80 MPa. However, the stress-strain curves do not show a full linear relation. Another method to determine the Young's modulus by the UCS method suggested by ISRM is the relation between stress and strain at 50% of the failure stress. This results in a difference up to 10% within the Young's modulus and even a difference of 35% for the Poisson's ratio (Appendix F).

6.3. Hydraulic Characterization

A number of experiments were carried out to define the porosity and permeability of the rock specimen at different conditions. It is recognized that the porosity of the rock samples is low, ranging from 0.21% to 1.00% at ambient conditions. The helium pycnometer showed both the largest variation and the largest uncertainty. Comparable porosity values are established by the electron probe images. The small variation in porosity values is presumably the result of local heterogeneity caused by the dolomitization. This low matrix porosity has a negative effect on the rock potential as it (1) provides a low storage capacity and (2) it results in low matrix permeabilities.

The low matrix permeabilities are confirmed by two different flow-through experiments. Permeability values obtained within the triaxial cell by water flow-through range from 3 to 154 μD at ambient conditions. A clear difference is determined between the different orientations, such that the k_{parallel} is a factor 10 larger compared to the $k_{\text{perpendicular}}$. This is mainly caused by the horizontal alignment of the minerals causing a higher tortuosity, as indicated by the microprobe analysis (Figure 4.3).

The above discussed porosity and permeability values are determined at atmospheric to low effective pressures. In order to quantify these parameters at reservoir conditions, the

hydrostatic pressure is increased while measuring the permeability or the change in porosity. Results show an exponential decay of the porosity and permeability as a function of effective pressure. David et al. (1994) attributed this compaction mechanism to the closure of microcracks. Even lower permeability values were observed by a gas flow-through experiment. At effective pressures between 4 and 6 MPa, a corrected fluid permeability of 0.17 μD and 0.31 μD was obtained. Although significant differences are observed within the different experimental setups and between the different samples, the impact is rather small since the transmissivity are below the economic threshold of 1 Dm.

In this study, the Terzaghi's effective stress principle is used, which assumes a Biot's coefficient of 1. However, all experiments showed a decrease of Biot's coefficient with increasing confining pressure. Since the squeezed out pore fluid is affected by temperature changes and Biot's coefficient values above 1 are observed, the obtained Biot's coefficients have an uncertainty up to ± 0.3 . The implementation of the obtained coefficients is therefore limited. Nevertheless, the decreasing change in Biot's coefficient at higher confining pressures can be used as a guideline. At pore pressures of 40 MPa, which are expected at reservoirs deeper than 4000 m, a change in the pore pressure has minor effect on the Biot's coefficient compared to shallower reservoirs.

In order to meet a minimum flow capacity of 1 Dm, the minimum required permeability of the Lower Carboniferous can be determined. In case of a reservoir thickness of 660m (e.g., UHM-02), a minimum permeability of 1.5 mD is required. Since the permeability of the investigated samples is significantly lower at reservoir conditions, it is conclusively demonstrated the intact rock permeability is insufficient.

6.4. Influence of the Bedding on Mechanical and Hydraulic Properties

The bedding of the Lower Carboniferous limestone plays a significant role in both the mechanical and hydraulic properties. Within several failure tests (Brazilian disc, uniaxial compression, triaxial compression and PTS), the rock samples showed fractures along the bedding plane. Within the Brazilian tests, the opening fracture initiated along the bedding perpendicular to the minimum principle stress. In addition, accompanied tensile fractures within shear deformation also followed the bedding plane. This can be attributed to the lower Mode I fracture toughness and tensile strengths parallel to the bedding. Within shale formations these weak bedding planes are observed extensively and it is suggested weak cement is the main reason. In addition, the preferred micro pore orientation as shown in Figure 4.3 reinforces the ability to create fractures. The weak planes and thus the transverse anisotropy of the rock can have a major effect on the wellbore stability under specific angles and should be considered within the trajectory of a well design (Wang, 2017; He, 2015). The bedding also influences the Young's modulus of the rock. Since these micropores are aligned parallel to the bedding, the pores will compact during the application of load perpendicular to the pore alignment. This results in relatively high strain measurements during the UCS test, causing a lower Young's modulus for the x/y-oriented cores.

6.5. Reservoir Improvement by Shear Fracturing

The mechanism of stimulation in EGS is assumed to be induced slip and the propagation of existing fractures. (McClure and Horne, 2013; Ye et al., 2017; Appendix H). Slip is successfully simulated by two different experimental setups and showed an improvement of the overall permeability after a fracture is created. In this paragraph, the validity of both experiments is discussed and section 6.6 focuses more on the implications of shear fracturing.

After the initiation of the shear fracture within the PTS experiment the results showed both dilation and an increase of permeability. The total rock permeability increased from $<1 \mu\text{D}$ to $\sim 45 \text{ mD}$ due to a maximum fracture opening of 0.1 mm. This fracture width corresponds to a fracture permeability of 8 D according to the arithmetic averaging method. However,

the cubic law suggested a larger fracture permeability of two orders of magnitude. This discrepancy is likely a combination of (1) the determination of the aperture thickness and (2) the applicability of the cubic law for this experimental setup.

At the point of failure the shear displacement of the fracture is zero. The rock fracture surface has a certain topography i.e., the surface roughness, and causes a fracture aperture if the fracture is displaced. The mean aperture of a displaced fracture is the result of (1) the surface roughness (2) the sustainability of the asperities during shear and (3) the fracture closure ratio (Renshaw, 1995; Appendix H). Figure 5.23 shows a constant decrease of the lateral strain between 0.7 mm and 1.2 mm. This results in the increase of aperture thickness (Figure 5.25). Within the same interval, and in particular towards the end of the displacement, a stagnation of the increase in permeability is observed. A constant aperture increase should result in at least a linear increase of permeability equation in case of arithmetic averaging and an exponential increase based on the cubic law (equations (29)-(29), respectively). It is therefore suggested a change in the permeability stagnation indicates an increase in fracture closure ratio, presumably as a result of mechanical deformation of asperities during shear.

Long term flow-through is continued for around 14 hours and suggested a slight decrease in permeability due to the transportation and plugging of small rock fragments. The constant permeability and lateral strain over the whole period proves a sustainable fracture flow without mechanical changes. Additionally, the sustainability of the shear fracture is proven by performing pore pressure cycling. Previous studies demonstrated a decrease in fracture permeability by asperity degradation after cycling the normal stress (Gale, 1982; Selvadurai, 2015) or confining pressure (Hofmann et al., 2016). However, a degradation of fracture permeability is not observed, on the contrary, permeability slightly increased after three full pore pressure cycles. Due to the high strength of our rock samples, failure of asperities is less expected as suggested by Hofmann et al. (2016). In addition, the shear displacement already removed weak asperities as indicated by the permeability stagnation, which is probably caused by the different fracture geometry. The fractures in this study are pure shear, where Hofmann et al. (2016) sheared a tensile induced fracture. Additionally, the effective pressure is varied up to 10 MPa compared to 50 MPa in the experiment of Hofmann et al. (2016). However, this gives only an explanation for a non-decreasing permeability and does not give any evidence for an increasing permeability. Since the loading piston during pressure cycling is at a fixed position, a decrease of effective pressure causes expansion of the sample, resulting in the increase of vertical load. At an effective pressure of 15 MPa in the second cycle, the vertical load is less compared to the first cycle, indicating inelastic deformation of the sample. If this deformation involves the formation of micro-cracks, permeability of the sample might increase. Another option is a small slip event occurred due to the fixed piston position resulting in a higher flow rate. However, the increase of permeability cannot be identified at or closely after low effective pressures. Another explanation for the increase in permeability is the washout of gouge and debris fill. This can be a result of fracture opening and closure due to the variations in effective pressure causing a change in the direction and velocity of the fluid flow.

The lateral strain was not fully constant after a period of 20 minutes (Figure 5.27). This can be the effect of slow pressure diffusion due to the low matrix permeability. In order to prove the steady-state condition within our experiment, a numerical model of pressure distribution within the fracture and matrix is simulated. So far, the matrix permeability was defined as $<1 \mu\text{D}$. Therefore both the upper limit ($1 \mu\text{D}$) and lower limit ($0.1 \mu\text{D}$) of the matrix permeability is used. Both scenarios showed steady state within 1 and 10 minutes, respectively (Figure 6.3). Within the fracture, steady state is reached within one second. It is therefore believed the pressure is fully distributed throughout the sample and mechanical creep affects the change in lateral strain.

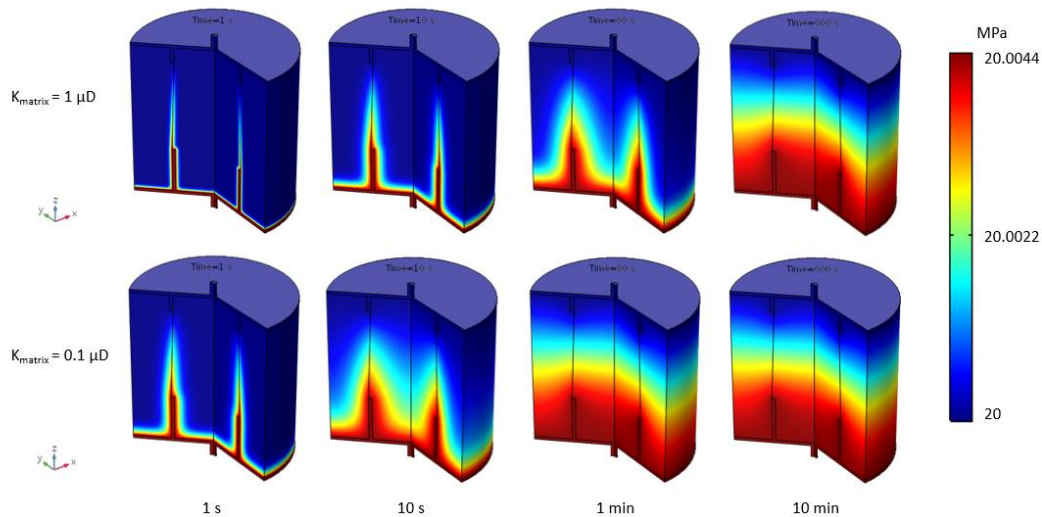


Figure 6.3: The pressure distribution of the matrix and fracture at different time steps.

The shear fracture created by triaxial deformation showed almost no improvement of the permeability at the effective pressures above 10 MPa and little increase of permeability is observed at effective pressures below 10 MPa. Based on the inlet area and fracture aperture, the fracture permeability can be obtained. However, the complex fracture geometry shown in Appendix G, limits a proper estimation of the fracture permeability. Multiple non-connecting fractures at the top of the sample contribute to the aperture opening, however these do not contribute to the fluid flow. This results in an overestimation of the effective aperture and underestimation of the fracture permeability. Besides the determination of the aperture by the strain measurements, aperture is determined optically using CT images of the fracture. The main disadvantage of this method is thickness measurements are performed at atmospheric pressures. However, it gives a reliable estimation of the upper limit of the fracture thickness.

Apart from the aperture, the inlet and outlet area at the top and bottom of the sample is necessary to determine the fracture permeability. Since the inflow area cannot be obtained by the naked eye, a CT scan of the CK06-AA-01-02-05s sample is performed to determine the geometry of the shear fracture (Appendix G). Extraction of both the in- and outlet area is difficult since (1) the image shows a lot of noise at both the top and bottom of the sample and (2) a complex fracture structure instead of a single fracture is present.

Compared to the PTS fracture, the triaxially induced fracture differs significantly in sample dimension, fracture geometry and fracture displacement. Considering the complex fracture geometry and the discrepancy in aperture thickness of triaxially induced shear fracture, no fracture permeability can be obtained. In contrast, the PTS test contains the possibility to simulate the fracture initiation of a real shear fracture during flow-through. Nevertheless, both experiments contribute to the understanding and effect of one single shear fracture.

6.6. Reservoir Implications and the Potential of EGS within the Lower Carboniferous Limestone

The intact rock might not be suitable as a reservoir rock, because the permeability is too low to meet the minimum required transmissivity. Therefore, the focus must be on secondary features, such as fractures. As discussed in Chapter 2, the secondary permeability features led to sufficient flow rates at shallower Lower Carboniferous reservoirs. However, at depths > 4000 m, higher temperatures and a different stress field can lead to a lower reservoir permeability. Compaction due to a larger overlying rock mass and the precipitation of minerals closes natural fractures and karst zones. However, sufficient flow rates within an analogue carbonate reservoir at more than 4 km is confirmed within the Tengiz oilfield

(Harris, 2008). Overall, due to the heterogeneity of the Lower Carboniferous, predicting the in-situ conditions at this depth remains uncertain. Drilling an exploration well is therefore the ideal opportunity to overcome these uncertainties. If karst features and natural fractures are present, these areas should be used as the main target. If it turns out the natural pathways are absent or show insufficient flow rates, the development of EGS within the Lower Carboniferous intends to improve the overall reservoir permeability.

As demonstrated in our experiments, the permeability is successfully improved by creating and displacing a sustainable shear fracture. The sustainability of the shear fracture implies the self-propping effect. Therefore the use of hydraulic stimulation, which creates in general both tensile and shear fractures, is considered as a potential EGS method for this reservoir without using proppants. In particular because Evans (2005) demonstrated shear fractures are the main contributors to the reservoir permeability. The revealed sustainability of the fracture does not imply a sustainable fracture for the entire lifetime of a geothermal project (> 30 years). Chemical processes, pressure solution and subcritical crack growth might affect the fracture permeability, either positively or negatively, due to temperature and pressure changes. These processes need to be investigated to determine the long term effect on fractures.

The final reservoir permeability after enhancement is dependent on the size, amount and orientation of fractures. Because the large overburden weight and the presence of a NW-SE extensional regime in the Netherlands, the minimum horizontal stress is expected within the NW-SE direction. Assuming no tectonic stresses, the minimum horizontal stress can be quantified by Eaton's formula:

$$\sigma_{h,min} = \frac{\nu - 1}{\nu} (\sigma_v - P_p) + P_p$$

The failure criteria defined in this study allow us to predict the fracture mode for two different rock orientations. By using the $\sigma_{h,min}$ and the σ_v , a pore pressure increase as a result of the hydraulic fracturing will move the Mohr circle into the unstable region (Figure 6.4). However, the large confidence intervals of the determined friction coefficient limit the prediction of the dominant fracture mode. In order to make a better prediction of the predominant fracture mode, the local stress field needs to be determined.

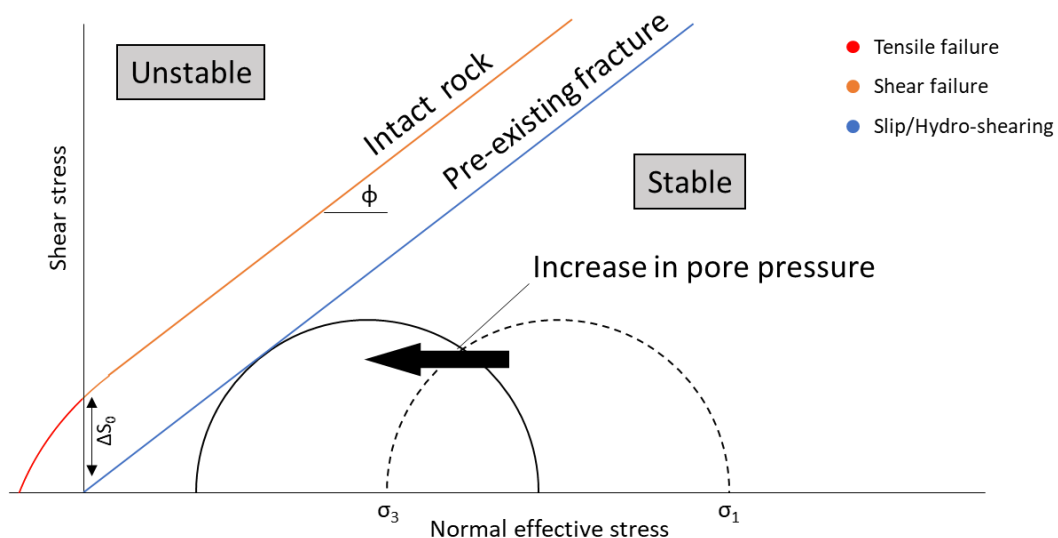


Figure 6.4: Effect of hydraulic stimulation on the rock stability. The region of the intersection between both failure envelope and Mohr circle indicates the preferred fracture mode.

Fractures along the weak bedding plane are encountered in the shear experiments. This observation plus the high K_{IIC}/K_{IC} ratio suggest horizontal tensile fractures are likely to initiate and propagate along the bedding in the reservoir. In combination with different

oriented shear fractures, an extensive fracture network can be generated. Their limited contribution to the overall permeability might be improved by the use of proppants to keep the fractures open. If this results in a sustainable network of both tensile and shear fractures, the reservoir potential increases significantly due to a higher percolation.

This work focused on the failure of the intact rock by hydraulic stimulation. It should be noted that present natural discontinuities as fractures and faults, but also veins, are more likely to slip or propagate instead of failure of the intact rock (Figure 6.4). This is mainly due to the lower cohesion of an individual fracture compared to the cohesion of an intact rock (Jaeger, 2007). The main advantage of these natural discontinuities is less pore pressure increase is required to displace the fractures.

Assuming a fault is a large scale representation of a shear fracture, pressure variations as showed within the PTS test will not change the permeability significantly. Moreover, displacement of the fault will only increase the permeability. However, approximating a slipping fault as an upscaled shear fracture is questionable and this assumption should be studied in more detail. More importantly, the slippage of a major fault might facilitate microseismicity. In particular, large faults have a significant potential to induce a seismic event (McClure, 2012). It is therefore suggested to investigate the presence of faults in the near well-bore region.

Although natural discontinuities are present in a reservoir, McClure and Horne (2013) argued a combination of preexisting fractures **and** newly formed fractures will exist under specific conditions. Since the preexisting fractures might have been formed under different stress conditions, their main orientation can be different. The application of hydraulic stimulation could therefore generate a network of different oriented shear fractures, which affect the percolation.

Given the high content of calcite and dolomite from the microstructural analysis, acidizing can be applied to enhance the reservoir permeability. Since calcite reacts with the acids, it forms conductive channels (wormholes) within the rock matrix. Additionally, the acid will leave the veins empty since these consist fully of calcite minerals. In particular the existing micro-network within the veins allows the acid to propagate relatively fast and create a wide fracture network. In case a wide vein network is present, the use of acidizing is therefore a viable technique to improve the reservoir. Acid treatments in the carbonate Molasse Basin (Germany) led, in some wells, to a significant increase of the productivity. However, it primarily cleaned the wellbore region instead of creating flow pathways in the matrix (Schumacher and Schulz, 2013). Dependent on the connectivity of the pre-existing vein network, even a combination of hydraulic fracturing and acidizing can be considered to enlarge the total reservoir permeability.

7

Conclusions and Recommendations

In this experimental study, the mechanical and hydraulic rock properties of Lower Carboniferous limestone rock samples have been investigated. A variety of experiments was performed to quantify the mean and range of the intact rock parameters. Since all rock samples were taken from the same block, the rock shows a high degree of heterogeneity within a small scale. A clear transverse anisotropy is established based on both mechanical and hydraulic parameters. In particular, the tensile strength and mode I fracture toughness have lower values within the lateral direction. Microscopic analysis confirmed this transverse anisotropy by the grain alignment and a specific pore structure. This resulted in an overall $k_{\text{parallel}}/k_{\text{perpendicular}}$ ratio of one order of magnitude.

The porosity and permeability of the intact rock, especially at reservoir conditions, is far below the minimum required flow capacity. It is concluded secondary permeability features are needed for economically profitable production rates. These secondary features can be present in the form of karst or natural fractures, as revealed within the shallower Lower Carboniferous reservoirs and analogous deep limestone reservoirs. An investigation on the natural fracture network within the Lower Carboniferous needs to be performed to implement the discontinuities on macroscopic scale.

In case no natural permeable features are present, it is demonstrated this rock successfully improved the permeability by induced fractures. Two different experimental setups are used to determine the permeability of a shear fracture. Although the PTS test is limited for transverse anisotropic rock samples, it is an innovative method to monitor the shear fracture permeability continuously. Shear fractures showed an improvement of the total rock permeability of one to four orders of magnitude. It is shown the permeability increased with increasing fracture displacement of the rock. Relative minor variations in the permeability are observed due to a change in effective pressure. Overall, the formed fracture showed a sustainable behaviour as it remained stable over time and after pressure variations. Future investigation is needed to prove the long term sustainability of the shear fracture. Additionally, one extra PTS test should be performed to confirm the results within thesis.

Hydraulic stimulation is considered as a potential EGS method since sustainable shear fractures show a significant increase of permeability. The high ability for tensile fracture propagation, especially along the weak bedding planes gives an extra opportunity to improve the permeability even further. Moreover, the presence of natural discontinuities has a significant influence on the final percolation of the reservoir. Acidizing the rock matrix - in particular when an existing vein network is present - is a considerable technique for our formation.

It can be concluded this work contributes to the development of the Lower Carboniferous limestone as a target for ultra-deep geothermal energy. The limits and opportunities of this formation are exposed and can be used as starting point for further research.

Bibliography

ASTM D3967-05, (2005). Standard Test Method for Splitting Tensile Strength of Intact Rock Core Specimens. *ASTM International*.

Abdel-Ghaney, M. A., Siso, S., Hassan, A. M., Pierpaolo, P. & Roberto, C. (2011). New Technology application, radial drilling petrobel, first well in Egypt. *10th Offshore Mediterranean Conference and Exhibition, Italy*.

Adams, C.A., Auld, A.M.C., Gluyas, J.G. and Hogg, S. (2015). Geothermal energy – The global opportunity. *J Power and Energy*, 227(7): 747-754.

Akesson, U., Hansson, J., Stigh, J. (2004) Characterization of microcracks in the Bohus granite, western Sweden, caused by uniaxial cyclic loading. *Eng Geol* 72:131–142

Backers, T., Stephansson, O. and Rybacki, E. (2002). Rock fracture toughness testing in Mode II – punch-through shear test. *Int J Rock Mech Min Sci* 39 (6): 755-769.

Backers, T. (2004). Fracture Toughness Determination and Micromechanics of Rock Under Mode 1 and mode 2 Loading. Dissertation Universität Potsdam.

Backers, T., Stephansson, O. (2012). ISRM suggested methods for the Determination of Mode II Fracture Toughness. *Rock Mechanics and Rock Engineering Vol 45*, pp. 1011-1022.

Bell, F.G. (1981). A survey of the physical properties of some carbonate rocks. *International association of Engineering Geology*.

Blöcher, G., Reinsch, T., Hassanzadegan, A., Milsch, H., Zimmermann, G. (2014). Direct and indirect laboratory measurements of poroelastic properties of two consolidated sandstones. - *International Journal of Rock Mechanics and Mining Sciences*, 67, pp. 191–201.

Boxem, T.A.P., Veldkamp, J.G. & van Wees, J.D.A.M. (2016). Ultra-diepe geothermie: Overzicht, inzicht & to-do ondergrond. TNO 2016 R10803 — Eindrapport

Brace, W.F., Walsh J.B., Frangos, W.T. (1968). Permeability of Granite under High Pressure. *Journal of Geophysical Research*. 73 (6): 2225-2236

Ciccotti, M. & Mulargia, F. (2004) Differences between static and dynamic elastic moduli of a typical seismogenic rock. *Geophys. J. Int.*, 157, pp.474–477.

Colmenares, L. B. & Zoback, M. D. (2002). A statistical evaluation of intact rock failure criteria constrained by polyaxial test data for five different rocks. *International Journal of Rock Mechanics & Mining Sciences*, 39 (2002) 695 – 729.

David, C., T.-F. Wong, W. Zhu, J. Zhang. (1994). Laboratory measurement of compaction-induced permeability change in porous rocks: implications for the generation and maintenance of pore pressure excess in the crust *Pure Appl Geophys*, 143 (1–3), pp. 425-456

Duin, E.J.T., Doornenbal, J.C., Rijkers, R.H.B., Verbeek, J.W. and Wong, Th.E. (2006). Subsurface structure of the Netherlands – results of recent onshore and offshore mapping. *Netherlands Journal of Geosciences* 85 (4), 245

- Dunn DE, LaFountain LJ, Jackson RE (1973) Porosity dependence and mechanism of brittle fracture in sandstones. *J Geophys Res.* 78:2403–2417
- Economides, M.J., Nolte, K.G., (2000). Reservoir Stimulation, 3rd Edition. *Wiley and Sons Ltd., United Kingdom.*
- Evans, K.F., Genter, A. & Sausse, J. (2005). Permeability creation and damage due to massive fluid injections into granite at 3.5 km at Soultz: 1. Borehole observations. *Journal of Geophysical Research*, 110 (B04203).
- Fairhurst, C. (1964). On the validity of the 'Brazilian' test for brittle materials. *Int. J. Rock Mech. Mining Sci.* 1: 535-546.
- Ferrill, D.A., Winterle, J., Wittmeyer, G., Sims, D.W., Colton, S. Armstrong, A., Morris. A.P., (1999). Stressed rock strains groundwater at Yucca Mountain, Nevada. *GSA Today* 9(5): 1-8.
- Fraser, A.J. & Gawthorpe, R.L., (1990). Tectono-stratigraphic development and hydrocarbon habitat of the Carboniferous in northern England. In: R.F.P. Hardman and J. Brooks (eds), Tectonic events responsible for Britain's oil and gas reserves. Geological Society Special Publication (London) 55: 49-86.
- Franquet, JA & Abass, HH 1999, Rock Mechanics for Industry, in B Amadei, RL Kranz, GA Scott & PH Smeallie (eds), Balkema, Rotterdam, pp. 349–355.
- Gale, J.E. (1982). The effects of fracture type (induced versus natural) (on the stress-fracture closure-fracture permeability relationships). In: Proceedings of the 23rd U.S. Symposium on Rock Mechanics (USRMS). Berkeley; 290– 298.
- Gao, Z. and Hu, Qinhong (2013). Estimating permeability using median pore-throat radius obtained from mercury intrusion porosimetry. *J. Geophys. Eng.* 10
- Golewski, G. L. (2017). Generalized Fracture Toughness and Compressive Strength of Sustainable Concrete Including Low Calcium Fly Ash. *Materials*, 10 (12), 1393
- Guo, H., Aziz, N.I. & Schmidt, L.C. (1993) Rock fracture-toughness determination by the Brazilian test. *Engineering Geology*, 33 (1993) 177-188.
- Hamdi, P., Stead, D. Elmo, D. (2015). Characterizing the influence of stress-induced microcracks on the laboratory strength and fracture development in brittle rocks using a finite-discrete element method-micro discrete fracture network FDEM- μ DFN approach. *Journal of Rock Mechanics and Geotechnical Engineering.* 7 (6), 609-625.
- Harris, M. (2008). Geologic Framework for the Tengiz and Korolev Fields, Kazakhstan – Carboniferous Isolated Carbonate Platforms, Adapted from 2000-2001 AAPG International Distinguished Lecture
- He, S. Liang, L., Zeng, Y., Ding, Y., Lin, Y., Liu, X. (2015). The influence of water-based drilling fluid on mechanical property of shale and the wellbore stability. *Petroleum* 2 (2016) 61-66
- Hoffman, H., et al. (2016). Transmissivity of Aligned and Displaced Tensile Fractures in Granitic Rocks During Cyclic Loading, *International Journal of Rock Mechanics and Mining Sciences*, 87, 69-84.

Hondros, J. R., (1959). The evaluation of Poisson's ratio and the modulus of materials of a low tensile resistance by the Brazilian (indirect tensile) test with particular reference to concrete. *Aust. J. Appl. Sci.*, 10: 243-268.

Jaeger, J. C. (1960). Shear fracture of anisotropic rocks. *Geol Mag.* 97, 65-72.

Kluge, C., Misch, H., Blocher, G. (2017). Permeability of displaced fractures. *Energy Procedia* 125. 88-97.

Kombrink, H., Van Lochem, H. & Van Der Zwan, C.J., (2010). Seismic interpretation of Dinantian carbonate platforms in the Netherlands; implications for the palaeogeographical and structural development of the Northwest European Carboniferous Basin. *Journal of the Geological Society of London*, 167/1, 99-108.

Kombrink, H., Leever, K.A., Van Wees, J.D., van Bergen, F., David, P., Wong, T.E. (2008). Late Carboniferous foreland basin formation and Early Carboniferous stretching in Northwestern Europe: inferences from quantitative subsidence analyses in the Netherlands. *Basin Research* 20. pp. 377-395.

Kramers, L, Vis, G. J., van den Dulk, M., Duin, E. J. T., Witmans, N., Pluymaekers, M. and Doornenbal, J. C.. (2012). Regionale studie aardwarmtepotentie provincie Limburg. TNO Rapport.

Lawrence, M., Jiang, Y. (2017). Porosity, Pore size distribution, Micro-structure. *Bio-aggregates Based Building Materials, RILEM State-of-the-Art Reports 23*, pp. 39-71.

Li, K. (2012). Comparison with of Geothermal energy with Solar and Wind power generation Systems. *In Thirty-Eight workshop on Geothermal Reservoir Engineering*, Stanford, California.

Markides, C. F., & Kourkoulis, S. K. (2013). Naturally accepted boundary conditions for the Brazilian disc test and the corresponding stress field. *Rock Mechanics and Rock Engineering*, 46, 959–980.

McClure, M. and Horne, R. (2013). Conditions required for shear stimulation in EGS. In: *Proceedings of European geothermal conference*, Pisa, Italy.

McClure, M. and Horne, R. (2013). Is Pure Shear Stimulation always the mechanism of Stimulation in EGS? *Thirty-Eighth Workshop on Geothermal Reservoir Engineering* Stanford University.

McCann, T. (2008). The Geology of Central Europe Volume 1: Precambrian and Paleozoic. *The Geological Society of London*.

Moro, F., Böhni, H. (2001). Ink-bottle effect in Mercury Intrusion Porosimetry of Cement-Based materials. *Journal of Colloid and Interface Science*, Vol 249, Issue 1: 262

Morris, A., Ferril, D.A., Brent Henderson, D. (1996). Slip-tendency analysis and fault reactivation. *GeoScienceWorld*. Vol. 24 nr. 3.

Olsen, R.A., Neubauer, C. M., Jennings, H.M. (1997). Damage to the pore structure of Hardened Portland Cement Paste by Mercury Intrusion. *J. Am. Ceram. Soc.* 80(9), 2454-2458

- Olsson, R. and Barton, N. (2001). An improved model for hydromechanical coupling during shearing of rock joints. *International Journal of Rock Mechanics and Mining Sciences*. 38, 317-329.
- Phillips, W. J. (1972). Hydraulic fracturing and mineralization. *Journal of the Geological Society of London*, v128 pp 337-359.
- Rijkers, R., van der Hoorn, K., Van Gijtenbeek, K., Gussinklo Ohmann, R., Nitters, G., Rombout, B., Spier, C. and Zwart, B. (2013). Enhanced Geothermal System in the Lower Carboniferous in the Netherlands – a geological and modelling study. *European Geothermal Congress 2013, Italy*.
- Reijmer, J.J.G., ten Veen, J.H., Jaarsma, B. and Boots, R. (2017). Seismic stratigraphy of Dinantian carbonates in the southern Netherlands and northern Belgium. *Netherlands Journal of Geosciences*.
- Renshaw, C.E. (1997). On the relationship between mechanical and hydraulic apertures in rough-walled fractures. *J. Geophys. Res.* 100: 24629-24636, 1995
- Rezaee M. R., Jafari, A. and Kazemzadeh, E. (2006). Relationships between permeability, porosity and pore throat size in carbonate rocks using regression analysis and neural networks. *J. Geophys. Eng.* 3 370-6
- Schön, J. H. (2011). Geomechanical Properties. *Handbook of Petroleum Exploration and Production*. 8, 245-271.
- Schumacher, S. and Schultz, R. (2013). Effectiveness of acidizing geothermal wells in the South German Molasse Basin. *Geothermal Energy Science* 1. 1-11. 2013
- Selvadurai, A. P. S. (2015). Normal stress-induced permeability hysteresis of a fracture in a granite cylinder. *Geofluids*
- Singh, S. K. (1988). Relationship among fatigue strength, mean grain size and compressive strength of a rock. *Rock Mech Rock Eng* 21(4):271–276
- Tamari, S. (2004). Optimum design of the constant-volume gas pycnometer for determining the volume of solid particles. *Meas. Sci. Technol.* 15 549.
- Tien, Y.M. and Kuo, M.C. (2001). A failure criterion for transversely isotropic rocks. *International Journal of Rock Mechanics and Mining Science* 38, 399-412.
- Van der Hoorn, K., Heijnen, L. J., Gankema, M. E. and Nitters, G. (2012). Hydraulic fracturing in limestone: a case study of two EGS projects in the Netherlands. *Thirty-seventh Workshop on Geothermal Reservoir Engineering, Stanford*.
- Van Hulten, F.F.N. (2012) Devonian-carboniferous carbonate platform systems of The Netherlands, *Geologica Belgica* 15(4)
- Walsh, J. B., and Brace, W. F. (1966). Elasticity of Rock: a Review of Some Recent Theoretical Studies. *Rock Mechanics and Engineering Geology, Vol. 4*, 283-297.
- Wang, Y., Li, C., Hu, Y., Mao, T., (2017). Brazilian test for Tensile Failure of Anisotropic Shale under different Strain Rates at Quasi-static loading. *Energies* 2017, 10 (9), 1324
- Willems, C.J.L. (2017). Doublet deployment strategies for geothermal Hot Sedimentary Aquifer exploitation: Application to the Lower Nieuwerkerk Formation, West Netherlands Basin.

Weber, J. and Bastick, M. (1968). 8 Influence de la température sur la détermination de la masse volumique de divers carbones par pycnométrie dans l'hélium *Bul. Soc. Chm. Fr.* 7 2702-6.

Ye, Z., Janis, M., Ghassemi, A. (2017). Injection-Driven Shear Slip and the Coupled Permeability Evolution of Granite Fractures for EGS Stimulation. 51st U.S. Rock Mechanics/Geomechanics Symposium, 25-28 June, San Francisco, California, USA

Ziegler, P.A. 1990. Geological Atlas of Western and Central Europe, 2nd edn. *Shell Internationale Petroleum Maatschappij B.V. Geological Society*, London.

Zimmerman, R. and Main, I. (2003). Chapter 7 Hydromechanical Behavior of Fractured Rocks. *Elsevier Academic Press*.

NLOG, (2016). Geothermal energy overview. <http://nlog.nl/en/geothermal-energy-overview>. Assessed: 2017-12-08.

IFC, (2013). Success of Geothermal Wells: A Global Study.

<https://www.rijksoverheid.nl/actueel/nieuws/2017/06/19/mogelijk-30-van-industriële-warmtevraag-door-ultradiepe-geothermie>

<https://www.rijksoverheid.nl/documenten/rapporten/2016/01/18/energie-rapport-transitie-naar-duurzaam>

List of figures

FIGURE 1.1: WORLD ENERGY CONSUMPTION (EIA, 2017)	10
FIGURE 1.2: LEFT: POTENTIAL RESOURCES IN TW (JACOBSON, 2009), RIGHT: INSTALLED POWER IN TW (LI, 2013)	11
FIGURE 1.3: SW-NE CROSS SECTION OF THE DUTCH SUBSURFACE. THE LOWER CARBONIFEROUS LIMESTONE IS INDICATED BY CARBOON KALKSTEEN GROEP (CL). SINCE THE THICKNESS OF THE LOWER CARBONIFEROUS IS UNCERTAIN, THE FORMATION IS INDICATED BY A DASHED LINE (TNO).	12
FIGURE 1.4: DIFFERENT FRACTURE MODES. LEFT: EXTENSIONAL FRACTURE (MODE I). CENTER: SHEARING FRACTURE, PERPENDICULAR TO EDGE (MODE II). RIGHT: SHEARING FRACTURE, PARALLEL TO THE EDGE (MODE III) (GOLEWSKI, 2017).....	13
FIGURE 2.1: SCHEMATIC CROSS-SECTION SHOWING THE INTERPRETED STRUCTURAL AND STRATIGRAPHIC SETTING OF THE HORST AND GRABEN STRUCTURE (KOMBRINK, 2010).....	16
FIGURE 2.2: STRATIGRAPHY OF THE CARBONIFEROUS PERIOD.....	17
FIGURE 2.3: OVERVIEWS OF THE WELLS AND CARBONATE PLATFORMS OF THE DINANTIAN. BOOTS (2015), HOORVELD (2013) AND KOMBRINK (2013).	18
FIGURE 2.4: SCHEMATIC OVERVIEW OF THE DEPOSITIONAL ENVIRONMENT DURING THE CARBONIFEROUS INDICATING THE KARSTIFICATION PROCESS DURING AND AFTER THE DEPOSIT OF THE DINANTIAN (GELUK ET AL. 2007).	19
FIGURE 2.5: CARBONATE PLAY SHOWING POTENTIAL RESERVOIR QUALITY OF THE DINANTIAN CARBONATES (TOTAL, 2007).....	19
FIGURE 2.6: LOCATION OF THE KORNELIMUNSTER QUARRY, THE QUARRY THE ROCK SAMPLES ARE COLLECTED (LEFT). THE MORE ZOOMED LOCATION INCLUDING THE GEOLOGICAL FORMATIONS AT SURFACE (RIGHT).....	21
FIGURE 3.1: DIFFERENT ORIENTATIONS OF THE DRILLED CORE SAMPLES. THE PERPENDICULAR (S) CORES ARE DRILLED IN THE Z-DIRECTION, THE PARALLEL (P) CORES ARE DRILLED IN EITHER THE X- OR Y-DIRECTION.....	23
FIGURE 3.2: SCHEMATIC OVERVIEW OF THE MTS (LEFT) AND A CROSS SECTIONAL OVERVIEW OF THE TRIAXIAL CELL AND ITS CONNECTION WITH QUIZIX PUMPS (PEI, 2016).	25
FIGURE 3.3: LEFT: SCHEMATIC OVERVIEW OF DIAMETRAL COMPRESSION DURING BRAZILIAN DISC TEST (GUO, 1993). RIGHT: THE EXPERIMENTAL SETUP OF THE BRAZILIAN DISC TEST WITHIN THE MTS.	26
FIGURE 3.4: STRESS INTENSITY FACTORS AS A FUNCTION OF DIMENSIONLESS CRACK LENGTH FOR DIFFERENT A (LEFT) AND THE STRESS INTENSITY FACTOR AS A FUNCTION OF DIMENSIONLESS CRACK LENGTH FOR ONLY 5° SCENARIO (RIGHT).	26
FIGURE 3.5: AN OVERVIEW OF THE SAMPLE PRIOR TO THE TRIAXIAL TEST. BOTH CIRCULAR AND AXIAL EXTENSOMETERS ARE ATTACHED TO THE SAMPLE.....	28
FIGURE 3.6: OVERVIEW OF THE SETUP DURING ULTRASONIC P- AND S-WAVE MEASUREMENTS.....	29
FIGURE 3.7: SCHEMATIC OVERVIEW OF THE HELIUM PYCNOMETER	30
FIGURE 3.8: SCHEMATIC OVERVIEW GAS PERMEAMETER: P(E) IS THE INLET PRESSURE, P(A) THE OUTLET PRESSURE AND P(M) THE CONFINING PRESSURE. DIFFERENT FLOW GAUGES CAN CONTROL THE FLOW RATES, WITH THEIR MAXIMUM FLOW RATE INDICATED (ML/MIN). ARGON IS USED FOR THE CONFINING PRESSURE AS WELL FOR THE FLOWING MEDIUM (FROM MILSCH, GFZ).....	32
FIGURE 3.9: LEFT: 3D VISUALIZATION OF THE SAMPLE USED FOR THE PTS TES. MIDDLE: A CROSS SECTION INCLUDING THE DIMENSIONS OF THE PTS SAMPLE. RIGHT: THE PTS SAMPLE PLACED IN THE MTS SURROUNDED BY THE CIRCULAR EXTENSOMETER.	34

FIGURE 3.10: OVERVIEW OF PTS SETUP. LEFT: INITIAL STRESS STATE BEFORE THE AXIAL LOADING. RIGHT: SITUATION AFTER APPLYING THE AXIAL LOAD TO THE SAMPLE.	35
FIGURE 3.11: LATERAL STRAIN AS A FUNCTION OF EFFECTIVE PRESSURE. THE LATERAL STRAIN IS MONITORED DURING A CONFINING PRESSURE RAMP FROM 2 UNTIL 30 MPA. EFFECTIVE PRESSURE IS DERIVED BASED ON THE EFFECTIVE PRESSURE LAW.....	37
FIGURE 3.12: SCHEMATIC OVERVIEW OF THE STEADY STATE FLOW THROUGH THE TRIAXIAL INDUCED FRACTURE.	37
FIGURE 3.13: A SCHEMATIC OVERVIEW OF THE EFFECT OF HYDROSTATIC UNLOADING. BOTH EXPANSION AND FRACTURE OPENING PLAY A ROLE. THEREFORE THE EXPANSION EFFECT IS CORRECTED TO DETERMINE THE APERTURE (EQS. 34).....	38
FIGURE 4.1: ELECTRON MICROPROBE IMAGE OF THE CKO6-AA-01-02-13S. RIGHT: DETERMINATION OF THE MINERAL COMPOSITION.....	40
FIGURE 4.2: ELECTRON MICROPROBE IMAGE OF THE CALCITE VEIN WITHIN THE CKO6-AA-01-02-13S (TOP). AN IMAGE FROM THE OPTICAL MICROSCOPE SHOWS THE CLEARLY THE VEIN WITHIN THE MATRIX (BOTTOM).....	41
FIGURE 4.3 ELECTRON MICROPROBE IMAGE OF THE CKO6-AA-01-01-19S HIGHLIGHTING THE LAYERS OF DIFFERENT GRAIN SIZES AND MINERALOGY. THE TOP PART SHOWS (PARTLY) DOLOMIZED CALCITE MINERALS.	42
FIGURE 4.4 ELECTRON MICROPROBE IMAGE OF THE CKO6-AA-01-01-12S SHOWING SHELLS AND SHELL FRAGMENTS.	42
FIGURE 4.5 ELECTRON MICROPROBE IMAGE OF THE CKO6-AA-01-01-12S SHOWING A BIOCLAST WITH INTRAPARTICLE POROSITY.	43
FIGURE 4.6: ELECTRON MICROPROBE IMAGE OF CKO6-AA-01-01-12S HIGHLIGHTING A BRACHIOPOD. BESIDES, A LARGE SHELL FRAGMENT AND A RELATIVELY HIGH DEGREE OF DOLOMITE CONTENT.	43
FIGURE 5.1: SCHEMATIC OVERVIEW OF THE BEDDING AND STRESS ORIENTATION DURING THE BRAZILIAN STRENGTH TEST. THE FIRST PART INDICATES THE BEDDING ORIENTATION, THE SECOND PART THE LOAD DIRECTION WITH RESPECT TO THE BEDDING PLANE.	44
FIGURE 5.2: STRESS-STRAIN CURVES OF THE BRAZILIAN DISC TEST OF THE DIFFERENT ORIENTED SAMPLES.	45
FIGURE 5.3: CKO6-AA-01-03-09P AFTER BRAZILIAN TEST SHOWING A MODE I FRACTURE ALONG THE BEDDING	46
FIGURE 5.4: CKO6-AA-01-02-03S AFTER BRAZILIAN TEST SHOWING AN ARBITRARY VERTICAL TENSILE FRACTURE.	46
FIGURE 5.5: CKO6-AA-01-02-11s AFTER BRAZILIAN TESTING SHOWING NON TENSILE FAILURE.....	46
FIGURE 5.6: STRESS STRAIN CURVE OF THE UCS TEST.	47
FIGURE 5.7: CKO6-AA-01-03-07P ROCK SAMPLE AFTER UNIAXIAL COMPRESSION TEST.	48
FIGURE 5.8: CKO6-AA-01-01-11s ROCK SAMPLE AFTER UNIAXIAL COMPRESSION TEST.	48
FIGURE 5.9: STRESS-STRAIN CURVES OF THE CONFINED COMPRESSIVE STRENGTH TEST OF THE X/Y-ORIENTED CORES.	49
FIGURE 5.10: STRESS-STRAIN CURVES OF THE CONFINED COMPRESSIVE STRENGTH TEST OF THE Z ORIENTED CORES.	50
FIGURE 5.11: MOHR COULOMB FAILURE ENVELOPE INCLUDING TENSILE STRENGTH, CONFINED COMPRESSIVE STRENGTH AND UNCONFINED COMPRESSIVE STRENGTH OF THE X/Y-ORIENTED SAMPLES. 90% CONFIDENCE INTERVALS SHOW THE UPPER AND LOWER BOUND OF THE FAILURE ENVELOPE.....	50
FIGURE 5.12: MOHR COULOMB FAILURE ENVELOPE INCLUDING TENSILE STRENGTH, CONFINED COMPRESSIVE STRENGTH AND UNCONFINED COMPRESSIVE STRENGTH OF THE Z-ORIENTED SAMPLES. 90% CONFIDENCE INTERVALS SHOW THE UPPER AND LOWER BOUND OF THE FAILURE ENVELOPE.	51

FIGURE 5.13: THE YOUNG'S MODULUS AND THE POISSON RATIO AS FUNCTION OF THE CONFINING PRESSURE.	52
FIGURE 5.14: POISSON'S RATIO AND YOUNG'S MODULUS DERIVED FROM ULTRASONIC MEASUREMENTS.	52
FIGURE 5.15: THE PORE VOLUME CHANGE DURING THE CONFINING PRESSURE RAMP.	53
FIGURE 5.16: SQUEEZED OUT PORE VOLUME DURING CONFINED COMPRESSION TEST. THE HIGHLIGHTED PART (BOLD) SHOWS THE PORE VOLUME CHANGE AFTER ULTIMATE FAILURE. ONLY CKO6-AA-01-03-01P SAMPLE SHOWS NO CLEAR INCREASE OF PORE VOLUME AFTER SAMPLE FAILURE.	54
FIGURE 5.17: BULK VOLUME CHANGE AND BULK MODULUS EVOLUTION AS A FUNCTION OF THE CONFINEMENT PRESSURE.	55
FIGURE 5.18: BIOT'S COEFFICIENT DETERMINED FROM THE ONE-STEP TESTING METHOD (FRANKQUET AND ABBAS, 1999).	56
FIGURE 5.19: PORE SIZE GEOMETRY DETERMINED BY THE MERCURY INTRUSION POROSIMETRY.	56
FIGURE 5.20: PERMEABILITY OF THE DIFFERENT ROCK SAMPLES AT A CONSTANT CONFINING PRESSURE OF 2 MPa. WITHIN SOME EXPERIMENTS DIFFERENT FLOW RATES ARE USED WHICH RESULTED IN MULTIPLE VALUES. THE VALUES ARE GROUPED BY ORIENTATIONS. TWO SAMPLES SHOW THE PERMEABILITY AS A FUNCTION OF EFFECTIVE PRESSURE.	57
FIGURE 5.21: PERMEABILITY MEASUREMENTS AT FOUR DIFFERENT PRESSURE LEVELS.	58
FIGURE 5.22: PERMEABILITY AS A FUNCTION OF $2/(P_{IN_POUT})$. THE INTERCEPTION OF THE DOTTED LINE AND THE Y-AXIS CORRESPONDS TO THE GAS CORRECTED PERMEABILITY.	59
FIGURE 5.23: PUNCH THROUGH SHEAR TEST OF THE CKO6-AA-01-02-02s AS A FUNCTION OF THE DISPLACEMENT RATE.	60
FIGURE 5.24: DETAILED OVERVIEW OF FIGURE 5.23 SHOWING THE START OF THE INFLOW.	60
FIGURE 5.25: MECHANICAL APERTURE DERIVED FROM THE LATERAL STRAIN. TOP: THE FRACTURE PERMEABILITY BASED ON THE ARITHMETIC AVERAGING. BOTTOM: THE FRACTURE PERMEABILITY FROM THE CUBIC LAW.	61
FIGURE 5.26: FRACTURE PERMEABILITY AND APERTURE DURING DISPLACEMENT (BEFORE VERTICAL LINE) AND AT A CONSTANT DISPLACEMENT OF 1.2 MM (AFTER VERTICAL LINE).	61
FIGURE 5.27: THE EFFECT OF THE AXIAL LOAD, LATERAL STRAIN AND PERMEABILITY AS A RESULT OF THE PORE PRESSURE CYCLES.	62
FIGURE 5.28: PERMEABILITY AND MECHANICAL APERTURE DURING THE THREE PORE PRESSURE CYCLES. THE SECOND PORE PRESSURE CYCLE IS HIGHLIGHTED.	63
FIGURE 5.29: CROSS PLOT OF THE LATERAL STRAIN AND PERMEABILITY DURING EFFECTIVE PRESSURE CYCLING.	63
FIGURE 5.30: SHEAR FRACTURE OF THE CKO6-AA-01-02-08s SHOWING THE DISPLACEMENT OF 0.22 MM.	64
FIGURE 5.31: PERMEABILITY EVOLUTION AFTER THE SHEAR DISPLACEMENT AT DIFFERENT EFFECTIVE PRESSURE OF THE CKO6-AA-01-02-08s	65
FIGURE 5.32: PERMEABILITY EVOLUTION AFTER THE SHEAR DISPLACEMENT AT DIFFERENT EFFECTIVE PRESSURE OF THE CKO6-AA-01-02-05s	66
FIGURE 6.1: A CT IMAGE OF THE FAILED PTS EXPERIMENT. THE BOTTOM PART (HIGHLIGHTED) IS BROKEN BY A HORIZONTAL CRACK. A WING CRACK AND SHEAR (NOT CONNECTING TOP AND BOTTOM) FRACTURE ARE BOTH INDICATED.	71
FIGURE 6.2: FRACTURE DEVELOPMENT OF WITHIN THE PTS EXPERIMENT INDICATED BY THE DIFFERENT STAGES DURING THE AXIAL DISPLACEMENT (A). THE LOCATION (B) AND THE GEOMETRY OF THE WING CRACK (C) AT 30% OF THE MAXIMUM LOAD ARE INDICATED (FROM BACKERS, 2002).	71
FIGURE 6.3: THE PRESSURE DISTRIBUTION OF THE MATRIX AND FRACTURE AT DIFFERENT TIME STEPS.	75

FIGURE 6.4: EFFECT OF HYDRAULIC STIMULATION ON THE ROCK STABILITY. THE REGION OF THE INTERSECTION BETWEEN BOTH FAILURE ENVELOPE AND MOHR CIRCLE INDICATES THE PREFERRED FRACTURE MODE. 76

FIGURE 7.1: OVERVIEW OF THE INVESTIGATED SAMPLES INCLUDING THEIR DIMENSIONS AND TESTS.... 89

FIGURE 7.2: OVERVIEW OF THE TRIAXIAL INDUCED SHEAR FRACTURES INDICATING THEIR FAILURE ANGLE. 90

FIGURE 7.3: TENSILE STRENGTH AND MODE I FRACTURE TOUGHNESS OF BRAZILIAN DISC TEST. THE CMA6- SAMPLES CORRESPOND TO THE EXPERIMENTS PERFORMED BY R.R. BAKKER. THE CKO6- SAMPLES CORRESPOND TO THE EXPERIMENTS PERFORMED IN THIS STUDY. 91

FIGURE 7.4: OVERVIEW OF THE ORIGINAL JAEGER'S ANISOTROPIC CRITERIA (LEFT) AND THE EXTENDED JAEGER'S CRITERIA (RIGHT) (AFTER TIEN AND KUO 2001). 93

FIGURE 7.5: DISTRIBUTION OF ROCKS WITHIN THE LOWER CARBONIFEROUS INDICATING THE BEVELAND, SCHOUWEN AND GOEREE MEMBERS. 93

FIGURE 7.6: TRANSIT TIME OF BOTH P- AND S-WAVES. LEFT: PERPENDICULAR TO THE BEDDING. RIGHT: PARALLEL TO THE BEDDING. 94

FIGURE 7.7: THE ELASTIC MODULI OBTAINED FROM THE UCS TEST OVER AN CERTAIN INTERVAL (RED) AND AT HALF FAILURE LOAD (BLUE)..... 95

FIGURE 7.8: CT IMAGE OF THE CKO6-AA-01-02-05s SHOWING A TRIAXIAL INDUCED SHEAR FRACTURE. HORIZONTAL CROSS SECTIONS (RIGHT) SHOW THE FRACTURE GEOMETRY AT THE TOP, CENTER AND BOTTOM OF THE SAMPLE. AN AVERAGE FRACTURE APERTURE OF 0.24 MM IS DETERMINED. 96

FIGURE 7.9: CT IMAGES OF THE FAILED PTS SAMPLE. LEFT: A VERTICAL CROSS SECTION THROUGH THE CENTER OF THE SAMPLE. RIGHT-TOP: EXTRACTED FRACTURE VOLUME INCLUDING RADIAL FRACTURES. RIGHT-BOTTOM: A HORIZONTAL AND VERTICAL CROSS SECTION OF THE SAMPLE. 97

FIGURE 7.10: TOP VIEW OF THE CKO6-AA-01-02-02s AFTER THE PTS TEST SHOWING A SET OF RADIAL FRACTURES WHICH INITIATED DURING THE HYDROSTATIC UNLOADING OF THE SAMPLE. 97

FIGURE 7.11: SHEAR DISPLACEMENT MECHANISM AS A RESULT OF SHEAR STRESS (LEFT). THE SHEAR STRESS AS A FUNCTION OF THE RELATIVE SHEAR DISPLACEMENT (RIGHT) (ZIMMERMAN, 2003). 98

FIGURE 7.12: SCHEMATIC OVERVIEW OF PRESSURE PULSE SETUP 99

List of tables

TABLE 1 : OVERVIEW OF POROSITY, PERMEABILITY AND DEPTH OF THE DINANTIAN AT THE SPECIFIED WELL LOCATIONS.	20
TABLE 2: ROCK SPECIMEN NAME DETERMINATION.	22
TABLE 3: OVERVIEW OF ROCK PARAMETERS AND THE USED METHODS.	24
TABLE 4: RESULTS FROM THE BRAZILIAN TENSILE STRENGTH TEST. *NOT INCLUDED IN THE AVERAGE AND STANDARD DEVIATION.	45
TABLE 5: UNCONFINED COMPRESSIVE STRENGTH RESULTS FROM 4 DIFFERENT SAMPLES.	47
TABLE 6: OVERVIEW OF THE TRIAXIAL TEST DATA INCLUDING THE CONFINING PRESSURE, VERTICAL PRESSURE, YOUNG'S MODULUS AND THE POISSON'S RATIO.	49
TABLE 7: COHESION AND ANGLE OF FRICTION BASED ON THE UCS AND CCS TESTS SPECIFIED ACCORDING TO THE SAMPLE ORIENTATION.	50
TABLE 8: OVERVIEW OF THE YOUNG'S MODULUS AND POISSON'S RATIO OBTAINED FROM THE CONFINED AND UNCONFINED COMPRESSIVE STRENGTH TESTS.	51
TABLE 9: OVERVIEW OF POROSITY VALUES DETERMINED BY THE DIFFERENT METHODS. *ERROR RANGE FROM KUILA (2013).	53
TABLE 10: PERMEABILITIES TESTED WITHIN THE TRIAXIAL SYSTEM AT A CONFINING PRESSURE OF 2 MPA	58
TABLE 11: LITERATURE VALUES OF THE UNCONFINED COMPRESSIVE STRENGTH OF CARBONIFEROUS LIMESTONE	68
TABLE 12: FAILURE ANGLES OF THE TRIAXIAL DEFORMED SAMPLES. *BASED ON THREE MAIN FRACTURES. **ANGLE ONLY DETERMINED OUTSIDE THE FRACTURE COMPLEX.	90

Appendix A

Schedule Kohlenkalk samples				
Name:	Length [mm]	Diameter [mm]	Test #1	Test#2
CKO6-AA-01-03-06p	100,03	49,89	Triaxial	
CKO6-AA-01-03-01p	95,98	49,94	Triaxial	
CKO6-AA-01-03-05p	100,02	49,98	Triaxial	
CKO6-AA-01-02-01s	98,90	49,89	Triaxial	
CKO6-AA-01-02-08s	97,41	49,96	Triaxial	
CKO6-AA-01-02-10s	98,61	49,99	Triaxial	
CKO6-AA-01-02-05s	97,16	49,92	Triaxial	
CKO6-AA-01-03-07p	100,00	50,03	UCS	
CKO6-AA-01-01-06s	100,02	49,95	UCS	
CKO6-AA-01-03-02p	98,62	49,93	UCS	
CKO6-AA-01-01-11s	97,56	49,92	UCS	
CKO6-AA-01-02-07s	24,30	49,93	BT	
CKO6-AA-01-02-03s	26,57	49,83	BT	
CKO6-AA-01-02-12s	26,93	49,97	BT	
CKO6-AA-01-02-11s	28,90	50,00	BT	
CKO6-AA-01-03-09p	27,50	50,07	BT	
CKO6-AA-01-03-11p	27,70	50,03	BT	
CKO6-AA-01-03-08p	27,20	49,93	BT	
CKO6-AA-01-03-12p	27,37	49,90	BT	
CKO6-AA-01-03-10p	28,60	50,03	BT	
CKO6-AA-01-03-16p	50,02	24,82	steady state	Pulse Method
CKO6-AA-01-03-17p	50,14	24,86	steady state	Pulse Method
CKO6-AA-01-01-02s	49,42	49,90	PTS (fail)	
CKO6-AA-01-01-07s	49,31	49,96	PTS (fail)	
CKO6-AA-01-01-09s	49,69	49,90	PTS (fail)	
CKO6-AA-01-02-02s	49,93	49,86	PTS	
CKO6-AA-01-03-18p	40,08	24,80	Helium Pycnometry	
CKO6-AA-01-03-13p	40,02	24,79	Helium Pycnometry	
CKO6-AA-01-03-15p	40,03	24,80	Helium Pycnometry	
CKO6-AA-01-01-10s	97,72	49,88	Ultrasonic	Hydrostatic weighing
CKO6-AA-01-02-04s	98,34	49,93	Ultrasonic	
CKO6-AA-01-02-05s	97,16	49,92	Hydrostatic weighing	
CKO6-MIP1	n.a.	n.a.	MIP	
CKO6-MIP2	n.a.	n.a.	MIP	

Figure 7.1: Overview of the investigated samples including their dimensions and tests.

Appendix B

The samples tested within the triaxial setup show a different deformation behaviour. The x/y-oriented cores show an increasing failure angle at higher confining pressures. Besides the CKO6-AA-01-03-06p shows a three fractures, and therefore it is in the transition between the UCS failure and shear fracturing. The z-oriented samples show a comparable deformation: an increasing failure angle at higher confining pressures. The CKO6-AA-01-02-01s shows at the center a complex fracture structure with conjugate fractures. These conjugates are a mix of both dilational and shear fractures and therefore indicate the transition towards shear fractures at higher confining pressures.

Sample code	Failure angle average [°]	Failure angle range [°]
CKO6-AA-01-03-06p*	19	15 - 21
CKO6-AA-01-03-01p	22	17 - 25
CKO6-AA-01-03-05p	23	22 - 27
CKO6-AA-01-02-01s**	19	13 - 21
CKO6-AA-01-02-08s	21	20 - 22
CKO6-AA-01-02-10s	27	19 - 31
CKO6-AA-01-02-10s	27	24 - 31

Table 12: Failure angles of the triaxial deformed samples. *Based on three main fractures. **Angle only determined outside the fracture complex.

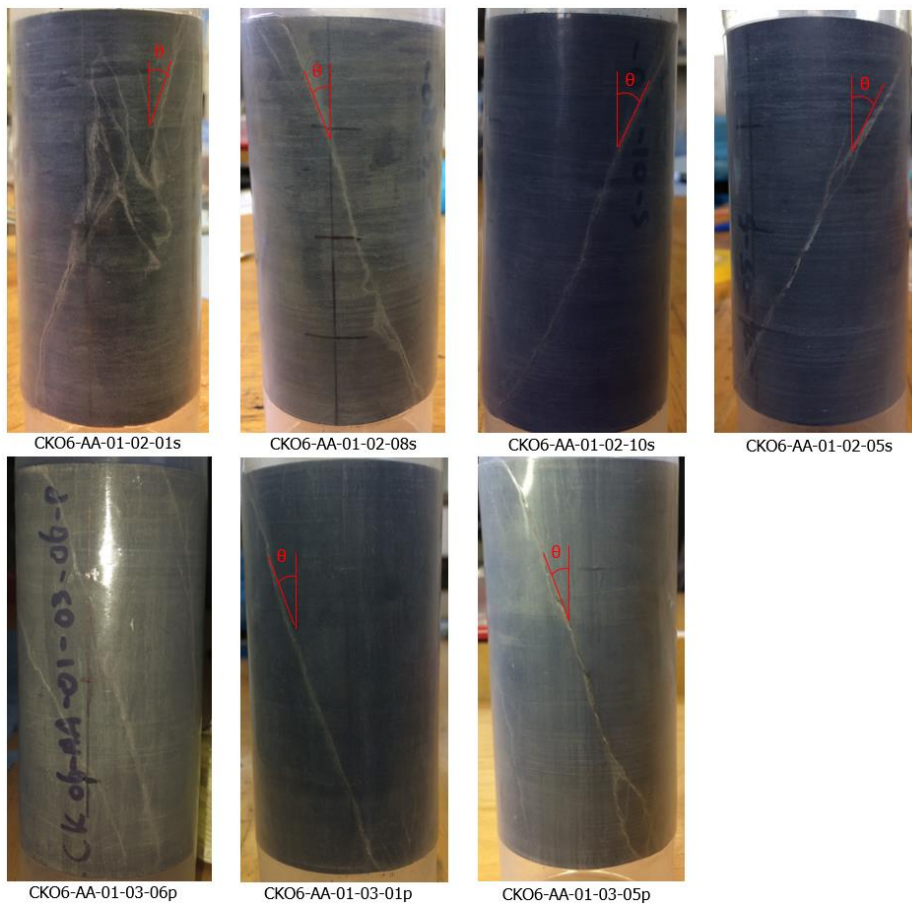


Figure 7.2: Overview of the triaxial induced shear fractures indicating their failure angle.

Appendix C

Within the laboratory of the TU Delft 37 Brazilian disc tests have been performed by R.R. Bakker. The samples were taken from a different block compared to the samples in this study. In this case, sample dimensions of 40 mm in diameter and 20 mm in thickness were used. The results of both the tensile strength and mode I fracture toughness are combined with the results from this study (Figure 7.3). The results of the Brazilian disc tests performed in Delft show a wide range of tensile strengths. In addition, the overall tensile strengths are larger compared with the experiments in this study.

In the case the bedding is parallel to the load direction (red in Figure 7.3), the average tensile strength is 10.6 MPa ranging from 6.8 MPa to 13.2 MPa. About the same range of tensile strengths is observed within the samples with their bedding perpendicular to the load direction (blue and yellow in Figure 7.3). The perpendicular oriented samples have an average tensile strength of 11.2 MPa ranging from 6.2 MPa to 15.6 MPa and the parallel oriented samples with their bedding perpendicular to the load have an average of 11.85 MPa ranging from 11.1 MPa to 12.7 MPa. Therefore, almost no difference can be observed between the tensile strengths and thus no indication for anisotropy.

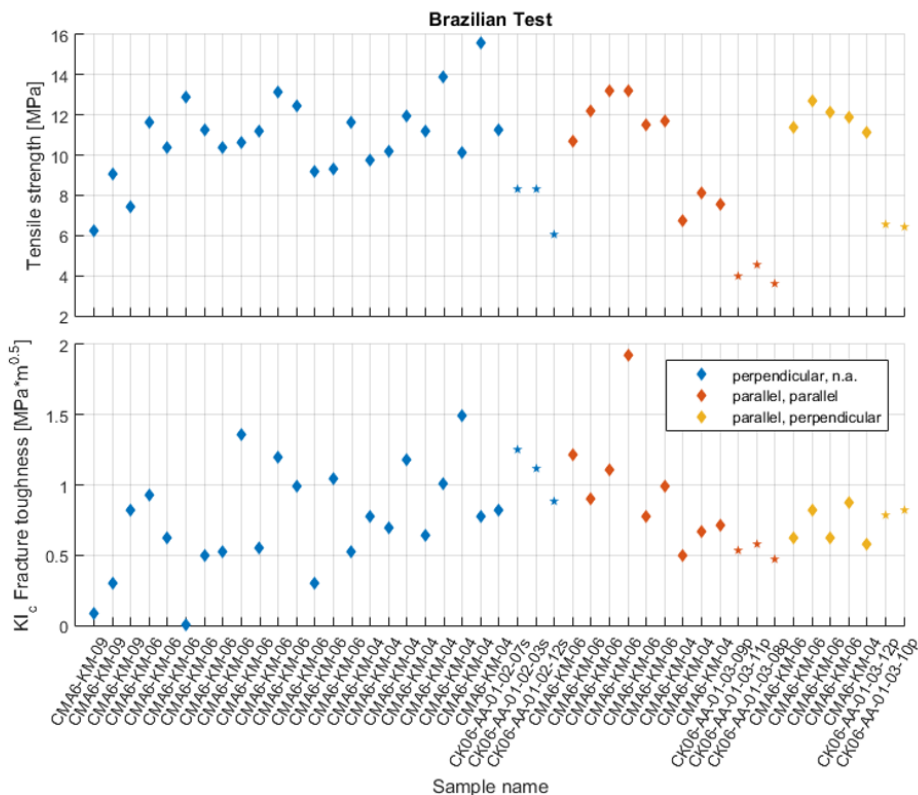


Figure 7.3: Tensile strength and mode I fracture toughness of Brazilian disc test. The CMA6- samples correspond to the experiments performed by R.R. Bakker. The CKO6- samples correspond to the experiments performed in this study.

The fracture toughness of all samples is determined based on the residual stress after tensile failure. The perpendicular oriented samples showed a wide range of fracture toughness values, ranging from 0 to 1.5 MPa·m^{0.5} with an average of 0.8 MPa·m^{0.5}. A few of these samples showed almost no residual strength after the tensile failure, resulting in a fracture toughness close to zero. The parallel oriented samples with the load parallel to the bedding showed slightly higher average value of 1.0 MPa·m^{0.5} and also a wide range from 0.5 to 2.0 MPa·m^{0.5} of fracture toughness values.

The parallel oriented samples with the load perpendicular to the bedding have the lowest fracture toughness with the smallest range: $0.7 \text{ MPa}\cdot\text{m}^{0.5}$ average ranging from $0.6 \text{ MPa}\cdot\text{m}^{0.5}$ to $0.9 \text{ MPa}\cdot\text{m}^{0.5}$.

Based on the tensile strength values and the range no distinction can be made between the different sample orientations. Therefore the tensile strength seems independent of the bedding orientation. Overall, the average values of the fracture toughness of different orientations are comparable to each other. Based on these values the propagation of a tensile fracture is not dependent on its orientation with respect to the bedding. The wide range of fracture toughness values indicates heterogeneity within the different investigated discs.

Appendix D

A failure envelope is set up based on the tensile, unconfined compression strength and confined compression strength. The tensile region is based on the average tensile strength (for the specific orientation) tested by the indirect Brazilian tensile strength tests. The compressive part of the failure envelope is based on the Mohr-Coulomb failure criterion, as described in 3.4.3. The friction angle φ can be described in terms of the rock failure angle θ :

$$\varphi = \frac{\pi}{2} - 2\theta \quad (35)$$

Where θ is measured based on Figure 7.2. and the internal friction coefficient is described as:

$$\mu = \tan(\varphi) \quad (36)$$

The cohesive strength S is a soil mechanics term and describes the adhesion of soil particles. Within rock mechanics this is simply the intercept at zero normal stress. The slope of the failure envelope φ is the dependent on the maximum and minimum principle stress.

Anisotropy

Jaeger (1960) states a rock containing well-defined parallel planes of weakness, has no limiting shear strength when the principle strength is parallel or perpendicular to the plane of weakness (Figure 7.4). This theory was modified by as the extended Jaeger criteria based on experimental data, resulting in a maximum shear strength at either $\beta = 0^\circ$ or $\beta = 90^\circ$.

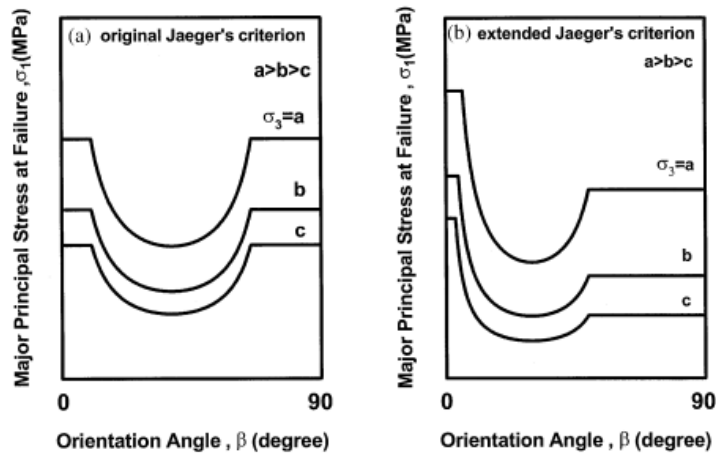


Figure 7.4: Overview of the original Jaeger's anisotropic criteria (left) and the extended Jaeger's criteria (right) (after Tien and Kuo 2001).

In the triaxial experiments, the bedding plane is assumed as the plane of weakness according to the results of the Brazilian tensile strength test. Since this plane is either oriented parallel (x/y-oriented samples, $\beta = 0^\circ$) or perpendicular (z-oriented samples, $\beta = 90^\circ$) to the maximum principle stress, this plane should not affect the peak shear strength. Therefore it can be concluded the strength of the rock itself is dominated by the rock material and is independent on the plane of weakness (Tien and Kuo, 2001). The rock samples with a $\beta = 0^\circ$ or $\beta = 90^\circ$ are therefore treated as two different rocks, resulting in orientation based mechanical rock parameters.

Appendix E

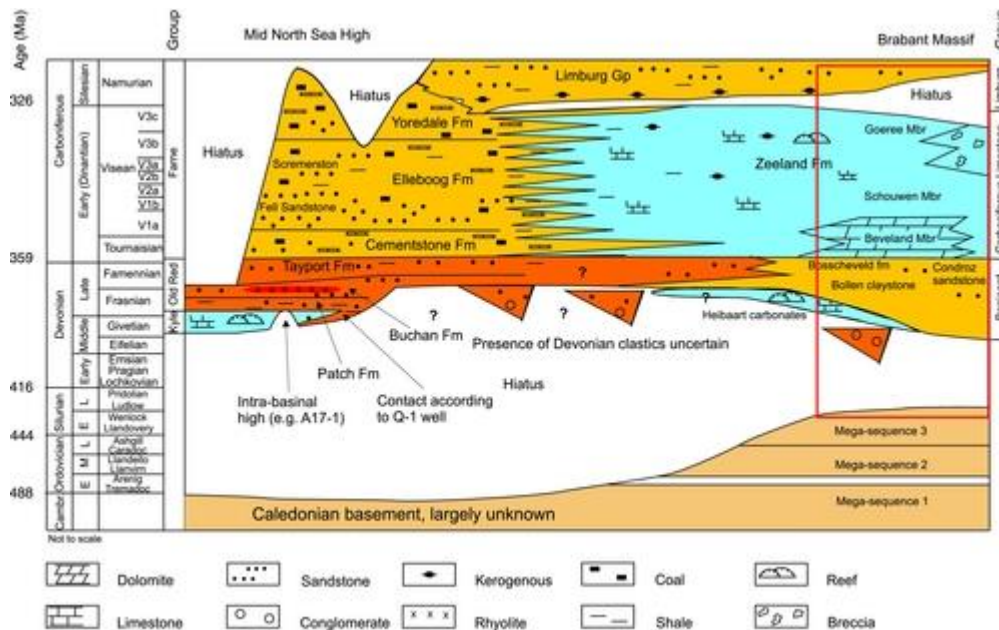


Figure 7.5: Distribution of rocks within the Lower Carboniferous indicating the Beveland, Schouwen and Goeree members.

Appendix F

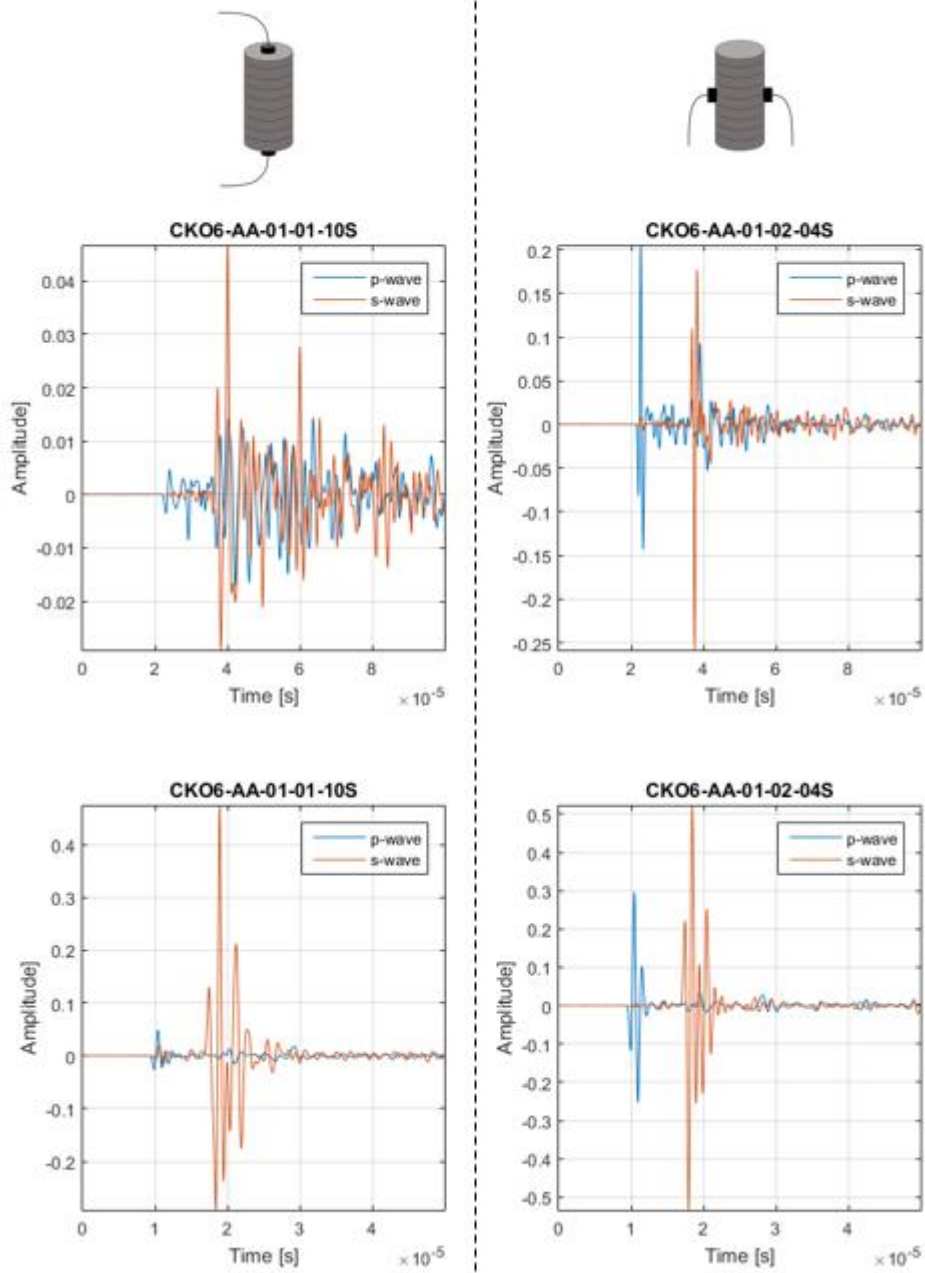


Figure 7.6: Transit time of both p- and s-waves. Left: perpendicular to the bedding. Right: parallel to the bedding.

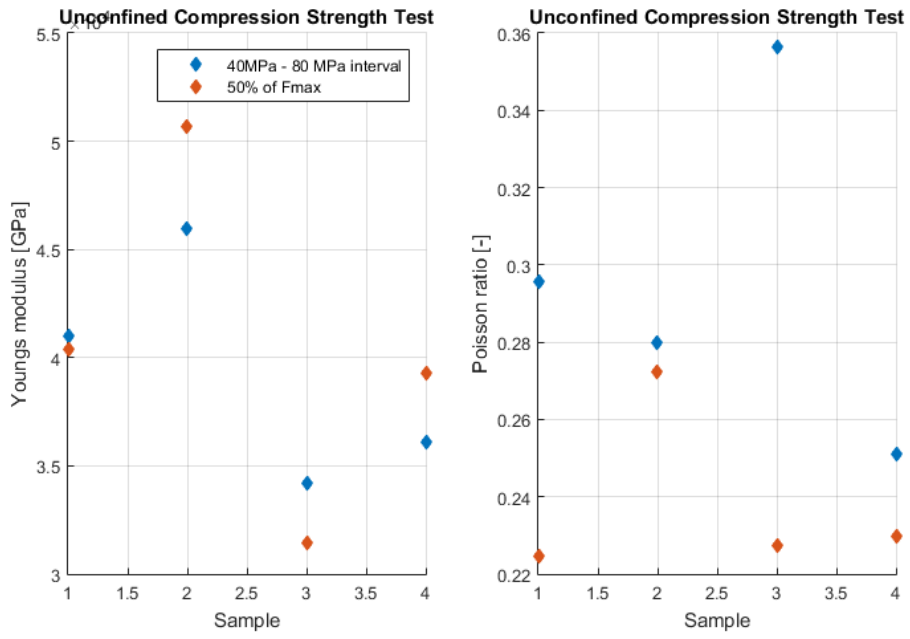


Figure 7.7: The elastic moduli obtained from the UCS test over an certain interval (red) and at half failure load (blue).

Appendix G

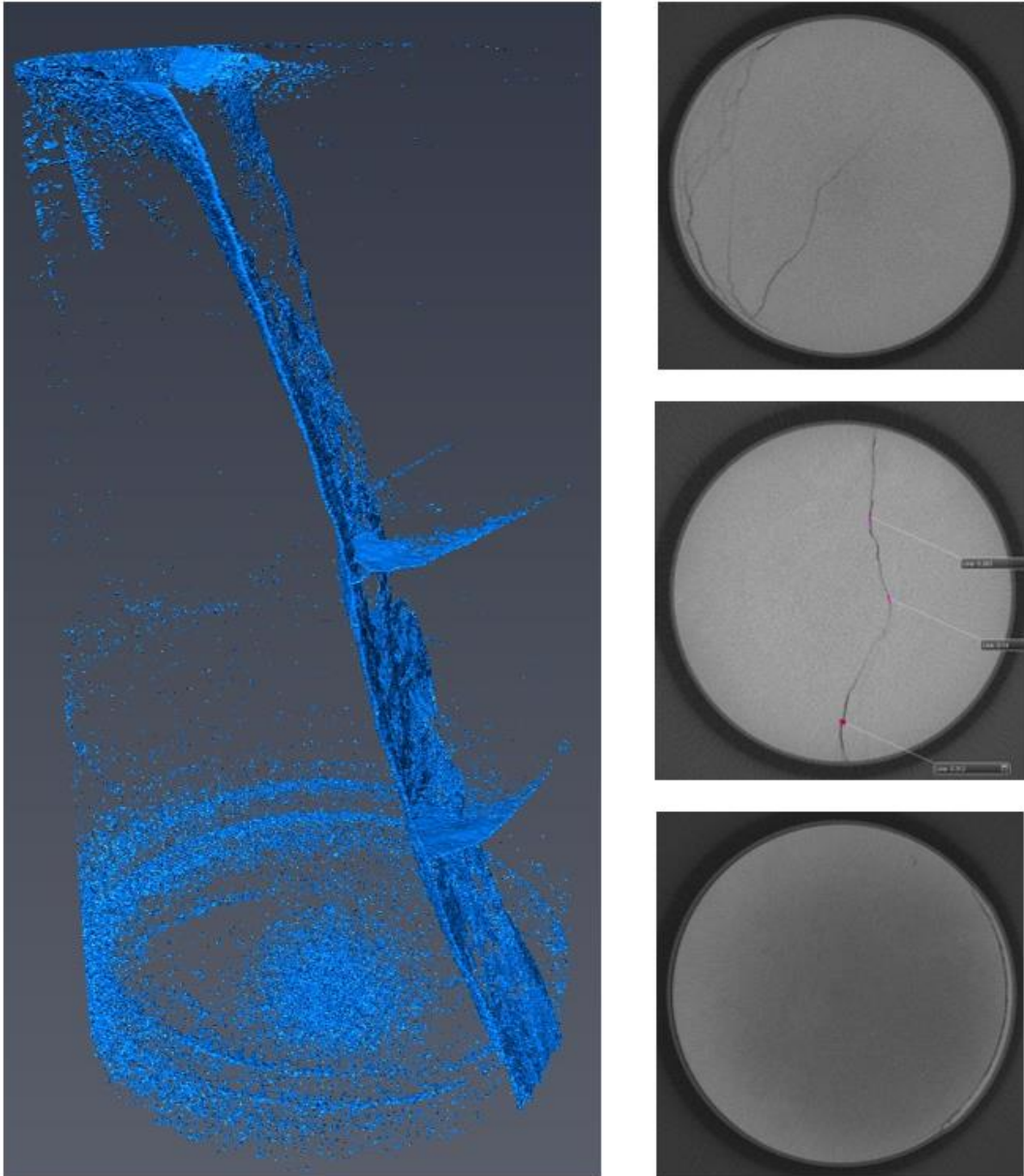


Figure 7.8:CT image of the CKO6-AA-01-02-05s showing a triaxial induced shear fracture. Horizontal cross sections (right) show the fracture geometry at the top, center and bottom of the sample. An average fracture aperture of 0.24 mm is determined.

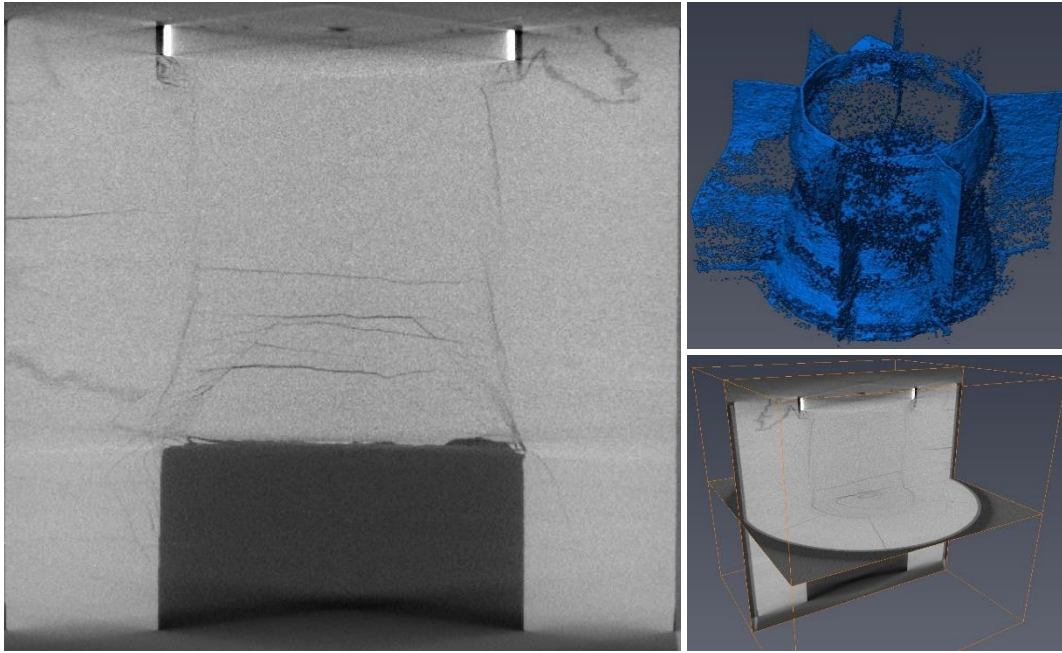


Figure 7.9: CT images of the failed PTS sample. Left: a vertical cross section through the center of the sample. Right-top: extracted fracture volume including radial fractures. Right-bottom: a horizontal and vertical cross section of the sample.



Figure 7.10: Top view of the CKO6-AA-01-02-02s after the PTS test showing a set of radial fractures which initiated during the hydrostatic unloading of the sample.

Appendix H

If a fracture opens and/or shears, it is expected the fracture permeability will increase. The tendency of a surface to slip is described by the slip tendency (Morris et al, 1996) and is described by the ratio of shear stress to normal stress on the fault plane:

$$T_s = \frac{\tau}{\sigma_{eff}} = \mu_s \quad (37)$$

Where T_s is in the range between 0 and 1, τ the shear stress, σ_{eff} the effective normal stress and μ the sliding friction coefficient. If the slip tendency exceeds the value of 0.85, the fault will slip according to Byerlee's law (for $\sigma < 200$ MPa). Whether a plane of weakness is

slipping or not is therefore dependent on the stress field and the fault geometry. Ferril (1999) described the dilation tendency, which is the potential to open a fracture:

$$T_d = \frac{\sigma_1 - \sigma_n}{\sigma_1 - \sigma_3} \quad (38)$$

Again, the stress field and fracture orientation are key parameters whether dilation occurs or not. The higher the ratio, the higher the tendency to dilate which is directly related to the aperture of the fracture and therefore to the permeability of the fracture.

Traction acting on a fracture plane can be divided into a normal and a shear component. The normal component is forcing to a normal closure, the shear component is forcing to offset the fracture planes relatively to each other. Since the fracture planes are both rough-fracture surfaces, the shear component is forced to cause a displacement perpendicular to the fracture plane. This mechanism is referred to as shear deformation (Zimmerman, 2003). During the displacement asperities cause dilation of the fracture (Figure 7.11). At a certain point the maximum shear stress will be reached, initiating irreversible damage to the fracture. Further relative movement of the fracture planes follows under lower shear stress due to crushed and sheared off asperities (Figure 7.11). The maximum shear stress is also known as the shear strength and increases as the normal stress applied on the fracture increases (Goodman, 1976).

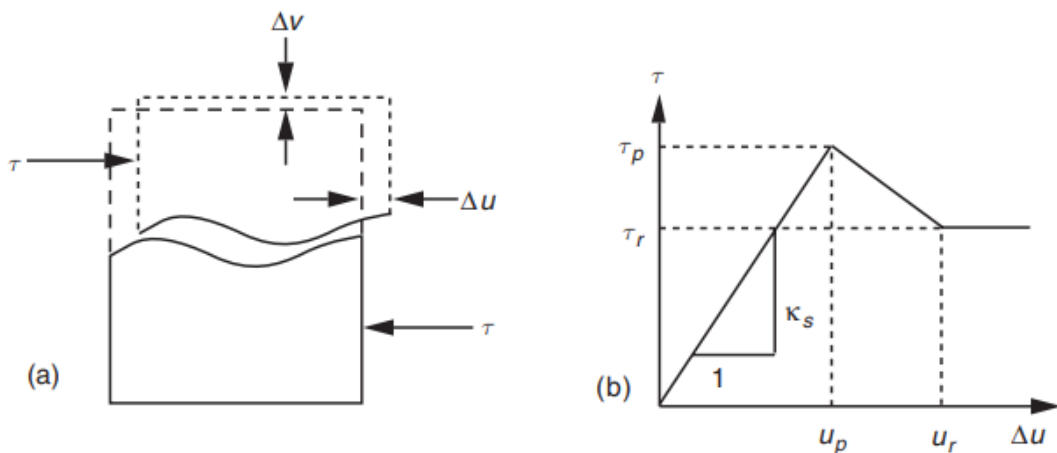


Figure 7.11: shear displacement mechanism as a result of shear stress (Left). The shear stress as a function of the relative shear displacement (Right) (Zimmerman, 2003).

The shear mechanism causes a change of aperture during displacement and therefore influences the fracture permeability. The aperture of where the fluid flows through is described by the cubic law, assuming two parallel plates. However, due to the fracture roughness and asperities the aperture over the fracture is not constant. A numerical study showed the cubic law solution overestimates the fracture permeability (Kluge et al., 2017).

Aperture can be described as mechanical and hydraulic aperture. Mechanical aperture is defined as the average point-to-point distance between rock and surface (Olsson and Barton, 2001) and hydraulic aperture as the result of laminar flow through the fracture based on the cubic law. In this study the latter is defined.

Appendix I

Pressure pulse

The permeability of a rock sample is obtained by the following experimental arrangement (Figure 7.12, Brace 1968): a specimen is subjected to a confining pressure, which is nearly equal to $P_\Sigma - P_1$ and P_2 . At time t_0 the pressure of P_1 is increased. As a result, the fluid

medium starts to flow through the rock sample to establish a new equilibrium. Neglecting the compressibility due to the pressure difference the pressure gradient can be expressed by (Brace, 1968):

$$\frac{dP}{dx} \cong f(t) \quad (39)$$

The permeability of the sample can be found by:

$$(P_1 - P_f) = \Delta P \left[\frac{V_2}{V_1} + V_2 \right] e^{-\alpha t} \quad (40)$$

Where:

$$\alpha = \left(\frac{kA}{\mu BL} \right) \left(\frac{1}{V_1} + \frac{1}{V_2} \right) \quad (41)$$

A is the cross-sectional area [m²], k the permeability of the specimen [m²], μ the viscosity of the pore fluid [Pa*s], V the volume of the reservoir 1 and 2, t the time [s] and P_f the final pressure at equilibrium [Pa] (Figure 7.12). Alpha can be obtained from the slope of the time vs. $(P_1 - P_f)$ curve.

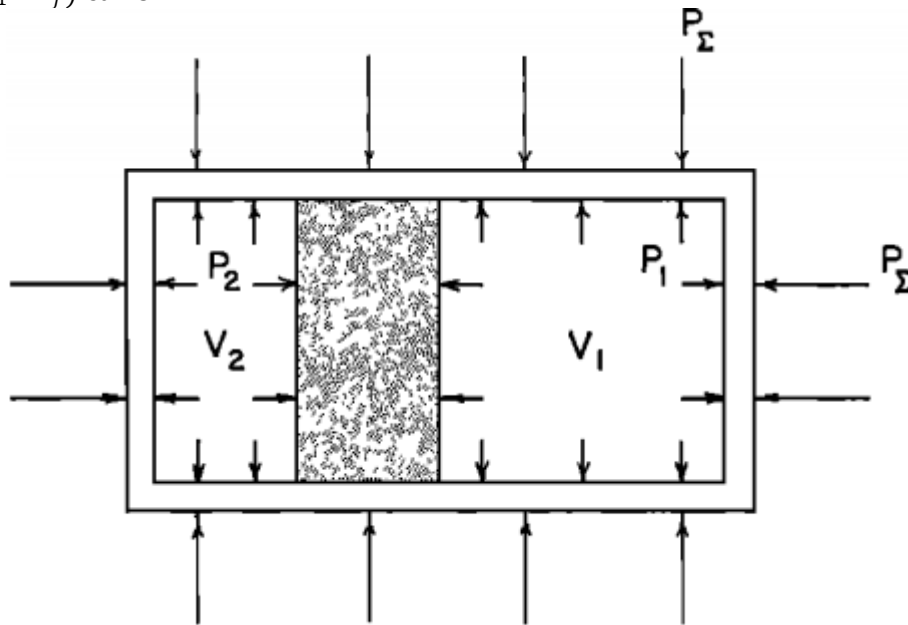


Figure 7.12: Schematic overview of pressure pulse setup

